



TECHNISCHE
UNIVERSITÄT
WIEN

DISSERTATION

**Catalytic CO oxidation on Palladium
and Rhodium model catalysts:
a PEEM and XPS study**

ausgeführt zum Zwecke der Erlangung des akademischen Grades eines
Doktors der Naturwissenschaften unter der Leitung von

Assoc.Prof. Dipl.-Phys. Dr.rer.nat. Yuri Suchorski

Univ.Prof. Mag.rer.nat. Dr.rer.nat. Günther Rupprechter

Institut für Materialchemie (E165)

eingereicht an der Technischen Universität Wien

Fakultät für Technische Chemie

von

M.Sc. Ivan Bernalov

Matrikelnummer 1228698

Dr. Bruno Buchwieser gasse 1/1113

2340 Mödling, Österreich

Wien, den 20.04.2016

Kurzfassung

Die *CO* Oxidation ist eine ökologisch relevante Reaktion. Aufgrund der hohen Toxizität von *CO* ist die Befreiung der Autoabgase von *CO* immer noch ein wichtiger Punkt in der modernen kommerziellen Katalyse. Durch die kommerzielle Nutzung von "Start-Stop" Systemen und modernen Hybridfahrzeugen, bei denen der Drei-Wege-Katalysator oft auskühlt, da die Verbrennungsmotoren häufig abgeschaltet werden, hat die Erforschung der katalytischen *CO* Oxidation nicht im Geringsten an Wichtigkeit verloren - sie ist sogar noch wichtiger geworden.

Herkömmliche Drei-Wege-Katalysatoren, die zur Reinigung der Autoabgase verwendet werden, beinhalten Edelmetall-Nanopartikeln (in der Regel *Pt*, *Pd* und *Rh*), die auf verschiedenen oxidischen Trägermaterialien aufgebracht werden.

Die Oberflächen von katalytisch aktiven Edelmetall-Nanopartikel bestehen aus unterschiedlichen Facetten, deren kristallographische Orientierungen nicht notwendigerweise zu niedrigen Miller-Index Flächen passen, sondern oft vicinale Flächen darstellen. Daher ist die Untersuchung von katalytischen Eigenschaften von gestuften Übergangsmetalloberflächen hoch aktuell.

Im Zuge dieser Dissertation wurden die katalytischen Eigenschaften von μm -großen *Rh*-Oberflächen einer polykristallinen *Rh*-Folie, die vicinal zu den [111]-, [100]- und [110]-Richtungen sind, mithilfe eines Photoemissionselektronenmikroskops (PEEM) untersucht. Zur Untersuchung der katalytischen Eigenschaften einzelner μm -großer Domänen wurde der "*Kinetik durch Abbilden*" Ansatz verwendet. Dieser Ansatz basiert auf der räumlich aufgelösten Analyse von PEEM Intensitäten von Abbildungen der untersuchten Oberfläche während einer laufenden katalytischen Reaktion, wobei während der Messung äußere Parameter verändert werden.

Durch die Analyse der PEEM Video Bilder, die während der *CO* Oxidationsreaktion

aufgezeichnet wurden, konnten lokale kinetische Phasendiagramme für die einzelnen Domänen, welche vicinal zu den [111]-, [100]- und [110]-Richtungen sind, bei einem konstantem Sauerstoffdruck von 1×10^{-6} mbar im Temperaturbereich von 393 bis 458 K konstruiert werden.

Der Vergleich der lokalen Phasendiagramme, die bei identischen Reaktionsbedingungen gemessen wurden, zeigt einen Einfluss der Stufendichte auf die katalytische Aktivität von gestuften *Rh*-Oberflächen: die Zunahme der Stufendichte bei [111]- und [100]-Richtung orientierten Oberflächen führt zu einer Erhöhung der Toleranz dieser Oberflächen gegenüber der *CO* Vergiftung.

Für *Rh*-Oberflächen, die vicinal zu der [110]-Richtung sind, wurde jedoch der entgegengesetzte Effekt beobachtet: eine Zunahme der Dichte der Stufen führte zu einer Verringerung der Toleranz dieser Oberflächen gegenüber der *CO* Vergiftung.

Als Hauptgrund für dieses "entgegengesetzte Verhalten" von zur [110]-Richtung vicinalen *Rh*-Oberflächen wird die Einlagerung von Sauerstoff in die *Rh*-Oberfläche (sub-surface oxygen) vorgeschlagen, da eingelagerter Sauerstoff das katalytische Verhalten der Oberfläche signifikant verändern kann. Die Hypothese der Sauerstoffeinlagerung basiert auf Experimenten mit H_2 Oxidation auf der gleichen polykristallinen *Rh*-Folie: die Bildung von Bereichen niedrigerer Austrittsarbeit, welche durch die Einlagerung von Sauerstoff unter der Oberfläche erklärt werden kann, wurde im *PEEM* im gleichen Bereich der polykristallinen *Rh*-Folie beobachtet, der auch bei der *CO* Oxidation untersucht wurde. Die intensivsten und langlebigsten "hellen Streifen" bilden sich auf den Regionen, die denen der *Rh* [110]- Vicinalen entsprechen.

Um die Rolle des oxidischen Trägermaterials in der *CO* Oxidation zu studieren, wurden μm -große *Pd*-Pulveragglomerate auf ZrO_x bzw. *Pt* aufgebracht und mithilfe des gleichen experimentellen Ansatz in der *CO* Oxidation untersucht.

Die lokale *PEEM*-Bild Intensitätsänderung wurde während der laufenden *CO* Oxidationsreaktion auf geträgerten *Pd* unter zyklischer Variation des *CO*-Partialdrucks bei konstantem Sauerstoffdruck von 1.3×10^{-5} mbar im Temperaturbereich von 413 bis 523 K aufgezeichnet. Basierend auf diesen Messungen wurden die lokalen kinetischen Phasendiagramme für die *Pd*-Modellsysteme, welche ZrO_x oder *Pt* als Trägermaterial verwenden, konstruiert. Um den Effekt von oxidischen Trägermaterialien auf die

katalytische Aktivität von *Pd*-Agglomeraten zu studieren, wurden die katalytischen Eigenschaften des *Pd/ZrO_x*-Systems mit einem ähnlichen Modellsystem, welches eine polykristalline *Pt*-Folie als Trägermaterial verwendet, verglichen. Dieser Vergleich zeigt eine signifikante Veränderung der katalytischen Aktivität der *Pd*-Agglomerate durch die Änderung der Art des Trägermaterials: das *Pd* mit oxidischem Trägermaterial zeigt eine signifikant höhere Toleranz gegenüber der *CO* Vergiftung, als das System mit *Pt* als Trägermaterial.

Um die Rolle des oxidischen Trägermaterial in der *CO* Oxidation besser zu verstehen, wurde der Einfluss der Dicke des *ZrO_x* auf die katalytische Aktivität des *Pd* untersucht. Diese Studie ergab einen beobachtbaren Einfluss der Oxidschichtdicke auf die katalytischen Eigenschaften der Modellsysteme: eine Erhöhung der Oxidschichtdicke führt zu einer Erhöhung der Toleranz gegenüber der *CO* Vergiftung.

In diesem Zusammenhang wurde die Zusammensetzung des Trägermaterials *ZrO_x* durch Untersuchung der Oxidation von polykristallinen *Zr*-Oberflächen mit *XPS* und *PEEM* studiert. Die Analyse der *XPS* Daten zeigte die Bildung von substöchiometrischen Oxiden bei niedriger Sauerstoffexposition. Es wurde gezeigt, dass während der ersten (schnellen) Stufe der Oxidation, eine substöchiometrische *Zr*-Oxidschicht entsteht. Diese Schicht enthält drei verschiedenen Spezies (Zr^{+1} , Zr^{+2} und Zr^{+3}) zwischen der metallischen *Zr*-Oberfläche und der oberen stöchiometrischer *ZrO₂*-Schicht. Bei sehr niedriger Sauerstoffexposition (≤ 4 L) bildet sich nur die substöchiometrische Schicht. Die Bildung der stöchiometrischen *ZrO₂*-Auflageschicht tritt in der zweiten (langsamen) Stufe der Oxidation ein. Auch *in situ* Beobachtungen der Oxidation von polykristallinem *Zr* unter den gleichen Bedingungen mittels *PEEM* stimmen mit dem Modell der zweistufigen Oxidation von *Zr* überein.

Abstract

The *CO* oxidation reaction is still an environmentally important reaction. Indeed, due to the toxic character of *CO*, the decrease of its content in the car exhaust is still one of the focus points of modern commercial catalysis. Moreover, due to the spreading of "start – stop" systems and of modern hybrid vehicles, where the internal combustion engines are often switched off, leading to the cooling down of the three-way catalysts (*TWC*), the importance of the effective oxidation of *CO* is even increased nowadays. Conventional *TWCs*, which are used for purifying the car exhaust from *CO*, are composed of noble metal nanoparticles (usually, *Pt*, *Pd* or *Rh*) supported by different oxidic supports. The catalytically active noble metal nanoparticles expose different facets, whose crystallographic orientations do not necessary fit to low Miller index planes. Therefore, studies of stepped transition metal surfaces are highly up to date. In the present thesis, catalytic properties of stepped (111)-, (100)- and (110)- type vicinal *Rh* surfaces, formed on μm -sized domains on a polycrystalline *Rh* foil, were studied by *PEEM*. For the investigation of the catalytic properties of individual μm -sized domains of a polycrystalline foil in the *CO* oxidation, the *kinetics by imaging approach* was used. This approach is based on monitoring the local *PEEM* intensity of the surface during an ongoing catalytic reaction while varying external parameters. By analysis of *PEEM* video frames recorded during the *CO* oxidation reaction, local kinetic phase diagrams for stepped (111)-, (100)- and (110)- type vicinal *Rh* surfaces were constructed for constant oxygen pressure of 1×10^{-6} mbar and for a constant temperature in the range of 393 to 458 K. Comparison of the local kinetics phase diagrams constructed for (111)-, (100)- and (110)- type vicinal *Rh* surfaces at identical reaction conditions revealed an influence of the density of steps on catalytic performance of stepped *Rh* surfaces: an increase of density of steps on (111)- and (100) type

vicinal *Rh* surfaces leads to an increase of the tolerance of these surfaces towards *CO* poisoning.

However, for the case of (110)-type vicinal *Rh* surfaces, the opposite effect was observed, namely an increase of the density of steps leads to a decrease of the tolerance of these surfaces towards *CO* poisoning. It was proposed, that the reason of this "opposite behaviour" of (110)-type vicinal *Rh* surfaces originates from the formation of subsurface oxygen, which can alter the catalytic behaviour. The suggestion about the formation of subsurface oxygen, was supported by experiments with H_2 oxidation on the same polycrystalline *Rh* foil. The formation of regions of reduced work function ("white stripes"), which indicate formation of subsurface oxygen, was observed by *PEEM* for the same regions of the polycrystalline *Rh* foil which was used for *CO* oxidation. The most intensive and long-living "white stripes" were observed on (110)-type vicinal *Rh* surfaces.

Beside the stepped *Rh* surfaces, μm -sized *Pd* powder agglomerates supported by ZrO_x and by *Pt* were studied using the same experimental approach. Motivation to study the supported *Pd* model systems was dictated by the opportunity to demonstrate the effect of an oxidic support on the catalytic properties of such model systems.

The local *PEEM* intensity was monitored during ongoing *CO* oxidation reaction under cyclic variation of *CO* partial pressure and at constant oxygen pressure of 1.3×10^{-5} mbar in the temperature range of 413 to 523 K. Based on these measurements, local kinetic phase diagrams for the *Pd* powder agglomerates supported by ZrO_x and *Pt* were constructed. In order to study the effect of the oxidic support on the catalytic performance of the *Pd*, the activity of the oxide-supported (in present case, ZrO_x -supported) *Pd* was compared with that of *Pd* supported by polycrystalline *Pt*. This comparison revealed a remarkable change of catalytic properties of supported *Pd* by changing the type of supporting material: the oxide-supported *Pd* exhibits significantly higher tolerance towards *CO* poisoning, than the *Pd* supported by *Pt*.

To reveal the details of the role of an oxidic support on the catalytic performance of supported *Pd*, the influence of thickness of the oxidic support on the catalytic performance of the model system was studied. This study revealed an observable effect of the oxide layer thickness on the catalytic properties of supported *Pd*: an increase

of the supporting oxide layer thickness leads to an increase of the tolerance of the supported *Pd* model system towards *CO* poisoning.

In this context, the composition of the supporting ZrO_x layer was studied in detail by the investigation of initial oxidation of polycrystalline *Zr* surfaces using *XPS* and *PEEM*. Analysis of *XPS* data revealed the formation of substoichiometric oxidic species at low oxygen exposure. It was shown, that during the first (fast) oxidation stage, the formation of the *Zr* suboxide interlayer consisting of three suboxidic components (Zr^{+1} , Zr^{+2} and Zr^{+3}), which are located between the metallic *Zr* surface and a stoichiometric ZrO_2 overlayer, takes place, whereas at very low oxygen exposure (about 4 L) a sole suboxide layer forms. Formation of the stoichiometric ZrO_2 overlayer occurs during the second (slow) oxidation stage. *In situ* observations of the initial oxidation of polycrystalline *Zr* at the same condition as in *XPS*, but in *PEEM* are in agreement with the two stage oxidation model.

Acknowledgements

I would like to express my sincere gratitude to the people who supported me during my doctoral study. I would like to thank...

*....my supervisors **Prof. Yuri Suchorski** and **Prof. Günter Rupprechter** for the opportunity to perform the research within the topic of the present thesis, for their precious guidance and support at all stages of my Ph.D. study.*

*....**Dr. Michael Stöger-Pollach** for his willingness to review this thesis.*

*....**Dr. Diana Vogel** for familiarizing me with the experimental setup.*

*....my "group mates" **Mag.rer.nat. Martin Datler**, **Dipl.-Chem.(FH) Sebastian Buhr**, **B.Sc. Johannes Zeininger** and **Clara Freytag** for the great collaboration, countless scientific discussions and for making a scientific atmosphere inside the group.*

*....**Prof. Johannes Bernardi** for the EBSD measurements.*

*....**Fonds zur Förderung der wissenschaftlichen Forschung (FWF)** in particular the Special Research Program Functional Oxide Surfaces and Interfaces (SFB F45 FOXSI) for financial support of this research.*

*....**Johannes Frank** for technical support.*

*....all **colleagues** at the Institute of Materials Chemistry (IMC) for making the great*

atmosphere in the Institute and, in particular, in the lab.

*....my **family and friends** for their support.*

Contents

1	Introduction	1
1.1	Catalysis: Industrial importance and the role in reshaping of the world	1
1.2	<i>In situ</i> imaging of surface processes	4
1.3	Objectives and challenges of the work	5
1.4	Outline and guideline of the thesis	10
2	Literature overview	12
2.1	Reactions of interest	12
2.1.1	CO oxidation on Pt group metals	12
2.1.2	Initial oxidation on Zr surfaces	14
2.2	Structure of Rh surfaces	16
2.2.1	Low Miller index Rh surfaces	16
2.2.2	Rh surface reconstructions	17
2.2.3	Stepped Rh surfaces	17
2.3	CO and oxygen interaction with Rh and Pd surfaces	19
2.3.1	CO adsorption on Rh and Pd surfaces	19
2.3.2	Oxygen adsorption on Rh and Pd surfaces	20
2.3.3	Diffusion	21
2.3.4	Oxide formation on Rh and Pd surfaces	24
2.4	Langmuir-Hinshelwood reaction mechanism	25
2.5	Bistability and kinetic phase diagram	27
2.6	Interaction of oxygen with Zr surfaces	30
2.6.1	Adsorption	30
2.6.2	Formation of zirconium oxide	30

2.7	Probing of ZrO _x surfaces by XPS	31
2.7.1	Interpretation of Zr chemical shifts in XPS	31
2.7.2	Formation of substoichiometric oxidic species on the Zr surface	33
3	Experimental	36
3.1	The ultrahigh vacuum system	36
3.2	The samples, sample holder and manipulator	38
3.2.1	The samples and sample holder	38
3.2.2	Sample manipulator in the PEEM chamber	39
3.2.3	Sample manipulator in the XPS chamber	40
3.3	The transfer system and the load lock	40
3.4	Preparation of sample surfaces	41
4	Methods	45
4.1	Photoemission electron microscopy	45
4.1.1	Principle of PEEM operation	45
4.1.2	Origin of the PEEM image contrast	48
4.1.3	Design of the PEEM apparatus	49
4.2	X-ray photoelectron spectroscopy	50
4.2.1	Instrumentation	51
4.2.2	Interpretation of XPS spectra	52
4.2.3	Estimation of the thickness of surface layers	55
4.3	Quadrupole mass spectrometry (QMS)	59
4.3.1	Principle of QMS operation	59
4.3.2	Instrumentation	59
4.4	Electron backscatter diffraction	62
5	Reaction kinetics by imaging	64
5.1	Basic idea	64
5.2	Experimental realization	65
6	Experimental study of CO oxidation on stepped Rh surfaces	67

6.1	Preparation and characterisation of the μm -sized stepped Rh domains	67
6.1.1	Formation and identification of high Miller index domains on Rh foil surface	67
6.1.2	XPS characterization of Rh sample surface	70
6.2	Global reaction kinetics of CO oxidation on polycrystalline Rh foil	71
6.3	Local reaction kinetics of CO oxidation on stepped Rh surfaces	72
6.3.1	CO oxidation on (111)-type vicinal Rh surfaces	72
6.3.2	CO oxidation on (100)-type vicinal Rh surfaces	75
6.3.3	CO oxidation on (110)-type vicinal Rh surfaces	77
6.3.4	Step density and other structure effects in the CO oxidation on vicinal Rh surfaces	79
6.4	Summary	87
7	XPS and PEEM study of initial oxidation of polycrystalline Zr foil	88
7.1	Sample preparation	88
7.1.1	The cleaning procedure	88
7.1.2	XPS characterization of the Zr sample surface	89
7.1.3	Formation of individual domains on Zr foil surface	90
7.1.4	Phase transition hcp-bcc in Zr	91
7.2	Initial oxidation of polycrystalline Zr foil	93
7.2.1	Detection of substoichiometric Zr oxide species	93
7.2.2	Effect of the temperature on initial oxidation of Zr	96
7.3	<i>In situ</i> observation of initial Zr oxidation by PEEM	98
7.4	Summary	100
8	PEEM and XPS study of CO oxidation on supported Pd model catalysts	101
8.1	Sample preparation	101
8.1.1	The cleaning procedure and XPS characterization of the sample	101

8.1.2	Identification of Pd and ZrO _x in PEEM	103
8.2	Local reaction kinetics of CO oxidation on ZrO _x	105
8.3	Role of the support in the CO oxidation on Pd	107
8.3.1	Pd/ZrO _x <i>versus</i> Pd/Pt	107
8.4	Role of the Zr oxide layer thickness in the CO oxidation on ZrO _x model catalyst	111
8.4.1	Local reaction kinetics: "thin" <i>versus</i> "thick" oxidic support . .	111
8.5	Summary	115
9	Conclusions	116
	References	124
	Publications list	136
	Conference contributions	136
	Curriculum vitae	143

1 | *Introduction*

Catalysis: Industrial importance and the role in reshaping of the world

The term *catalysis* was defined by Jakob Berzellius in 1835. But, as a phenomenon it was employed by humankind since ancient times changing the lifestyle of the people until present times. The early origins of applications of catalytic processes can be found even in antiquity: e.g. one of the first catalytic processes which was employed by humans was the production of alcoholic beverages from sugar by fermentation, whereas the evidences of fermented beverage production came from ancient China [1]. The first documented employment of catalysts was performed by Valerius Cordus who used sulphuric acid to catalyse the conversion of alcohol to ether [2]. Since then, a lot of bright minds around the globe contributed to the applications of catalysis which have helped to form world around us. This development still proceeds.

The first discovery, that may be considered as a clear evidence that reaction between two gaseous reactants takes place on a solid surface without to change, was made by Humphry Davy [3]. Davy found out that oxygen and coal gas (methane) reacts more easily in the presence of *Pd* or *Pt* wire than without it. This invention was used in so-called *Davy lamp* which helped in detection of methane in coal mines and saved many lives in those times [4].

Significance of the catalysis for modern society can not be totally understood without mentioning the Haber-Bosch process. At the turn of the 19th and 20th century due to growth of world's population demand of the ammonia for fertilizer production rapidly increased. However, in those times all ammonia was obtained only from mining of the

nitre deposits. Already in those times it was clear, that remaining resources of nitre will be not able to satisfy the growing demand [5]. Another possibility to produce ammonia in significant amounts is the fixation of atmospheric nitrogen. Although, due to exceptional stability of the nitrogen molecule which is explained by formation of triple bonds between nitrogen atoms, the N_2 molecules are almost unreactive [6]. The ground-breaking method of ammonia production in significant amounts was invented by Fritz Haber [7]. Haber found a way to force atmospheric nitrogen to react with hydrogen with subsequent formation of ammonia as a desired reaction product. The main idea of this method is performing of the reaction between atmospheric nitrogen and hydrogen on the osmium catalyst surface in a flow reactor at high pressure and temperature conditions [8, 9]. Haber's idea was further improved and scaled up to an industrial level of production by Carl Bosch. For the invention and improvement of the ammonia synthesis process Fritz Haber and Carl Bosch were awarded the Nobel Prize in 1918 and 1931 respectively [6]. The Haber-Bosch process is counted as one of the most important inventions of 20th century. It stays in one line with such great achievements as nuclear energy, space flights and computers. Without the development of the Haber-Bosch process production of ammonia in significant amounts would be hardly possible and the world's population could not have grown from 1.6 billion in 1900 to today's 7 billion [10, 11].

Nowadays, the field of catalysis still attracts remarkable amount of interest due to its industrial and scientific perspectives. Most of the chemical industry processes involve catalysts, leading thus to a serious contribution in the world's economy. Several sectors of the world's economy, such as the petroleum industry, chemical and food industry are fully dependent on catalysis. Catalysis as an economic branch contributes more than 35% to the global GDP [12]. In forecast, the catalysis market will reach a sales volume of 27.59 Billion USD by 2020 [13].

An important example of a modern technological process involving catalysts is the Fluid Catalytic Cracking (FCC). FCC pushes the borders of the petrochemical industry by allowing a more efficient transformation of higher boiling oils into lighter ones. This makes production of gasoline, different gases (propane, butane etc.) and synthetic materials (plastics, synthetic rubbers) more efficient [14, 15].

Catalytic processes are also essential in the clean environmental technology, e.g. in green energy conversion systems, such as fuel cells. Also effective conversion of hazardous pollutants and harmful gases (e.g. car exhausts) could be hardly performed without catalysts. Catalytic removing of harmful gases from car exhaust is successfully performed nowadays by catalytic converters. The first catalytic converters were invented by Eugene Houdry in the mid-1950s [16]. Further improvements have led to the *Three Way Catalytic Converter* which is able to effectively reduce emission of unburned hydrocarbons, carbon monoxide and nitrogen oxides (Fig. 1.1) [17].



Figure 1.1: Schematic illustration of Three Way Catalytic Converter. Adapted from ref. [18].

The prominent role of the catalysis industry and its huge impact to the world's economy leads to intensive research in the field of catalysis. Since real catalysts, *de facto*, are very complex multicomponent systems consisting of highly dispersed metal powders supported by oxidic supports, it is hardly possible to predict their behaviour under working conditions. The popular *trial-and-error* approach is suitable for the creation of commercial catalysts, but the exact tailoring of catalysts for particular reactions or particular conditions is not possible with this approach.

Understanding the complex behaviour of real catalysts needs, obviously, the creation of model systems and a molecular level understanding of how the model catalyst works under idealized conditions and establishing then connections between the behaviour of the model catalysts and the real catalytic systems [19]. This demands, among of others, bridging of *the pressure* and *materials gap* or, in other words, performing of the catalytic research under ambient pressure conditions with catalytic systems of increasing complexity approaching the real catalytic systems (e.g. metal powders supported by oxidic support) [20].

***In situ* imaging of surface processes**

Humans have always wanted to see objects which are far smaller than the limit of their natural eyes perception [21]. By invention of light microscopes this problem was partly solved. However, for surface science and catalysis it is not enough just to observe the small objects like supported nanoparticles, surface domains, defects, etc. It would be highly desirable to track the temporal evolution of physical and chemical properties in real time as well as to simultaneously characterize changes of the physical and chemical properties during a chemical reaction (i.e. *in situ*).

One of the methods which can be successfully employed for real time observation of ongoing physical and chemical processes on the surface is the Photoemission Electron Microscopy (*PEEM*) [22, 23]. The working principle of the *PEEM* is based on collecting of information about the processes which take place on the sample surface by means of photoelectrons emitted from the sample surface upon illumination of the sample with UV-light [22]. The contrast mechanism in *PEEM* is based on the change of the sample local work function and, therefore, the local *PEEM* image intensity is sensitive to the type of adsorbed molecules which cover the surface [22, 24]. This contrast mechanism provides basis for monitoring the ongoing surface processes such as kinetic phase transitions [25], oscillations [24] and pattern formation [26] in real time.

Since, the first application of *PEEM* in catalytic studies this method attracted remarkable attention around the world. The main advantage of this method is the *parallel imaging principle* which gives to this method the ability to observe changes on the whole field of view [27]. This is a significant advantage in comparison with methods such as *STM*, *AFM* or another scanning techniques, which allow the obtaining of information in a certain moment of time from a small confined region only.[28].

First attempts to apply *PEEM* in the catalysis research were performed on nearly ideal, single crystal surfaces of catalytically relevant metals such as *Pd* [23, 29] and *Pt* [10, 24, 30]. This approach shed the light on fundamental properties of some surface reactions, such as *CO* oxidation: e.g. bistability [29, 30], reaction-diffusion fronts

[29, 30], kinetic oscillations [10, 24] and pattern formation [23]. In this early experiments, the effects originating from existence of defects, different components such as metal and oxide were not considered. However, the behaviour of real catalysts differs from that of single crystals (*materials gap*). Bridging this *gap* is possible by increasing the complexity of investigated systems, e.g. from single crystals to polycrystalline foils and, further, to the oxide supported μm -sized metal agglomerates and supported nanoparticles of different size, shape and interparticle distance. Polycrystalline metal foils and supported μm -sized metal powder agglomerates are the center topic of this thesis.

Objectives and challenges of the work

Despite the remarkable progress in the field of *in situ* surface imaging there are still plenty of challenges which have to be faced. As already mentioned, one of this challenging tasks which is relevant for modern catalysis, is bridging the *pressure* and *materials gaps* [20]. Finding solution for this task, at least for particular reaction and catalytic system, needs answering following questions:

- **Pressure gap** - *How do the variation partial pressures of reactants affect the catalyst performance?*
- **Materials gap** - *How does increasing the complexity of the catalyst structure from the simple model systems to technological catalysts change catalyst reaction behaviour?*

In this thesis, the emphasis is placed on the looking for answers to the second question, namely to bridging the *materials gap*, at least for *CO* oxidation on transition metal surfaces. The main strategy of the thesis is to increase complexity along the *the complexity axis* (Fig. 1.2) or, in other words, to increase the complexity of investigated model systems step by step from polycrystalline metal foils to the supported μm -sized metal agglomerates.

CO oxidation on polycrystalline Rh foil

Modern emission abatement devices effectively remove *CO*, *HC* and *NO_x* from gasoline-engine exhaust, helping automakers to fulfil the newest strict emissions regulations [17, 31, 32].

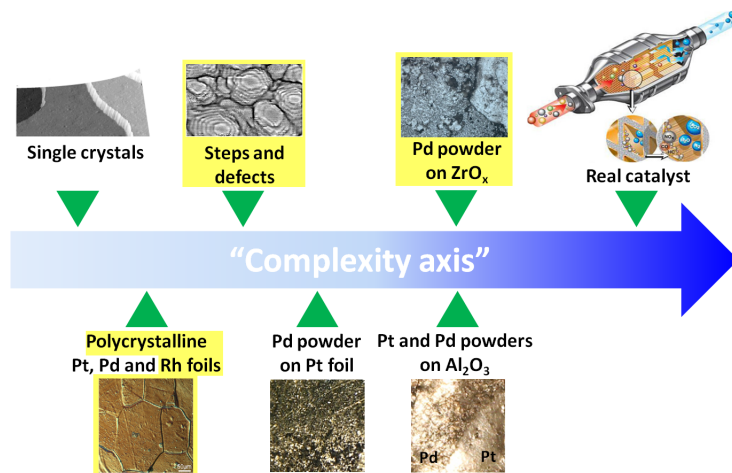


Figure 1.2: Schematic presentation of the complexity axis in present studies of the CO oxidation reaction. The topics of present thesis are marked yellow.

Whereas the CO and HC are quite effectively oxidized by conventional three-way converters ($TWCs$), the NO_x reduction and PM (particulate matter, which becomes to be an increasing problem in the direct injection gasoline engines [33]) abatement remain challenging for the existing technology. The innovative techniques, such as e.g. four-way (FWC by $BASF$) conversion catalyst allows combustion of PM into CO_2 by capturing the particles in the porous monolith walls which act as a kind of a trap for the particulates [35]. This makes the additional particle filter used conventionally in combination with a TWC unnecessary [32, 36]. In the novel converters, the size- and composition-optimized combination of supported Pd and Rh particles perform, as in usual $TWCs$, the catalytic conversion, whereas Pd particles are much more effective in the oxidation and Rh , in turn, is particularly effective in eliminating NO_x due to its efficiency in dissociating NO . The resulting nitrogen usually recombines to N_2 and the remaining oxygen atoms often block the adsorption sites and therefore need to be reactively removed by CO in order to proceed in the reduction reaction [37]. Thus a detailed understanding of the peculiarities of the CO oxidation reaction on Rh is important for the design of novel effective catalysts. Although the CO oxidation on Rh is generally well studied, particular details such as peculiarities of the surface structure sensitivity or exact role of the surface oxides are not entirely clarified [38]. The question of the surface sensitivity was qualitatively cleared in thorough studies on Rh single crystals [39] and in the following vivid discussion [40], but the detailed comparison of the behaviour of differently oriented Rh surfaces in a wide parameter

range is still missing. Since supported *Rh* nanoparticles of technological catalysts typically exhibit different facets to the reactive gases, the existing studies were most frequently carried out for *Rh* single crystal surfaces [41, 42, 43]. Catalytic reaction properties were usually determined by mass spectroscopic product analysis, or, in case of atmospheric pressure conditions, by gas chromatography. To compare the catalytic properties of the different crystallographic orientations, the individual single crystal samples have to be investigated sequentially within a relatively large parameter space of reactant gas pressure and reaction temperature. However, this approach has some limitations and can be used only as a first approximation for prediction of reaction behaviour of real catalyst. These limitations originate from the fact that it is difficult to keep exactly the same experimental conditions for different samples. The parallel measurements using the mass spectroscopic methods are hardly possible due to the basically averaging principle of mass spectroscopic analysis. It has several limitations. Since kinetic transitions from active state to inactive and *vice versa* on the surface are strongly affected by these parameters, comparison of data obtained in separated experiments seems to be hardly possible [44]. Due to this fact, the main challenge in understanding the *CO* oxidation reaction on transition metal surfaces reaction is the comparison of different crystallographic orientation at absolutely the same conditions. This problem was solved, at least for *CO* oxidation reaction on *Pd* and *Pt* polycrystalline surfaces, using the *kinetics by imaging approach* [45, 46]. This approach allows obtaining information about local (domain-specific) and global (spatially averaged) reaction kinetics by evaluation of *PEEM* video sequences coupled with monitoring of the reactants partial pressure using *QMS* [47].

Since polycrystalline surfaces exhibit different orientations, these model systems seem to be suitable candidates for investigation of *structure-reactivity* correlations for *CO* oxidation and other model catalytic reactions [48].

The main objective of this section is extension of *kinetics by imaging* approach to the case of *CO* oxidation reaction on stepped polycrystalline *Rh* surfaces. In here, catalytic *CO* oxidation on polycrystalline *Rh* foil consisting of μm -sized stepped *Rh* domains is investigated under idealized high vacuum conditions at 10^{-6} mbar pressure range. Emphasis is placed on direct comparison of local reaction kinetics taking place

on differently oriented stepped Rh (hkl) domains. Catalytic properties of differently oriented stepped Rh (hkl) domains are compared to each other in respect with high and low reactivity range in $(p_{CO}, \frac{1}{T})$ - parameters space.

Initial oxidation of Zr

Zr has been chosen as an object of investigation since it finds a wide amount of different applications e.g. in the Three Way Catalytic Converter as a support for transition metal powders [49], in microelectronics [50] and in nuclear reactors [51].

As mentioned in section 1.1, real heterogeneous catalysts are multicomponent metal - oxide systems with very complex catalytic behaviour. Understanding of this behaviour needs, obviously, not only a change of the catalysts complexity (bridging *the materials gap*), but also understanding of the behaviour of separated component on the real catalyst (e.g. oxidic support or metal powder separately).

Since, the supporting material for the catalyst plays a significant role in the catalysts performance and, obviously, can drastically modify the activity of the catalyst [52], knowledges about behaviour of the oxidic support under the oxidation conditions coupled with obtaining information about the composition of the supporting oxidic material, structure and change of both of them during reaction are essential for understanding of the real catalyst behaviour. Also, due to the existence of the *support effect* in catalysis, it is highly desirable to achieve a precise control over the composition of the oxidic support.

Initial formation of the oxide on the Zr surface is a topic of great interest itself, because up to date there is a lack of information about formation of sub-stoichiometric surface species during initial oxidation of Zr and the role of this species in the oxidation process [53].

The main objective of this section is the investigation of the initial oxide formation on the polycrystalline Zr surface. Special emphasis is placed on the influence of the oxidation conditions, such as temperature and oxygen exposure, on the thickness and composition of the oxidic layer, which is formed during oxidation. Also, formation of sub-stoichiometric oxidic species at the very beginning of oxidation process is discussed.

CO oxidation on Pd supported by ZrO_x

Although catalytic *CO* oxidation on oxide supported *Pt* group metal is one of the frequently investigated topics in catalysis [54], there are still a lot of open questions in these area, e.g the effect of the supporting material on the reaction behaviour of the catalyst.

Up to date, most of the studies which were dedicated to this problem were based on evaluation of experimental data obtained using different spectroscopic techniques e.g. *XPS*, *IR*, etc. [55].

Although these studies resulted broader understanding of the tiny molecular processes which are hidden behind effect of the different supporting materials on the reaction behaviour of the catalytic systems, the information obtained using these techniques gives, obviously, only averaged interpretation of the problem. In other words, using these methods spatial phenomena can be hardly observed. On the other hand, scanning probe techniques like, e.g *STM* gives the opportunity to observe surface reactions with spatial resolution [28]. However, due to the scanning character of these techniques, obtaining information about real-time processes on the solid surface is hardly possible. Therefore, up to date, there is a lack of experimental information about the effect of the support on spatially coupled phenomena such as kinetic transitions, reaction-diffusion front propagation and kinetic oscillations. These processes can be understood, to the full extent, only by using experimental techniques allowing not only local spatial resolution but also ability to perform *in situ* measurements during ongoing reaction. Solving of this challenging task, at least for the case of *CO* oxidation on supported *Pd* μm - sized metal agglomerates, is the challenge of the following section.

The main objective in this section is the extension the *kinetics by imaging approach** to the investigation of two component model catalyst consisting of μm - sized metal agglomerates supported by different supports. The main emphasis, however, is placed on *Pd* agglomerates supported by *ZrO_x*. First objective is performing locally resolved measurements of ongoing *CO* oxidation reaction on *Pd* agglomerates supported by *ZrO_x*. Further, in order to shed the light on influence of the support effect to local reaction kinetics, *Pd* supported by *ZrO_x* has to be compared with local data obtained on *Pd* agglomerates supported by polycrystalline *Pt* foil. The next challenge in this

*see chapter 5 for details

section is to answer the question of how the thickness of the ZrO_x support affects local reaction kinetics of CO oxidation on Pd model catalyst, at least in 10^{-5} mbar pressure range. This goal can be achieved by the correlation of data obtained using *kinetic by imaging approach* with spectroscopic data obtained by *XPS*.

Outline and guideline of the thesis

Thesis outline

The *literature overview* chapter presents a survey about features of reactions investigated in this thesis, namely *CO oxidation on transition metals surfaces* and *initial oxide formation on Zr surfaces*. Also information about structural properties of *Rh* and *Pd* low Miller index surfaces, their reconstructions in couple with interaction with CO and oxygen with *Rh* and *Pd* surfaces is provided. An overview of oxide formation on *Rh* and *Pd* surfaces is presented. Further, the mechanism of CO oxidation on transition metal surface and some features such as bistable behaviour of such a kind of reaction are discussed. Introduction to construction of the kinetic phase diagrams and their application in catalysis research is provided. Information about the interaction of oxygen with *Zr* surfaces and formation of oxides on *Zr* surface is presented with special emphasis on probing such surfaces with *XPS* and the possibility of sub-stoichiometric oxidic species formation during initial oxidation of *Zr* surfaces.

The *experimental* chapter presents the experimental *UHV* setup, which was employed for obtaining the results presented in this thesis. Detailed description of the main parts of experimental setup, transfer system, sample holder and sample preparation facilities and cleaning procedure are presented.

The *methods* chapter introduces experimental techniques which are employed in this thesis, namely *PEEM*, *QMS*, *XPS* and *EBSD*. Theoretical background, principles of operation and short overview of the instruments design couples with the role of each certain technique in the following thesis is presented.

The *reaction kinetics by imaging approach* chapter presents an introduction to the *reaction kinetics by imaging* approach and its application to the investigation of the CO oxidation on polycrystalline metal surfaces and supported μm - sized metal

agglomerates. Experimental realization of the method using combination of *PEEM* and *QMS* techniques is discussed.

The chapter *experimental study of CO oxidation on stepped Rh surfaces* is dedicated to the presentation of experimental results of *CO* oxidation on differently oriented stepped *Rh* (hkl) domains of the polycrystalline *Rh* foil, obtained using the *reaction kinetics by imaging* approach. Main attention is paid to the construction of kinetic phase diagrams for differently oriented stepped *Rh* (hkl) domains by analysis of *PEEM* video sequences recorded during the ongoing *CO* oxidation reaction (local kinetic phase diagrams) and global (spatially averaged) kinetic phase diagram which are obtained by analysis of *QMS* data.

The chapter *XPS and PEEM study of initial oxidation of polycrystalline Zr foil* concentrates on the influence of the oxidation parameters, such as temperature and oxygen exposure, on initial oxidation of the polycrystalline *Zr* surface. Variation of oxidic layer thickness and composition by changing these parameters are presented. Additional emphases is paid to the detection of sub-stoichiometric oxidic species during initial oxidation of the polycrystalline *Zr* surface.

In the chapter *PEEM and XPS study of CO oxidation on supported Pd model catalysts*, *reaction kinetics by imaging* is extended to the case of *CO* oxidation on supported *Pd* model catalyst. The role of the support on local reaction kinetics is discussed. Additional emphasis is placed on the role of ZrO_x support thickness to local reaction kinetics of *CO* oxidation of *Pd* model catalyst.

The *conclusions* chapter summarizes the most important results of this thesis.

2 | *Literature overview*

Reactions of interest

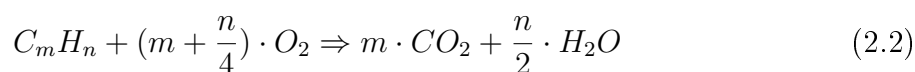
CO oxidation on Pt group metals

The *CO* oxidation reaction plays in modern heterogeneous catalysis the same important role as a *drosophila melanogaster* in genetics [55]. This importance is mainly caused by high environmental and industrial relevance and, besides, by relative simplicity and a high degree of understanding of the reaction mechanism [53].

The *CO* oxidation on transition metal surfaces is intensively investigated for the last four decades. Numerous studies from early "*classical*" studies on single crystals under *UHV* conditions [6, 56, 57] to modern "*state of the art*" experiments with size- and shape-selected nanoparticles under ambient conditions [58, 59, 60] have helped in understanding the elementary processes which contribute to the *CO* oxidation reaction mechanism. The collection of information about the fundamental properties of this reaction led also to the understanding of the non-linear character of this reaction [6, 24, 61]. Additionally, the experiments with single crystals paved the way for understanding the catalytic behaviour of more complex systems, such as oxide-supported transition metal particles and, subsequently, opened the way for bridging the *materials and pressure gap* in heterogeneous catalysis [20].

The relatively simple mechanism of the *CO* oxidation on transition metal surfaces allows to use its use as a probe reaction for testing the properties of new catalytically relevant materials both for model studies and for industrial catalysis [53]. Such studies usually include investigations of the behaviour of the reactive species (*CO* and oxygen) on the model catalyst surface, estimation of the number of the active sites per surface area for industrial catalysts, etc.

Environmental importance of the CO oxidation, as was mentioned in a section 1.1, consists mainly in the elimination of the highly toxic CO from the automotive exhausts [62] or from the by-products of incomplete combustion of hydrocarbons in petrochemical industry [55]. In the case of the car engines, the huge amounts of CO (nearly 100 %) can be effectively removed by *three way catalysts* [33], which convert CO to CO_2 (eq. 2.1) and, additionally, convert unburned hydrocarbons (eq. 2.2), and nitrogen monoxides (eq. 2.3) to environmentally friendly reaction products [62]:



From an industrial point of view, the CO oxidation reaction is relevant for hydrogen production for fuel cells, methanol synthesis, chemical elimination of CO_2 by means of the water-gas shift reaction [54].

The simplicity of this reaction is caused, mainly, by the fact, that CO oxidation has only one limiting step (i.e. surface diffusion of the CO molecules) and a sole reaction product, namely CO_2 . Since, CO_2 binds and interacts much weaker with the most of catalytic surfaces than CO , interpretation of experimental data becomes very straightforward [54]. In the gas phase, the probability of the reaction between CO and oxygen is limited by breaking of the $O-O$ bond in the O_2 molecule. The activation energy of the $O-O$ bond breaking in the gas phase is around 500 kJ/mol [63]. However, catalysts effectively promote breaking of the $O-O$ bonds in oxygen molecules and, hence, boost the CO oxidation reaction very effectively [63]. Figure 2.1 shows energy diagram of the CO oxidation on Pt group metals. The kinetics of the reaction between CO and oxygen on transition metal surfaces obeys the *Langmuir-Hinshelwood mechanism* which includes several elementary steps: adsorption of CO and oxygen on a transition metal surface, surface diffusion of CO towards the neighbouring oxygen atoms, reaction between CO and atomic oxygen and, finally, desorption of CO_2 as a reaction product [64, 65] *.

*The detailed description of Langmuir-Hinshelwood mechanism is given in a section 2.4 "Langmuir-Hinshelwood mechanism"

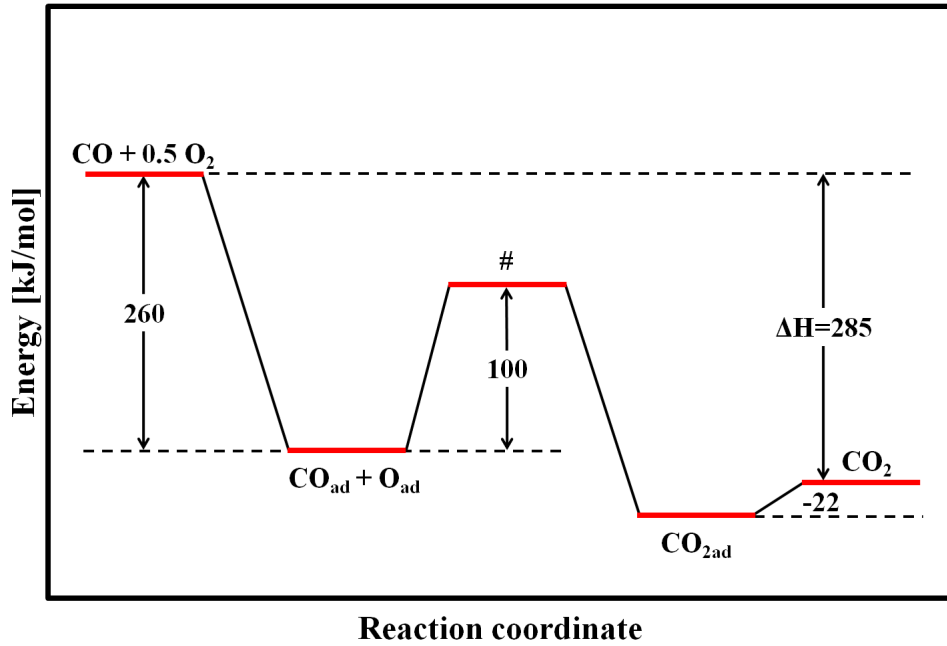
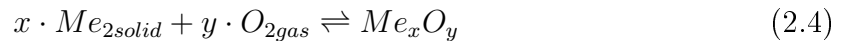


Figure 2.1: Energy diagram of the CO oxidation on Pt group metals. (The picture adapted from ref. [63].)

Initial oxidation on Zr surfaces

Upon interaction with pure oxygen or oxygen-containing atmosphere almost all metals form an oxide layer on their surfaces [66]. In general case, oxidation of metals can be expressed by the following equation [67]:



However, a detailed consideration of the oxidation process reveals numerous complex competitive and overlapping mechanisms which contribute to the oxide layer growth on the metal surface: physisorption of the molecular oxygen from the gas phase, dissociative chemisorption of oxygen, oxide islands nucleation, transport of the reactants through oxide film and continuous oxide film growth (Fig 2.2) [67].

Early experiments with oxidation of the Zr were dedicated, in most cases, only to the "raw" high temperature oxidation of Zr at atmospheric pressure, which lead to the formation of thick oxide layer [68].

The choice of such experimental conditions was dictated, on the one hand, by the

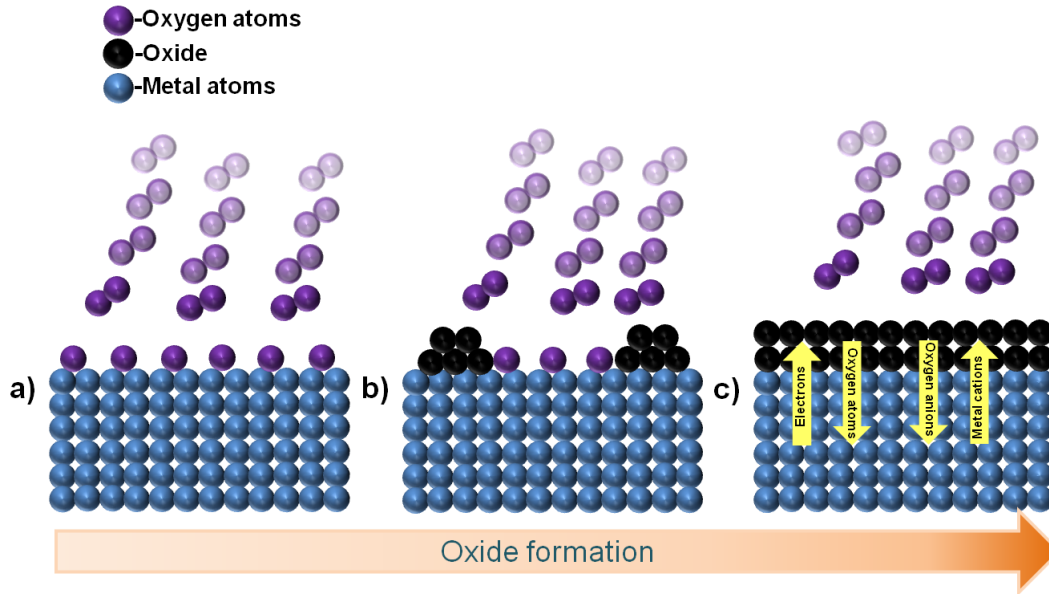


Figure 2.2: Schematical representation of different processes which occur during the thermal oxidation of metals: **a)** chemisorption of oxygen; **b)** nucleation of oxide islands; **c)** continuous film growth.

high relevance of *Zr* as a fuel cladding material for nuclear industry and the necessity for modelling the conditions, which are similar to those inside nuclear reactors and, on the other hand, by difficulties to precisely manipulate and examine the sample composition on the atomic scale.

These "*early birds*" experiments revealed general features of the oxide formation on the *Zr* surface, e.g. existence of the *fast* and *slow* stages of the oxidation process [66]. However, the innermost details of the oxidation process, which takes place at the very beginning of the oxide formation, especially at low temperature and pressure conditions, were not yet clarified.

Further development of the surface sensitive techniques such as *XPS*, *STM*, ellipsometry, etc. helped to shed more light to the processes, which take place at the very beginning of the *Zr* oxidation process [69].

One of the reasons to establish the control on the oxide layer compositions with atomic precision is that zirconia is considered as a promising candidate for the replacement of silicon in next generation electronic devices. Since, according to Moore's law, size of electronic components get smaller each several years [70], contribution of the the oxide film become crucial [71, 72].

Surface oxidation of metals can be described using several models such as Cabrera-

Mott [66], Fromhold-Cook [73] and Deal-Grove [74]. These models give rather reliable representation of the oxide film development during oxidation process, but, however, assume only homogeneous growth of the oxide layer on the homogeneous substrate by species transport through the developing oxide film. Therefore, such effects as influence of substrate structure, defects and impurities are not considered in these models. Moreover, these models do not consider changes of the developing oxide layer composition during the oxidation process, namely they do not involve formation of substoichiometric oxidic species.

Up to date, the questions about formation of substoichiometric oxidic species during initial oxidation of metallic *Zr* have been not answered to the full extent[†]. Foremost, the understanding of the *Zr* oxidation process needs a clean "*oxide-free*" *Zr* surface, which is a challenging task itself, since *Zr* has a very high affinity to oxygen [75] and therefore forms oxides very easily even under low pressure conditions. Hence, for obtaining reliable results, *UHV* conditions together with proper surface preparation and an effective cleaning procedure are necessary.

The main challenge in studying the nature of substoichiometric oxides is, that they appear at the very beginning of the oxidation process [76, 77, 78]. This is also the reason, why up to date there is no agreement about the type of the substoichiometric oxidic species which can be formed during initial oxidation of *Zr* surface.

Structure of Rh surfaces

Low Miller index Rh surfaces

Metallic rhodium has the face centred (*FCC*) lattice structure with a lattice constant of 0.38 Å. Low Miller index planes (*100*), (*110*) and (*111*) have the lowest surface energy [79, 80] and, therefore, these orientations are preferred for the *FCC* metal surfaces. Upon prolonged annealing most of the polycrystalline *FCC* metals recrystallize in crystallites with (*100*), (*110*) and (*111*) orientation. The ball models of these three crystallographic orientations are presented on Fig. 2.3.

[†]see section 2.6.2 for details

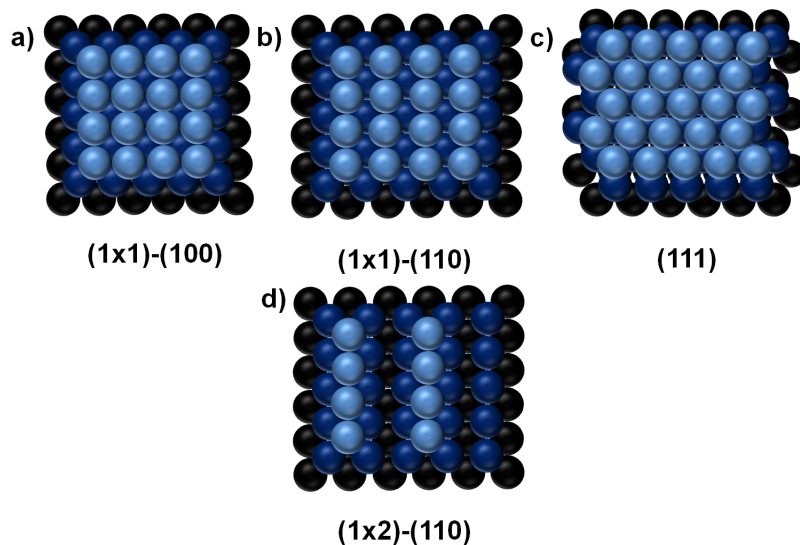


Figure 2.3: Structure of different *Rh* surfaces: **a)** $(1 \times 1)-(100)$; **b)** $(1 \times 1)-(110)$; **c)** (111) surfaces; **d)** $(1 \times 2)-(110)$ *missing row* reconstructed surface.

Rh surface reconstructions

During the reconstruction, surface atoms undergo substantial rearrangement not only in vertical but also in horizontal position [28]. The main reason of the surface reconstructions is minimization of surface free energy. Due to absence of neighbours on the next atomic layer, surface atoms have reduced coordination and, therefore, they try to minimize surface free energy by packing close together [28]. Reconstruction of different low Miller index planes can be observed by exposure of the sample surface in different gas mixtures at different temperature. Clean *Rh* (110) surface exhibits (1×1) structure (Fig. 2.3 b), which can be reconstructed in variety of *missing row* reconstructions depending on the surface preparation procedure [81, 82, 83].

Stepped Rh surfaces

Real catalysis does not occur on the low Miller index surfaces, such as *Rh* (100) , *Rh* (110) , *Rh* (111) . Therefore, it is interesting to create stepped surfaces which are mis-oriented from the low Miller index orientations [28]. These high Miller index surfaces are composed of arrays of flat terraces, which are separated by atomic steps (Fig. 2.4), which can also contain kinks. The example of a stepped *Rh* (755) surface is presented in the Figure 2.4.

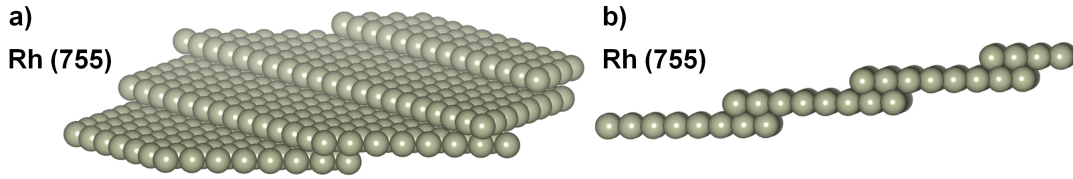


Figure 2.4: The ball model of the stepped $Rh(755)$ surface.

For the proper description of the orientation of stepped surfaces, Lang, Joyner, and Somorjai introduced a notation which describes the stepped surface through the orientation of the terrace, orientation of the step and number of the atoms in a terrace and a step [84]. The notation which describes the orientation of a stepped surface looks as follows:

$$n \cdot (h_t k_t l_t) \times m \cdot (h_s k_s l_s) \quad (2.5)$$

Here $(h_t k_t l_t)$ and $(h_s k_s l_s)$ represent the Miller indices of the terrace and the step respectively, n - and m - atomic rows in the terrace and atomic height (i.e. number of the atoms) in the step, respectively. Using the notation 2.5, the $Rh(755)$ surface can be represented as $6 \cdot (111) \times (100)$ or as surface consisting of (111) -oriented terrace of six atomic rows wide and a (100) -oriented step of one atom height.

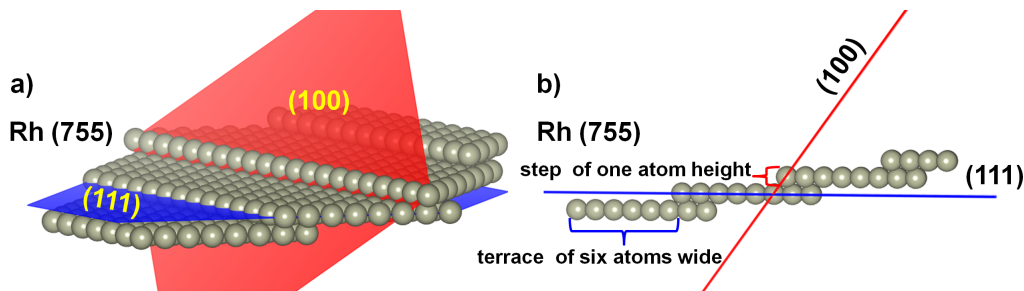


Figure 2.5: A $Rh(755)$ stepped surface with marked orientation of a terrace (blue plane) and of a step (red plane).

CO and oxygen interaction with Rh and Pd surfaces

CO adsorption on Rh and Pd surfaces

CO adsorption on *Pt* group metal surfaces is one of the most frequently investigated and well-understood adsorption problems in surface science. On *Rh* and *Pd* surfaces, CO adsorbs molecularly with carbon pointing towards the metal surface. The model describing CO adsorption on the *Pt* group metal surfaces was developed by G. Blyholder (*Blyholder model*) [85]. Schematically, this model is presented on the Fig. 2.6.

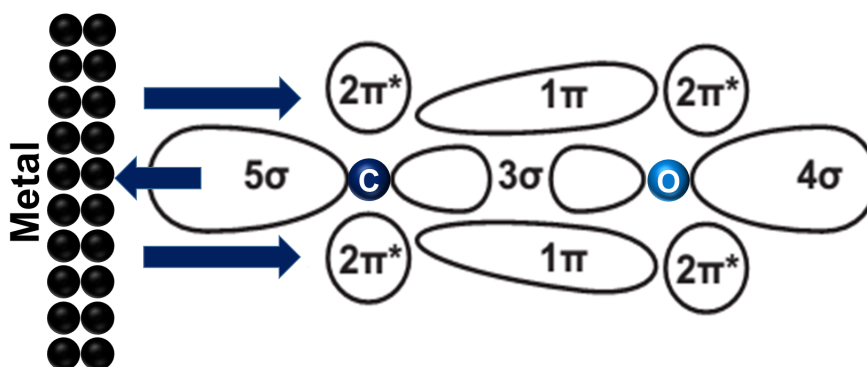


Figure 2.6: Blyholder model of CO adsorption on *Pt* group metal surfaces.

In this model two orbitals of the CO molecule (acceptor) and the *d*-band of the metal (donor) are involved. Bonding of the CO molecule on *Pt* group metal surfaces takes place through the transfer of electrons from the 5σ highest occupied molecular orbital (*HOMO*) of adsorbing CO molecule to *d*-band of the metal. Also, back donation of electrons from *d*- and *p*- band of metal to the 2π* of CO molecule, which is lowest unoccupied orbital (*LUMO*) takes place. As a result, the bond between the metal surface and the CO molecule become stronger, while the bond between carbon and oxygen atoms in the CO molecule become weaker in comparison with the gas phase. Adsorption properties of CO on *Rh* and *Pd* single crystalline surfaces are strongly dependent on the crystallographic orientation of the surface. Experimental estimation of the heat of CO adsorption on *Rh* low Miller index single crystalline surfaces showed that the heat of CO adsorption increases with the increase of the metal atoms packing density in the following order $E_{ads}(Rh(110)) < E_{ads}(Rh(100)) < E_{ads}(Rh(111))$ [86]. For *Rh*(111) and *Rh*(110), the initial heat of CO chemisorption has been determined as 132 kJ/mol [87, 88] and 130 kJ/mol [89, 90] respectively. On the other hand, for

Rh (100), the initial heat of chemisorption has been estimated as 125 kJ/mol [87, 88]. In general, the heat of *CO* chemisorption for *Pd* and *Rh* single crystalline surfaces decreases with increase of *CO* coverage θ_{CO} . On the *Rh* (110) surface, *CO* adsorbs with the initial sticking coefficient of 0.68 in the temperature range 373 - 473 K and shows coverage dependence, namely decrease of the sticking coefficient with increase of *CO* coverage [91].

In turn, for *CO* on *Pd*, the dependence between the heat of *CO* chemisorption and atomic packing density for *Pd* (hkl) surfaces has a reverse order $E_{ads}(Pd(111)) < E_{ads}(Pd(100)) < E_{ads}(Pd(110))$ [86]. Initial heat of *CO* adsorption on *Pd* (100) is 153 kJ/mol and on *Pd* (110) and on *Pd* (111) it is 167 kJ/mol and 142 kJ/mol [64] respectively. The initial sticking coefficient for *Pd* (100) is in a range of 0.6 - 0.8 [92, 93]. For *Pd* (110) and *Pd* (111) clean surfaces, the initial sticking coefficient is unity. Desorption of *CO* from *Pd* (110), *Pd* (100) and *Pd* (111) starts at temperatures higher than 450 K [92, 94, 95, 99].

Oxygen adsorption on Rh and Pd surfaces

In contrary to *CO*, oxygen adsorbs dissociatively on *Rh* and *Pd* single crystalline surfaces. Interaction of oxygen with low Miller index *Rh* surfaces was extensively studied revealing a huge variety of adsorption structures which can be formed on these surfaces. On *Rh* (111), oxygen adsorbs dissociatively in disordered state even at temperature of 150 K [100]. Desorption temperature of oxygen from the *Rh* (111) was determined in different studies in a wide range between 700 K and 1250 K [101, 102]. Such a wide range can be explained by differences in heating rates in different experiments. A thermal desorption spectrum measured for *Rh* (100) showed appearance of three desorption peaks β_1 , β_2 and β_3 (Fig 2.7) [103]. Desorption temperature for these peaks was determined as following β_1 - 820 K, β_2 - 920 K, β_3 - 1200-1350 K. Desorption peak β_3 corresponds to desorption of atomic oxygen. In contrast to this, desorption peak β_2 corresponds to desorption of molecular oxygen [103]. The *Rh* (110) desorption spectrum exhibits 5 desorption states β_1 , β_2 , β_3 , β_4 and β_5 which appears in wide temperature range from 797 K to 1150 K (Fig 2.8). Desorption states β_1 , β_2 , β_3 , β_4 corresponds to first order desorption and β_5 state to second order desorption [104].

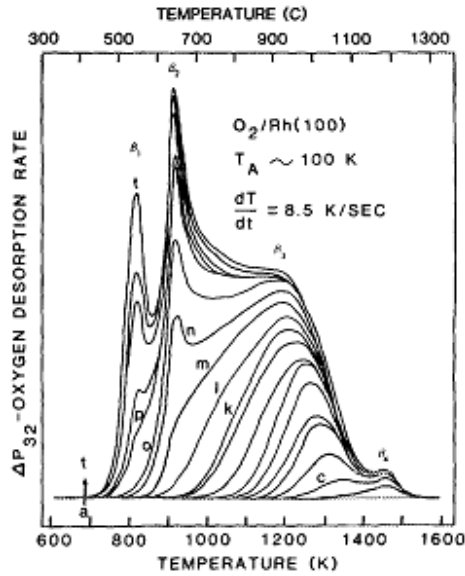


Figure 2.7: The oxygen desorption spectrum for $Rh(100)$ single crystalline surface. The original picture is take from ref. [103].

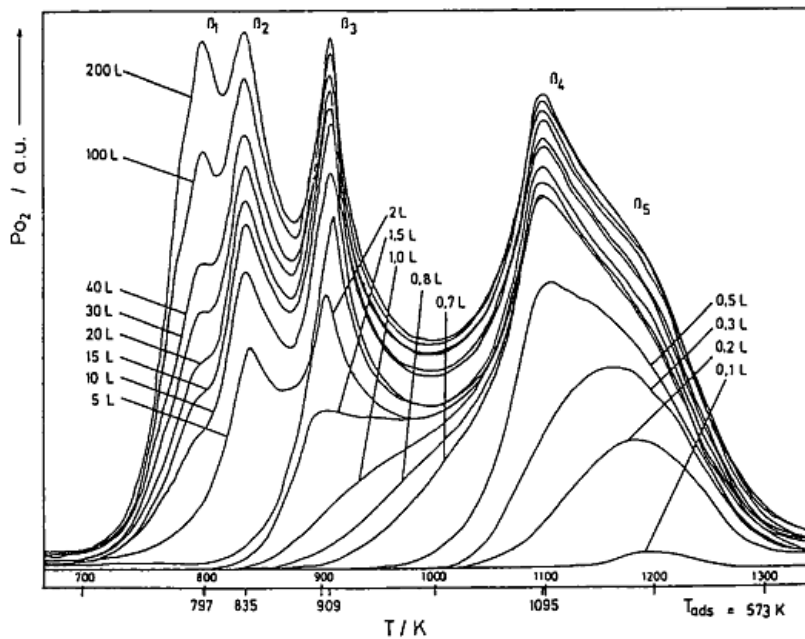


Figure 2.8: The oxygen desorption spectrum for $Rh(110)$ single crystalline surface. The original picture is take from ref. [104].

On $Pd(110)$ and on $Pd(100)$ oxygen adsorbs in both atomic and molecular states at the temperature of 100 K [96, 105, 106, 107], with sticking coefficient ranging from 0.1 to 0.75 [108]. Dissociative adsorption of oxygen on $Pd(111)$ was reported at temperature below 80 K [107, 108].

Diffusion

Surface diffusion is a process which is associated with motion of the adsorbed species, such as adatoms, molecules, atomic clusters, etc. on the solid or liquid surface. On the solid surface, the adsorbed species occupy specific adsorption sites which are the positions of the local minimum of the potential energy on the *potential energy surface*

(Fig 2.9). Surface diffusion proceeds by means of motion of the adsorbed species from one adjacent adsorption site to another. Diffusion is a thermally activated process, hence in order to diffuse from one adjacent adsorption site to another, diffusing species has to overcome the energy barrier E_A^{diff} . This barrier is called *activation energy*. For successive surface diffusion, the barrier E_A^{diff} has to be smaller than the desorption energy E_{des} . Otherwise, the desorption process will dominate over the diffusion [28].

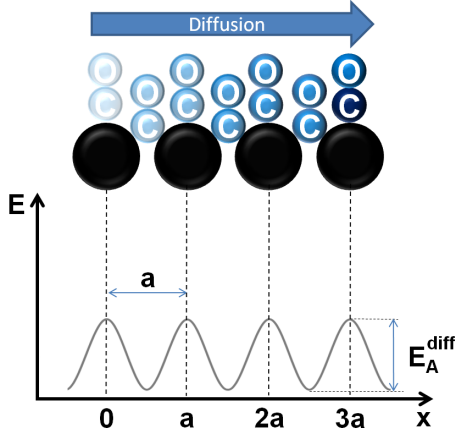


Figure 2.9: Schematic representation of surface diffusion of the adsorbed molecule in one-dimensional case. In order to diffuse from one adsorption site to another, adsorbate has to overcome diffusion barrier E_A^{diff} . Taken from ref. [28].

In a case of the surface diffusion, two regimes have to be mentioned. At high surface temperatures, when $kT \gg E_A^{diff}$, adsorbed species move freely along the surface. In contrast to this, at low surface temperatures, when $kT < E_A^{diff}$, adsorbed species hop from one adjacent adsorption site to another by *hopping mechanism*. According to this mechanism, adsorbed species oscillate in the potential well (adsorption site) with frequency ν_0 until they get thermally activated by the energy exchange between the adspecies and the substrate. Then, these adsorbed species will overcome the barrier E_A^{diff} and hop to another adsorption site. For heterogeneously catalysed reactions, the *hopping mechanism* reliably describes behaviour of the adsorbed species.

The distance, which a diffusing molecule can overcome within one hop on the surface with interatomic spacing a for the time t (*hopping distance*) is determined by following equation [28]:

$$\langle \Delta r^2 \rangle = \nu \cdot a^2 \cdot t \quad (2.6)$$

The hopping frequency ν in eq. 2.6 is expressed by following equation:

$$\nu = \nu_0 \cdot \exp\left(\frac{-E_A^{diff}}{k_B \cdot T}\right) \quad (2.7)$$

For the case of *tracer diffusion* which, in an ideal case, is the diffusion of a single adsorbed particle on the surface, i.e. when coverage Θ is low ($\Theta = \frac{N_{ads}}{N_{tot}}$), the diffusion coefficient (D^*) is given by:

$$D^* = \frac{\nu \cdot a^2}{z} \cdot \exp\left(\frac{-E_A^{diff}}{k_B \cdot T}\right) \quad (2.8)$$

In the case of the *tracer diffusion*, the diffusion coefficient D^* describes the path (or the trace) of individual adsorbed particles on the surface.

For the most of processes which are involved in the heterogeneously catalysed reactions, the surface coverage Θ is high enough to allow *chemical diffusion* to take place. *Chemical diffusion is a collective process, occurs in the presence of a concentration gradient and results in a net mass transfer.* In this case, the diffusion can be described by the first and second *Fick's laws*:

$$(I) \quad J = -D \cdot \nabla \Theta(r, t) \quad (2.9)$$

$$(II) \quad \frac{\partial \Theta(r, t)}{\partial t} = D \cdot \nabla^2 \Theta(r, t) \quad (2.10)$$

Here, J - is the diffusion flux and D - the diffusion coefficient of the chemical diffusion which is not always equal to D^* .

The diffusion coefficient D can be obtained by measuring the evolution of the surface coverage Θ which can be estimated by real-time observation of the surface diffusion by *photoemission electron microscopy* [111]. By analysing of the *PEEM* video data it is possible to obtain information about the evolution of the concentration profile of the diffusing species (e.g. *CO* molecules) at certain temperature and hence estimate the value of the diffusion coefficient. By plotting the diffusion coefficient values as a function of the reciprocal temperature in an Arrhenius plot, the activation energy E_A^{diff} and the pre-exponential factor D_0 can be estimated. In ref. [112], by using a combination of *PEEM* and *LITD* techniques, e.g the diffusion coefficient for *CO* diffusion on *Pd(111)* and its dependence on the *CO* coverage Θ was obtained in this way. The diffusion coefficient can exhibit *orientational anisotropy* and *directional anisotropy*. Since surfaces of the different crystallographic orientations have different atomic structure,

they exhibit a different relief of the *potential energy surface*. Therefore, the diffusion coefficient for the same species but adsorbed on surfaces of different crystallographic orientation may be different (so-called *orientational anisotropy*). Since the surfaces of certain crystallographic orientation can exhibit a anisotropy of their structure in different crystallographic directions, the value of the diffusion coefficient in different direction may be different (so-called *directional anisotropy*). In the case of *Pt* single crystalline surfaces, e.g. directional anisotropy for *CO* diffusion was reported for a *Pt* (110) (1×1) surface in ref. [113].

Oxide formation on Rh and Pd surfaces

The oxidation of a *Rh* surface can be divided into several elementary steps: dissociative chemisorption of oxygen, dissolution of the oxygen in the bulk, formation of the surface- and then bulk oxides [113, 114, 115]. Field emission experiments performed in ref. [114] showed that dissolution of the oxygen into the bulk is more probable on more open surfaces.

Surface oxide formation on *Rh* (hkl) and *Pd* (hkl) single crystalline surfaces was investigated in a wide range of oxygen partial pressures. In the case on low Miller index *Rh* single crystalline surfaces, formation of the surface oxide starts at the oxygen partial pressure range of $10^{-5} - 10^{-3}$ mbar depending on the packing density of the surface atoms. Upon interaction with the oxygen at "oxidation conditions", a surface trilayer oxide can be formed [116].

On *Rh* (111), an exposure in 2×10^{-4} mbar of oxygen at 800 K leads to formation of a trilayer (8×8) hexagonal *Rh* oxide on a *Rh* (9×9) metallic substrate. *DFT* calculations revealed that the most thermodynamically stable oxide phase at these conditions is *RhO₂* (8×8) on *Rh* (9×9) [117].

On *Rh* (100), formation of the surface oxide starts at oxygen partial pressures of 10^{-4} mbar at 700 K. At these conditions, a surface trilayer *O-Rh-O* oxide with structure *c* (8×2) is formed [118]. On *Rh* (110), in turn, oxidation at 10^{-4} mbar of oxygen leads to formation of the *c* (4×2) surface oxide [119].

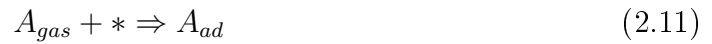
Upon oxidation of *Pd* surfaces bulk, or surface oxide species can be formed. Exposure of *Pd* (100) surfaces in oxygen in the pressure range of 10^{-6} to 1 bar at temperature

range of up to 1000 K depending on experimental conditions leads to formation of bulk or surface oxides [120]. In turn, on *Pd* (110) formation of only bulk oxides was observed [121].

Langmuir-Hinshelwood reaction mechanism

Langmuir-Hinshelwood (L-H) reaction mechanism was first suggested by Irwing Langmuir (1921) and then developed by Cyril Hinshelwood. This mechanism describes a surface reaction between two adsorbed species on the solid surface with subsequent desorption of resulting reaction product.

In general, for two reactants A and B and resulting product C, the L-H mechanism can be expressed by following set of equations [122, 123]:



The index "gas" is denoted to the species in a gas phase and index "ad" - to the adsorbed species. As was mentioned in section 2.1.1, *CO* oxidation on *Pt* group metals obeys *Langmuir-Hinshelwood kinetics* (Fig 2.10).

For the case of the *CO* oxidation on the *Pt* group metals, the L-H mechanism can be expressed using following set of equations [64, 65]:



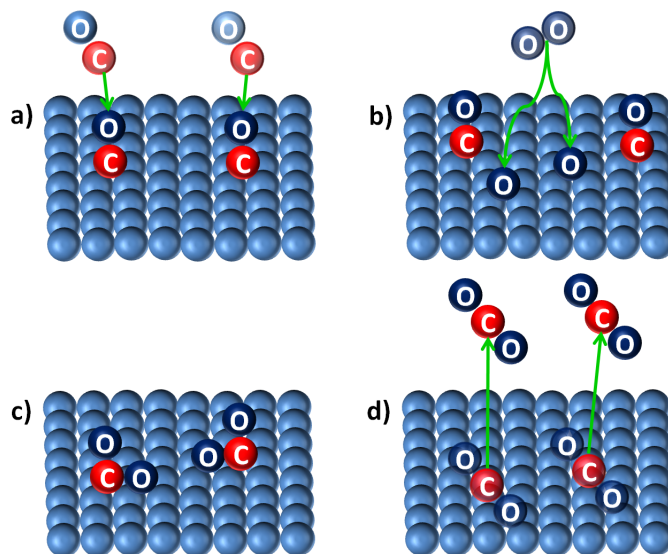


Figure 2.10: Schematic representation of the Langmuir-Hinshelwood mechanism for the CO oxidation on transition metal surfaces: **a)** molecular adsorption of CO ; **b)** dissociative adsorption of oxygen; **c)** diffusion of the adsorbed CO molecules towards the adsorbed oxygen atoms with subsequent reaction between them; **d)** desorption of CO_2 .

Eq. 2.16 describes dissociative adsorption of oxygen onto transition metal surface and eq. 2.17, in turn, molecular chemisorption of CO on transition metal surface. CO chemisorbs molecularly and therefore occupies only one adsorption site (Fig. 2.6 a). Oxygen however, needs two absorption sites on the surface for dissociative atomic adsorption (Fig. 2.6 b).

The next step is the reaction between chemisorbed CO and atomic oxygen (eq. 2.18). Diffusion of dissociatively chemisorbed oxygen atoms along the surface can be neglected. In turn, chemisorbed CO molecule easily diffuses along the surface. CO diffusion is the rate limiting step of the surface reaction between molecularly adsorbed CO and dissociatively adsorbed atomic oxygen. The diffusing CO molecule reacts with the oxygen atom forming, CO_2 as a reaction product (eq. 2.18). Since binding of CO_2 molecules with transition metal surfaces is weak, CO_2 desorbs and leaves two free adsorption sites which can be used for the next reaction cycle (eq. 2.19).

Despite the relatively simple mechanism of the CO oxidation reaction, this reaction has a specific feature which has to be specially underlined: for effective adsorption on the transition metal surface oxygen needs two adsorption sites, in contrary to the single site adsorbed CO . Adsorbed CO forms densely packed adlayers and hence

blocks dissociative adsorption of the oxygen, while leads to "*CO poisoning*" of the surface. Adsorbed oxygen atoms, in turn, form relatively open structures which do not affect the *CO* adsorption, that means that dissociatively adsorbed oxygen atoms do not block *CO* adsorption [124]. This "asymmetry" in the adsorption properties of *CO* and oxygen leads to the *asymmetric inhibition* of the reaction, which is reflected in the fact that depending on the control parameters, like *CO* partial pressure and surface temperature, the catalyst surface can be either in *active steady state* (i.e oxygen covered) or *inactive steady state* (*CO* covered). Also, the *CO* oxidation reaction exhibits bistable behaviour, which means that the system can reside at both stable steady states at the same control parameters like temperature and *CO* and oxygen pressure.

Bistability and kinetic phase diagram

Despite the relatively simple reaction mechanism, the *CO* oxidation on transition metal surfaces shows two eminent features which demonstrate the non-linear behaviour of this reaction and hence make this reaction an interesting subject for experimental and theoretical studies. These features are *bistability* [125] and *kinetic oscillations* [24]. Bistability means that the system can stay in two different states at the same set of parameters, i.e. in the case of the *CO* oxidation on transition metal surfaces, in an active steady state and in an inactive steady state at the same *CO* and oxygen partial pressures and temperature. The bistable behaviour of the *CO* oxidation on transition metal surfaces is reflected in the existence of a hysteresis for this system at cyclewise varying of the one of parameters. The expected R_{CO_2} hysteresis loop at varying *CO* partial pressure at constant oxygen partial pressure and constant temperature and the experimentally observed hysteresis measured during the *CO* oxidation on the polycrystalline *Pd* foil at constant oxygen partial pressure of 1.3×10^{-5} mbar and at constant temperature of 453 K [126] are presented in the Fig. 2.11 a, b.

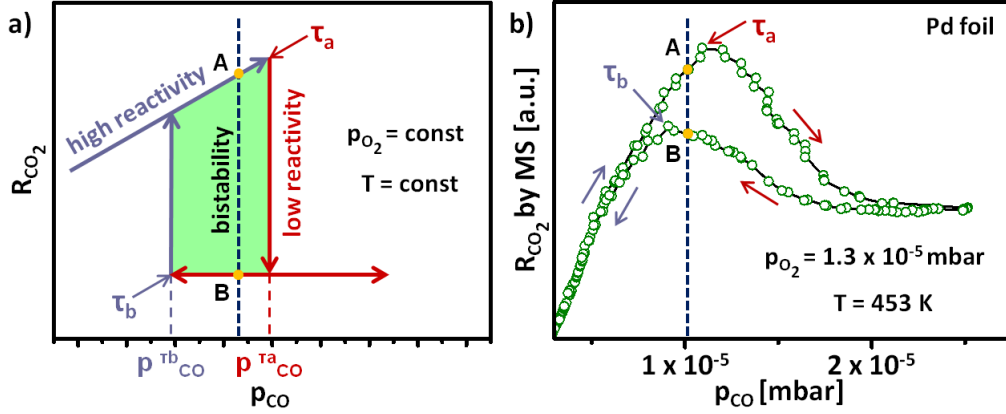


Figure 2.11: The R_{CO_2} hysteresis loop during CO oxidation on transition metal surfaces: a) schema of the hysteresis of the CO_2 production rate in the CO oxidation during the cyclic variation of the CO partial pressure at constant temperature and constant oxygen partial pressure; b) R_{CO_2} hysteresis measured by QMS during the CO oxidation on the polycrystalline Pd surface at constant oxygen partial pressure of 1.3×10^{-5} mbar and constant temperature of 453 K. Adapted from ref. [126].

At low CO pressures, the CO_2 production rate R_{CO_2} is low. The surface is covered by oxygen and resides in the *active steady state*. By increasing of the CO partial pressure, the R_{CO_2} increases linearly as long as the surface is oxygen covered, until the CO partial pressure reaches the critical value of $p_{CO}^{\tau_a}$. At this, so-called first transition point τ_a , the system experiences a *kinetic transition* from the *active steady state* to the *inactive steady state* and, as the result, the R_{CO_2} rapidly decreases. The reason of this rapid decrease of the R_{CO_2} is *poisoning* of the catalyst surface by CO , where the molecularly adsorbed CO achieves a coverage sufficient for blocking the adsorption sites which are necessary for the dissociative oxygen adsorption.

When one decreases the CO partial pressure, the R_{CO_2} remains very low, the system remains in the inactive steady state even at $p_{CO} < p_{CO}^{\tau_a}$. Only at $p_{CO}^{\tau_b}$, which is much lower than $p_{CO}^{\tau_a}$, the system switches again to the active steady state. The transition from the inactive to active state (τ_b) occurs at $p_{CO}^{\tau_b} \ll p_{CO}^{\tau_a}$. The reason why $p_{CO}^{\tau_b} \ll p_{CO}^{\tau_a}$, as already mentioned, *asymmetric inhibition* of the oxygen adsorption by CO . Between transition points τ_a and τ_b the system is bistable. In contrast with this, in the regions *above* τ_a and *below* τ_b the system is *monostable*. The width of the bistability region is dependent at the constant p_{O_2} on the surface temperature (Fig. 2.12 c).

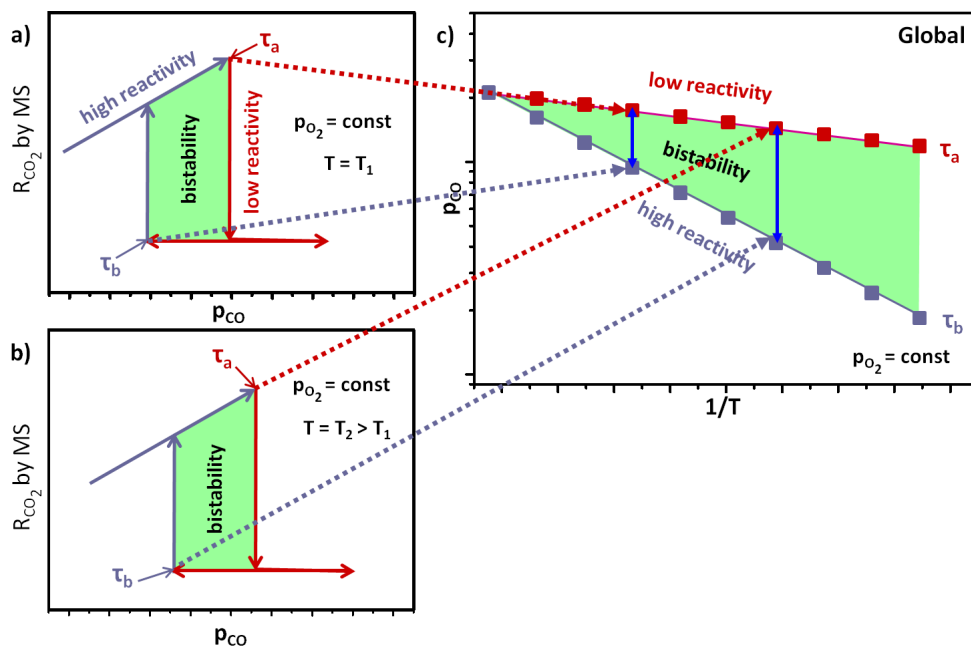


Figure 2.12: Schema of construction of a kinetic phase diagram: **a)** the hysteresis loop at a temperature T_1 and a constant p_{O_2} ; **b)** the same but at T_2 ; **c)** the kinetic phase diagram constructed from the transition points τ_a and τ_b corresponding to CO hysteresis curves in **(a)** and in **(b)**.

The plot of the transition points τ_a and τ_b as a function of the reciprocal temperature in a $(p_{CO}, \frac{1}{T})$ -parameter space illustrates the kinetic behaviour of the catalytic system (Fig. 2.12 c). This type of the plot is called *kinetic phase diagram*. Such a diagram summarizes the possible states of the catalytic system and provides direct information about the catalytic behaviour of the system within the studied range of pressure and temperature.

Comparison of the kinetic phase diagrams obtained for the catalytic systems of different structure [127], composition and complexity [128] at identical pressure and temperature conditions gives a possibility for the direct comparison of the catalytic properties of the systems in a wide range of pressures and temperatures. Thus, it paves a way for the correlation between the structure and the composition of the catalysts with their reactivity in a direct and straightforward manner.

Interaction of oxygen with Zr surfaces

Adsorption

In the case of the low Miller index surfaces of technologically relevant noble metals it is generally considered that oxygen adsorbs dissociatively on the metal surface. At moderate oxygen coverages and surface temperatures, the dissociated oxygen occupies adsorption sites above the sample surface. Similarly to *Pd* and *Rh*, in the case of *Zr*, oxygen adsorbs dissociatively, but it tends to also occupy the subsurface sites even at temperatures lower than room temperature [129]. Sample heating leads to diffusion of oxygen into the bulk.

On *Zr* (0001), upon adsorption of 0.5 ML of oxygen, the oxygen atoms penetrate into the subsurface region and remain stable there until 573 K. However, at higher temperature diffusion into the bulk takes place. These subsurface sites can be occupied by oxygen even at 90 K and oxygen population in these sites increases with increasing temperature until it reaches 100 % at 493 K [130].

For *Zr* (10 $\bar{1}$ 0) – (2 × 4) *LEED*, *AES* and work function measurements also showed that oxygen preferably occupies subsurface sites [130]. Work function measurements performed during oxygen adsorption on the *Zr* (0001), showed that penetration of oxygen atoms into the subsurface sites leads to a decrease of the sample work function, but bulk diffusion increases the value of the work function [130].

Wang et al. proposed a multiple layer adsorption model where 0.25 ML of oxygen occupy sites between first and second subsurface layer and another 0.25 ML of oxygen are placed between the second and third layer [131]. In the study performed in ref. [132], it was found that the sticking coefficient for the oxygen does not depend on the temperature and can be assumed as 1.

Formation of zirconium oxide

As was mentioned in section 2.1.2, oxidation of metal surfaces involves several processes e.g: dissociative chemisorption of oxygen, nucleation of oxide islands, growth of the oxide islands and formation of the continuous oxide film.

The *XPS* studies of initial oxide formation on *Zr* revealed that formation of oxide

species already take place at very low oxygen exposure, e.g. the ZrO_2 peak appears on the Zr polycrystalline surfaces already at the exposure 4 L [76] of oxygen at room temperature.

The *STM* studies of the initial oxide formation on single crystalline Zr (0001) and Zr (10 $\bar{1}$ 0) surfaces showed that exposure in oxygen for 300 s at 1×10^{-6} mbar and in the temperature range of 300 - 450 K leads to formation of the oxide layer which become thicker with an increase of the oxidation temperature [133].

Molecular dynamics simulations performed in ref. [134] showed that the kinetics of the oxide growth on the Zr (0001) single crystalline surface can be divided into two stages. The first, fast oxidation stage, proceeds at the very beginning of the oxidation process at low oxygen exposures and, subsequently, at low oxide thickness. The second, slow oxidation stage follows the fast stage and starts at higher oxygen exposure.

The study performed in ref. [69] also showed that initial oxidation of polycrystalline Zr surface at oxygen pressure of 1×10^{-8} mbar in the temperature range of 373 - 773 K also can be subdivided into two stages (fast and slow respectively). The fast stage occurs at lower oxidation temperatures (≤ 423 K) and the second, slow stage, subsequently, at higher oxidation temperatures (≥ 423 K). During the fast stage rapid formation and growth of the oxide layer takes place which reaches the limiting thickness at the end of the first stage. The second stage is associated with the continuous growth of the oxide layer [69]. During the second stage, the thickness of the stoichiometric oxide overlayer follows the linear growth law, namely the linear dependence between the increase of the oxide layer thickness and oxidation time at constant temperature and constant oxygen partial pressure [66].

Based on the *XPS* measurements, formation of the substoichiometric species during initial oxidation of Zr was considered [76][‡].

Probing of ZrO_x surfaces by XPS

Interpretation of Zr chemical shifts in XPS

The fact that each particular element has a characteristic binding energy associated with each core atomic orbital, makes X-ray photoelectron spectroscopy (*XPS*)

[‡]See section 2.7.2 for details

a method with an ultimate elemental sensitivity[§]. In addition, the *XPS* spectrum contains not only the information about the elemental composition of the sample, but also about the chemical state of the elements distributed in the surface region of the sample [135].

The information about the chemical state of the element of interest can be directly extracted from the binding energy of the core level peaks or, more precise, from the shift of the corresponding core level peak in comparison with the core level peak of the pure element. This shift of the core level peak positions in the *XPS* spectrum is called *chemical shift* [136].

The meaning of the *chemical shift* can be explained in a simplified way from the electrostatic consideration using the *charge potential model*, which considers an atom as a sphere of radius r . This sphere consists of valence electrons with charge q and resulting potential inside the sphere is $v = \frac{q}{r}$. Any change of the chemical state e.g. change of the atom oxidation state or formation of new compounds due to chemical reaction, will disturb valence electrons and, subsequently, will change the binding energy of the electrons in a atom.

The change of the binding energy E_B^i in comparison with the binding energy of an electron in undisturbed atom E_{ref}^i can be estimated using following formula:

$$E_B^i = E_{ref}^i + kq_i + \sum_{i \neq j} \frac{q_i}{r_{ij}} \quad (2.19)$$

The change of electron binding energy in an atom can occur due to the change of q (atom charge or density of valence electrons). In order to make it more clear, eq. 2.19 can be expressed in different way:

$$E_B^2 - E_B^1 = k \cdot (q_2 - q_1) + (v_2 - v_1) \quad (2.20)$$

From the first term one can clearly see that the change of the charge of the atom (density of valence electrons) due to the reduction or oxidation leads to a change of the core electrons binding energies. For most chemical elements, the value of the *chemical shift* of core level peak in comparison with the pure elements core level peak is several eV [63].

[§]For more details about *XPS* see section 4.2 "X-ray photoelectron spectroscopy"

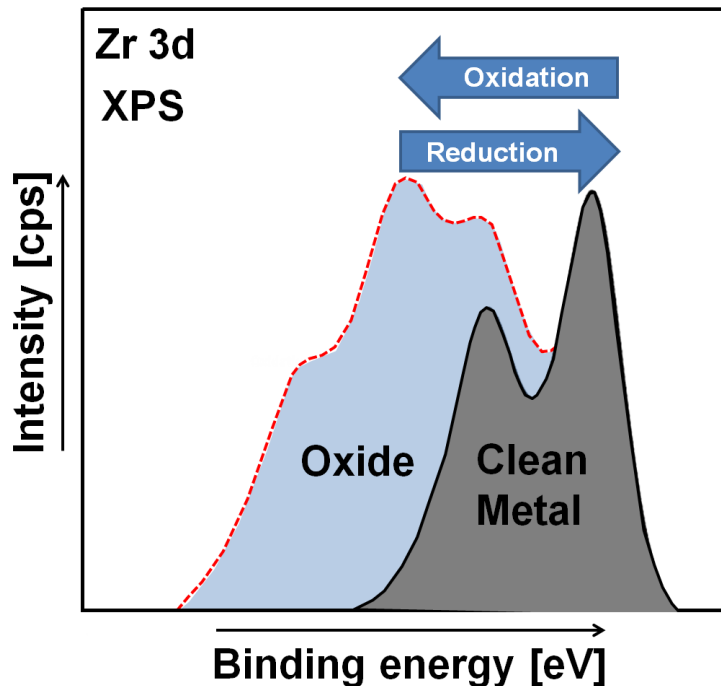


Figure 2.13: Chemical shift (schematically) of $Zr\ 3d$ peak due to the oxidation or reduction of the Zr .

The direction of the *chemical shift* is dependent on the electronegativity of elements, which are forming the new chemical state. Due to the fact that electronegativity for oxygen (3.5) [137] is higher than for Zr (1.4) [137] oxygen will attract valence electrons from Zr and therefore, the $Zr\ 3d$ core level peak upon oxidation will shift to the direction of higher binding energy and upon reduction to the direction of lower binding energy in comparison with the $Zr\ 3d$ core level peak for pure Zr (Fig. 2.13).

Formation of substoichiometric oxidic species on the Zr surface

Despite of the extensive study of Zr oxidation, some "fine" details of this process remain unrevealed. One of them is the possible formation of the substoichiometric species during initial oxidation of Zr .

Concerning to the issue of formation of the substoichiometric oxidic species during initial oxidation of Zr , there are still disagreements in the literature about the existence of the substoichiometric oxides and about the number of the suboxidic species which can be formed during initial oxidation of Zr . Most of the evidences for the existence of ZrO_x substoichiometric species during initial oxidation of Zr are based on the deconvolution of XPS spectra obtained from oxidized polycrystalline or single crystal

Zr surfaces [69, 76, 138]. In studies [76, 138], the amount of suboxides is suggested to be 3 (Zr^{+3} , Zr^{+2} and Zr^{+1}). The main argument which is presented in these *XPS*-based studies is the inability to obtain an appropriate fitting with only two species i.e. Zr^0 (metallic *Zr*) or Zr^{+4} (ZrO_2). The possibility of the existence of 4 oxidation states (3 suboxides and 1 stoichiometric oxide) is proposed in the ref. [76] on the basis that there are four possible coordinations of *Zr* atoms with oxygen (ZrO_2 or Zr^{+4} , Zr_2O_3 or Zr^{+3} , ZrO or Zr^{+2} and Zr_2O or Zr^{+1}). In the study [76], it was suggested that spacing between different oxidation states (i.e. chemical shift) has to be equal due to the fact, that the Madelung energy and ionization energy, which contribute to the value of the chemical shift are proportional to the oxidation state. On the other hand, the experiments performed in ref. [69] using monochromatized *XPS* in couple with a spectrum reconstruction method [139, 140] revealed formation of only two suboxides. The same number of suboxides formed on a polycrystalline *Zr* after oxygen exposure of 5 L at room temperature was detected in ref. [141].

Whereas the number of the appearing suboxides is still under debate, a principal consensus seem to be achieved in the question of the existence of the substoichiometric oxides in the region between stoichiometric ZrO_2 and the metallic substrate.

Information about the distribution of the oxidic species in the oxidised *Zr* sample can be obtained using the *atom probe tomography* technique (*APT*) [142]. By means of the *APT* technique, Wadman in ref. [143] showed formation of *Zr* oxide species with composition close to ZrO in the region between ZrO_2 and metallic *Zr*. Using the same technique for investigations of oxidation of *Zr* alloys, it was shown that formation of suboxidic phases during oxidation process takes place at the stoichiometric oxide-metal interface [144]. Quantitative analysis of the oxygen profile across the oxide-metal interface obtained by EELS for oxidized *Zr* alloys showed formation of suboxide phases in the region between ZrO_2 and *Zr* during oxidation process at the interface [145]. Also, on the basis of *AES* measurements it was shown that formation of $\alpha - ZrO$ at the interface region between ZrO_2 and *Zr* takes place [146].

An important question is the kinetics of the substoichiometric oxide growth. In the study performed in ref. [69], it was revealed that oxidation of the *Zr* is a two stage process and that formation of suboxidic layer starts during the first "fast" oxidation

stage and reaches its limiting thickness at the end of this stage. The value of the limiting thickness of the oxidic interlayer increases with the increase of the oxidation temperature. The second, "slow" stage, in turn, is associated with the formation of only stoichiometric ZrO_2 . In the study performed in ref. [138] it was suggested that the substoichiometric oxidic species may act as a precursors for the growth of the stoichiometric ZrO_2 .

The main difficulty in investigating of the kinetics of suboxidic species growth is that they appear at very low oxygen exposures and their contribution to the whole oxidic layer, in comparison with stoichiometric oxide, is small. This makes the observation of sole suboxidic layer formation a very challenging task.

3 | *Experimental*

The ultrahigh vacuum system

The results which are presented in the present thesis are obtained using the multifunctional ultra-high vacuum (*UHV*) experimental setup which is presented in Fig. 3.1. The setup consists of two separated *UHV* chambers which are connected via a load lock. One of the chambers is equipped with a *PEEM* (photoemission electron microscope, *PEEM* 150, STAIB instruments) and a *QMS* (quadrupole mass spectrometer, *e* – Vision⁺, MKS Instruments). As the excitation source for the *PEEM*, an *UV* deuterium discharge lamp with the cut off energy of 6.8 eV is used. The base pressure inside the chamber is 10^{-9} mbar. It is achieved using an *IGP* (ion getter pump, Vacion Plus 500, Varian) for pumping the system in a stand by mode, i.e. when no experiments are performed and by a combination of the rotary vane backing pump (TriVac D8B, Leybold) and a turbomolecular pump (TMU 260, Balzers) during the experiments. In addition, for the pumping of the residual hydrogen, a titanium sublimation pump (Varian) was used. For removing residual water, the whole *UHV* setup was regularly baked out at $T \approx 403$ K. In order to keep the pressure inside the *PEEM* imaging column lower than 5×10^{-7} mbar, the *PEEM* electron optics was pumped out by means of the rotary vane pump and a turbomolecular pump (TMU 071P, Pfeiffer Vacuum). The monitoring of the pressure in the chamber is performed by a Bayard-Alpert hot cathode ionization gauge (Varian) and by a combined Pirani and a cold cathode pressure gauge (PKR 251, Compact FullRangeTM Gauge, Pfeiffer Vacuum).

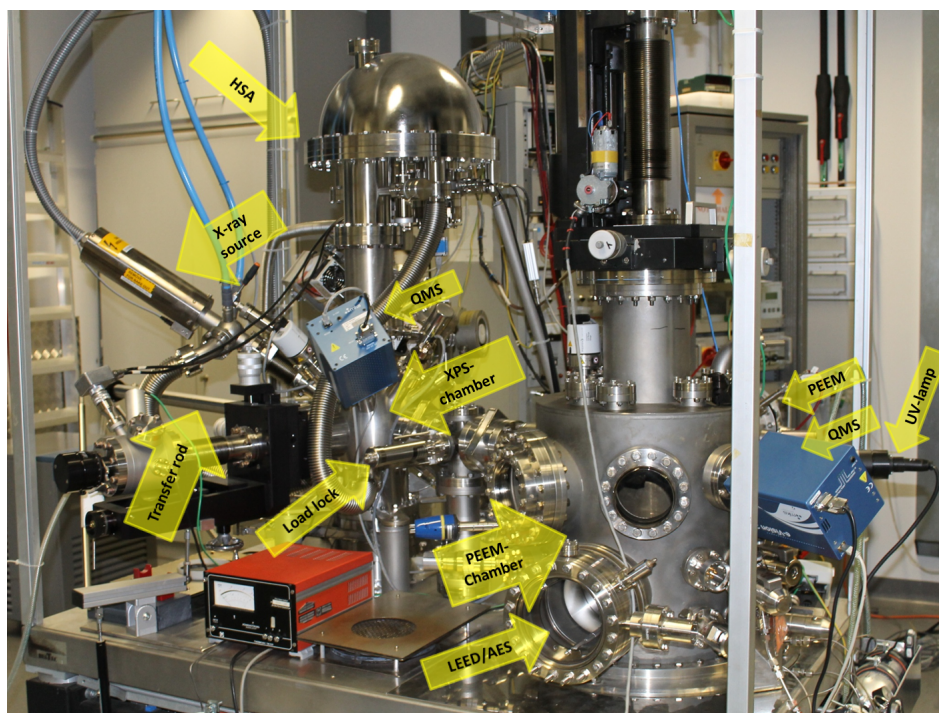
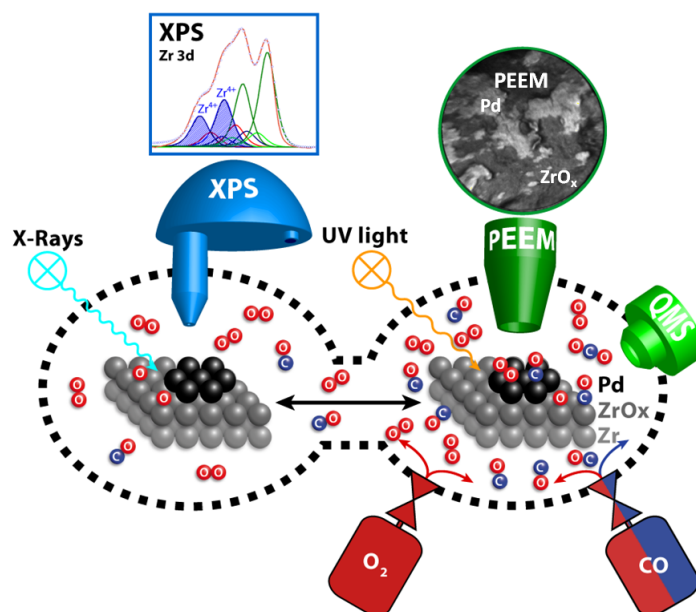


Figure 3.1: a) *UHV* experimental setup.



b) Schema of the *UHV* experimental setup. The sample is introduced into the system via load lock. The sample can be transferred by means of the transfer rod to the one of the chambers.

For monitoring the reactants and reaction products partial pressures during the experiments, a *QMS* (e-Vision⁺, MKS Instruments) was used. The chamber is additionally equipped with a *LEED/AES* (low-energy electron diffraction/auger electron spectroscopy SPECTALEED, Omicron NanoTechnology). The *Ar*⁺ sputtering of the

sample was performed with a sputter gun (IQE 11/35, SPECS). The sample is annealed up to 1273 K by means of the electron bombardment.

The second chamber of the experimental setup is equipped with a *HSA* (hemispherical electron energy analyzer, Phoibos 100, SPECS), a X-ray source (XR 50, SPECS) and a *QMS* (e-Vision⁺, MKS Instruments). In order to maintain a base pressure of 10^{-9} mbar, pumping of the chamber was performed by a *IGP* (StarCell 300, Varian) and a titanium sublimation pump. Additional pumping could be performed via load lock and via *PEEM* chamber. The pressure in the chamber was controlled by an ionization gauge (MVC-3, Vacum) and by the combined Pirani and cold cathode pressure gauge (PKR 251, Compact FullRangeTM Gauge, Pfeiffer Vacuum). For the cleaning of the sample, *Ar*⁺ sputtering and annealing facilities were also installed in this chamber. For performing the catalytic measurements, high purity gases (*CO* and *O*₂) were used, which were supplied via variable leak valves (Varian).

The samples, sample holder and manipulator

The samples and sample holder

The samples, which were used in present experiments, consisted of a 10x10 mm² polycrystalline *Rh* (MaTeck, purity 99.97%) and *Zr* (MaTeck, purity 99.98%) metal foils, and of the *Pd* powder supported by the *Zr* foil. In the case of the supported *Pd* samples, the *Pd* powder (MaTeck, purity 99.99%) was impregnated into the *Zr* foil (MaTeck, purity 99.98%) which served as a support.

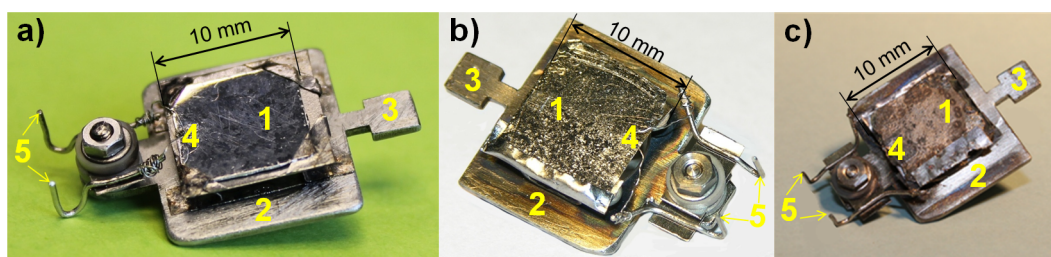


Figure 3.2: The samples used in the experiments: **a)** the polycrystalline Rh foil sample; **b)** the polycrystalline *Zr* foil sample; **c)** the sample consisting of the Pd powder, supported by *ZrO*₂ (1) fixed on the sample plate (2), which contains a transfer clutch (3) and a *Ni/NiCr* K-type thermocouple (4), which contacts with the sample holder contacts via the contact electrodes (5).

Each sample was fixed on a molybdenum standard sample plate (Omicron/SPECS) by means of spot-welding (Fig. 3.2). The sample plate could be fixed on the sample plate holder which, in turn, is fixed on the manipulator (Fig. 3.3 and Fig. 3.4). The construction of the sample holder allows transfer of the sample between the *PEEM* and the *XPS* chambers by means of a transfer rod*.

Sample manipulator in the PEEM chamber

The sample manipulator in the *PEEM* chamber (Fig. 3.3) allows positioning of the sample in different positions within the chamber, i.e. in the sputtering position, in the positions for performing of the *PEEM* or the *LEED/AES* measurements and in the transfer position.

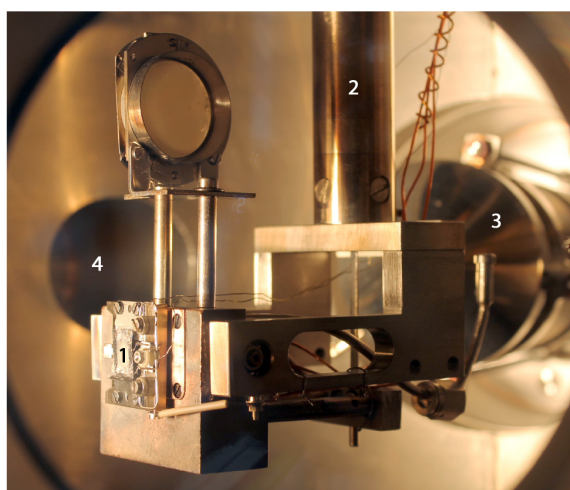


Figure 3.3: The view on the manipulator inside the *PEEM* chamber: (1) a sample mounted to a sample holder; (2) a manipulator; (3) the entrance lens of the *PEEM*; (4) entrance to the connection between the *PEEM* chamber and the load lock.

The sample manipulator allows to move a sample in two horizontal, x , y and in a vertical, z directions. Additionally, the rotation in a perpendicular to the z axis plane in a range of 0° to 360° and also a tilting of the sample in respect to the z axis is possible.

All these degrees of freedom in the positioning of the sample are necessary for the *PEEM* measurements, namely for the homogeneous illumination of a sample with

*see section 3.3 for details

UV light and for the adjustment of a *PEEM* image, i.e optimisation of the image brightness and sharpness by changing the position of a sample.

The sample is heated by means of electron bombardment. As the electron source, a home-made thoriated tungsten filament (thickness: $d=0.12$ mm) was used. Using a filament current of about 2 A and accelerating voltage of 400-500 V, an emission current of 25-28 mA and a temperature of the sample of about 1200 K can be achieved.

Sample manipulator in the XPS chamber

The sample manipulator in the *XPS* chamber (Fig. 3.4) is similar to that in the *PEEM* chamber. The manipulator allows positioning of the sample in the sputtering position, in the position for the *XPS* measurements and in the transfer position. Additionally, in order to perform the angle resolved *XPS* measurements, the angle between axis of the hemispherical analyser and the sample can be varied. As in the *PEEM* chamber, the sample in the *XPS* chamber was heated by means of the electron bombardment.

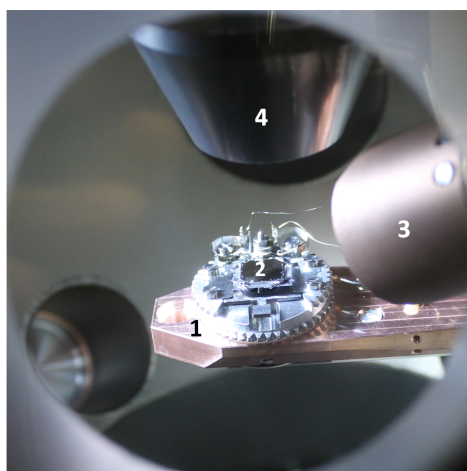


Figure 3.4: The view inside the *XPS* chamber: (1) sample manipulator; (2) sample; (3) X-ray source; (4) entrance of the hemispherical analyser.

The transfer system and the load lock

The *PEEM* chamber and the *XPS* chamber are connected by a load lock, which is shown in Fig. 3.5 a, b. The load lock is separated from the *PEEM* chamber and the *XPS* chamber by gate valves (VAT) and is pumped by a rotary vane pump (Duo 5, Pfeiffer Vacuum) and a turbomolecular pump (HiPace 80, Pfeiffer Vacuum). The pressure in the load lock is controlled by a hot cathode pressure gauge (MVC-3, Vacom).

The load lock is used for loading or unloading the sample into the *UHV* apparatus and for the sample transfer between the *PEEM* chamber and the *XPS* chamber without exposition of the sample to atmospheric pressure (Fig. 3.6).

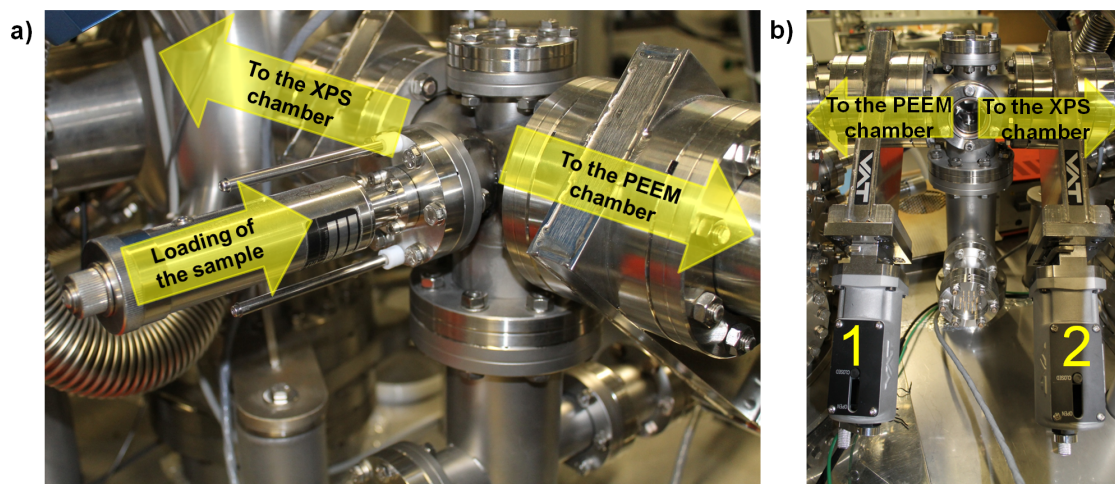


Figure 3.5: a) The front view of the load lock. Directions of loading of a sample into the load lock and of the transfer of a sample to the *PEEM* chamber and to the *XPS* chamber are marked; b) the back view of the load lock: (1) and (2) are the gate valves, separating the load lock from the *PEEM* chamber and the *XPS* chamber, respectively.

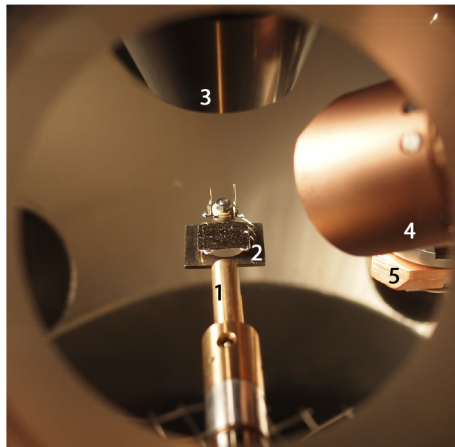


Figure 3.6: The view to the sample fixed on the transfer rod inside the *XPS* chamber: (1) transfer rod; (2) sample; (3) entrance of the hemispherical analyser; (4) X-ray source; (5) manipulator.

Preparation of sample surfaces

A proper preparation of the sample surface is crucial for catalytic studies, since the cleanness and the structure of the sample surface significantly affect its catalytic properties. For the studies intended in present thesis, the surface should contain, if at all, only minimal amounts of contaminations. The most common impurities on the sample surface were oxygen, carbon and sometimes also sulphur.

In present thesis, a standard *UHV* cleaning procedure was employed. This procedure consists of sputtering of a sample surface with Ar^+ ions, *UHV* annealing and heating in the, e.g. oxygen atmosphere to remove carbon. Depending on the particular sample, some steps can be skipped or performed in a different order.

- **Sputtering:** The surface contaminations can be removed (sputtered off) from the sample surface by the noble gas ions, e.g. Ar^+ . In this step, the Ar^+ ions are accelerated to relatively high kinetic energies (ca. 1-3 keV) and collide with the sample surface. These collisions lead to the removal of surface contaminations (Fig 3.7 a, b) [28]. The side effect of this method is the erosion of the surface and possible violation of arrangement of the surface atoms (Fig 3.7 c).

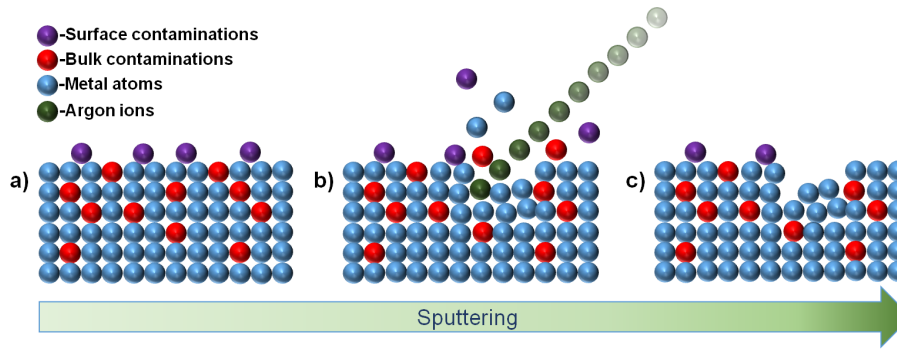


Figure 3.7: Schema of removing impurities from the sample surface by means of the Ar^+ ions sputtering: **a)** the sample surface before sputtering. The red atoms correspond to the impurities in the bulk and in the subsurface region and the violet atoms correspond to the impurities in the surface region. The blue atoms correspond to the clean metal; **b)** the Ar^+ sputtering process. Collision of the energetic ions with the surface atoms leads to the removal of the impurities from the surface and the subsurface region. Additionally, some metal atoms can also be removed; **c)** the final result of the Ar^+ sputtering process: some of the impurities have been removed from the surface and from the subsurface region, but the surface has become defected.

- Annealing of the sample in UHV:** This step of the cleaning procedure serves for the solution of the two problems. Foremost, the heating of the sample to high temperatures allows to restore the order of the surface atoms which was disturbed by sputtering (Fig 3.8 a, b). Additionally, heating of a sample to the high temperatures (about several hundreds K) leads to the desorption of volatile surface contaminations into the vacuum or to the dissolution of the surface contaminations into the bulk. As the result, only small amount of the contaminations remains on the surface. The side effect of the *UHV* annealing at high temperature is possible segregation of the impurities from the bulk, which can leads to contamination of the sample surface (Fig 3.8 c) [28].

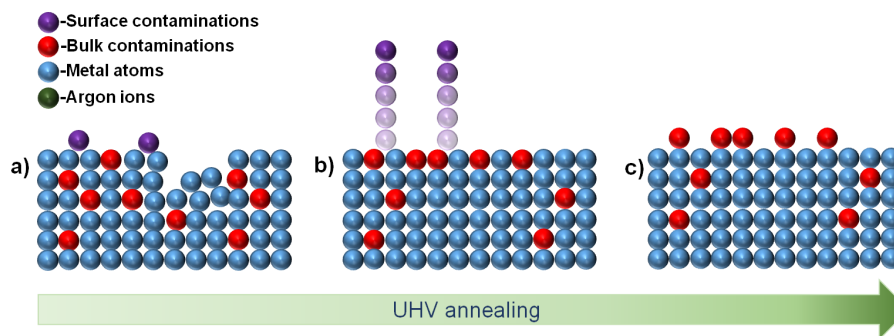


Figure 3.8: Annealing of the sample in *UHV* : **a)** defected sample surface with residual surface contaminations after the sputtering with Ar^+ ions; **b)** heating to high temperatures under *UHV* conditions leads to desorption of volatile contaminants as a desirable effect and the segregation as a side effect; **c)** the result of *UHV* annealing: restoring of the surface atomic order, and enrichment of the surface by impurities from the bulk.

- Heating in the reactive gas atmosphere:** This step removes the contaminations (usually, carbon) from the sample surface by formation of the volatile compounds as a result of the chemical reaction between the reactive gases and the surface impurities (Fig 3.9 a, b, c) [28]. The most frequently used reactive gases are oxygen or hydrogen. The side effect of this method is possible formation of oxides or hydrides on the surface which should be removed by sputtering or *UHV* annealing.

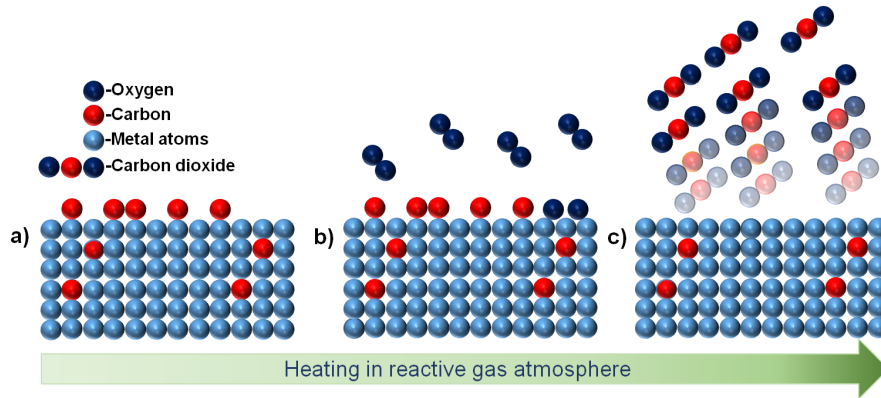


Figure 3.9: Heating of the sample in reactive gas atmosphere: **a)** the sample surface with carbon contaminants; **b)** exposure of the sample surface in the oxygen atmosphere at high temperature; **c)** oxygen adsorbs dissociatively on the sample surface. Surface reaction between atomic oxygen and surface carbon leads to the formation of CO_2 which desorbs from the surface, leaving it almost clean.

Since no universal cleaning procedure exists, each particular sample needs special cleaning procedure which fits to the current purpose. In the present thesis, each investigated sample was cleaned with alternating amount of cleaning cycles containing the steps which were mentioned above.

4 | *Methods*

Photoemission electron microscopy

The photoemission electron microscope (*PEEM*) is a microscope which images the surface by photoelectrons which are generated by illumination of a sample by high energy photons, e.g. by *UV*-light or by X-rays [147].

The first demonstration of the possibility of imaging of the surface with the *UV* photoelectrons was performed by Brüche in the 1930's [148]. The most successful period of the *PEEM* started however in the 1980's, when researchers used this technique for investigation of spatio-temporal behaviour of different catalytic reactions, e.g. *CO* oxidation reaction on transition metal surfaces.

Nowadays, the *PEEM* is a powerful tool for *in situ* imaging of ongoing physical and chemical processes, such as surface chemical reactions [45], including spatio-temporal oscillations [24], thermal stability of oxides [149], surface diffusion [113], etc.

Principle of PEEM operation

The working principle of the *PEEM* is based on the *photoelectric effect*. The phenomenon of photoelectric effect was detected by Henrich Hertz and Wilhelm Hallwachs in 1887 [150, 151]. In 1905, Albert Einstein gave the first theoretical explanation of this phenomenon. For this work he received a Nobel prize in 1921 [152]. According to Einstein, the relation between the energy of the incident photons and the kinetic energy of the emitted photoelectrons is described by following equation (eq. 4.1):

$$E_{kin} = h\nu - E_B - \Phi \quad (4.1)$$

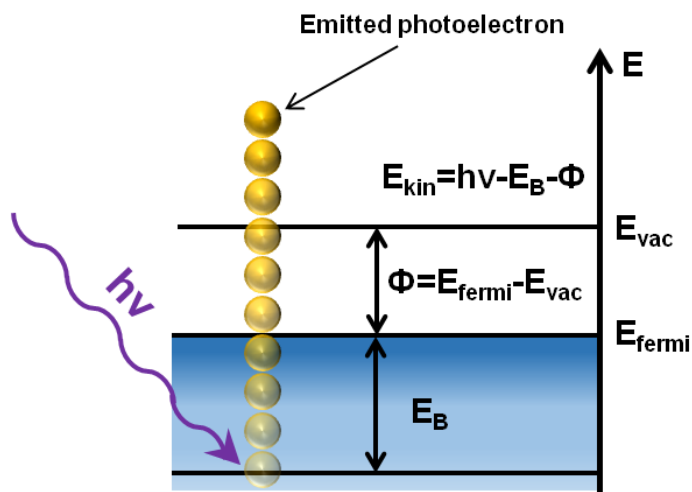


Figure 4.1: Schema of the photoelectric effect. The kinetic energy of photoemitted electron (E_k) depends on the energy of incoming photon ($h\nu$), the binding energy of the electron in the atom (E_B) and value of the sample work function (Φ).

During photoemission, a particular electron absorbs a photon of a certain energy and, if the energy of the incident photon is higher than the binding energy of that particular electron in the solid and the sample work function, photoemission takes place (Fig. 4.1). Figure 4.2 illustrates the usual photoemission spectrum which consists of following regions: secondary electrons, Auger electrons, core level electrons and valence electrons.

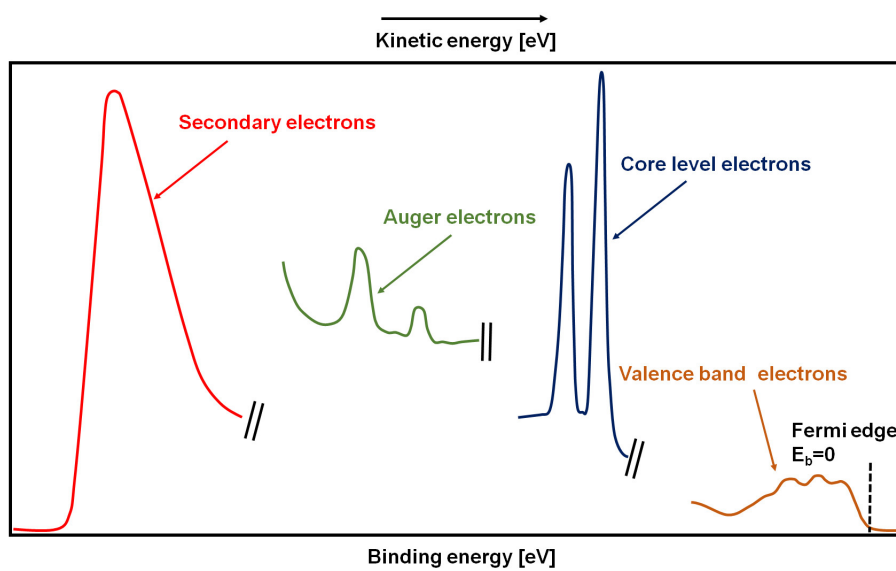


Figure 4.2: Schema of the photoemission spectrum.

The electrons in the valence band have relatively low binding energy and these electrons are very sensitive to the chemical environment, e.g. adsorbed molecules. For obtaining information about the electron states in the valence band, *UV*-photoelectron

spectroscopy (*UPS*) is used.

Core levels are associated with the electronic states which are localized on a single atom and therefore these states characterize the chemical identity of the atomic species. They are used for producing chemical contrast in *X-ray PEEM* and for chemical analysis in *XPS*. The photoemission spectrum in the Figure 4.2 also contains the *Auger electrons*. These electrons are emitted from the solid due to relaxation of the ions, which were created in the photoemission process. The emission of photoelectrons from the atoms in the solid creates the core holes which can be filled by the electrons which reside on higher energy levels. Upon filling of the core hole, i.e. upon transition from higher energy level to lower energy level, these electrons transfer their energy to the Auger electrons which are emitted from the solid. Kinetic energy of the Auger electron may be defined as energy difference between the energy level of the core hole, the energy level of electron which fill the core hole and the energy level where Auger electron resided before emission [136].

On the left of the photoemission spectrum in Fig. 4.2, the secondary electrons attributed to inelastically scattered electrons can be found. These electrons are used for imaging in *UV-PEEM*. The light sources which are used for excitation of the photoelectrons in laboratory-based *PEEM* are usually mercury lamps (cut off energy 4.9 eV) or deuterium lamps (cut off energy 6.8 eV). Since cut off energy of these sources is small, illumination of the solid surface with these light sources leads to emission of small fractions of photoelectrons from valence band and huge fractions of secondary (inelastically scattered) electrons, which appear in a range between the excitation energy $h\nu$ and the sample work function (Φ). The amount of emitted secondary electrons, which is dependent on the sample work function, determines the *PEEM* image contrast*.

As a full field microscope, which means that the entire region within the field of view of the microscope is imaged to a phosphor screen at the same time, the *PEEM* has following advantages: the whole region of interest within the field of view of the *PEEM* is imaged at the same time and ability to perform the real-time imaging. Both these features allow *in situ* observations of different ongoing physical and chemical processes. Lateral resolution of the used *PEEM* (about 1 μm) is limited by the chromatic aber-

*the details of *PEEM* image contrast are discussed in a section 4.1.2.

rations of the objective lenses. *PEEM* is a surface sensitive technique because the secondary (inelastically scattered) electrons, which are used for imaging in *PEEM* emerged from a very narrow region (about few topmost atomic layers) of the sample.

Origin of the PEEM image contrast

The image contrast in the *PEEM* is strongly affected by the local work function of the sample surface. The value of the local work function depends on different factors, i.e. crystallographic orientation of the imaged surface, the topography of the imaged surface, presence of the adsorbed molecules, etc. [22]. Change of the surface work function leads to change of yield of the photoelectrons (*photocurrent density*) which changes the local *PEEM* image intensity. The relationship between j which is photocurrent density, the energy of the incident photons $h\nu$ and the sample work function Φ can be approximately expressed using the Fowler theory [153]:

$$j \sim (h\nu - \Phi)^2 \quad (4.2)$$

The principle of the *PEEM* contrast is illustrated in Fig. 4.3. If a sample with a work function Φ is illuminated with photons with the kinetic energy $h\nu$, the resulting photoemission spectrum has the width $(h\nu - \Phi)$.

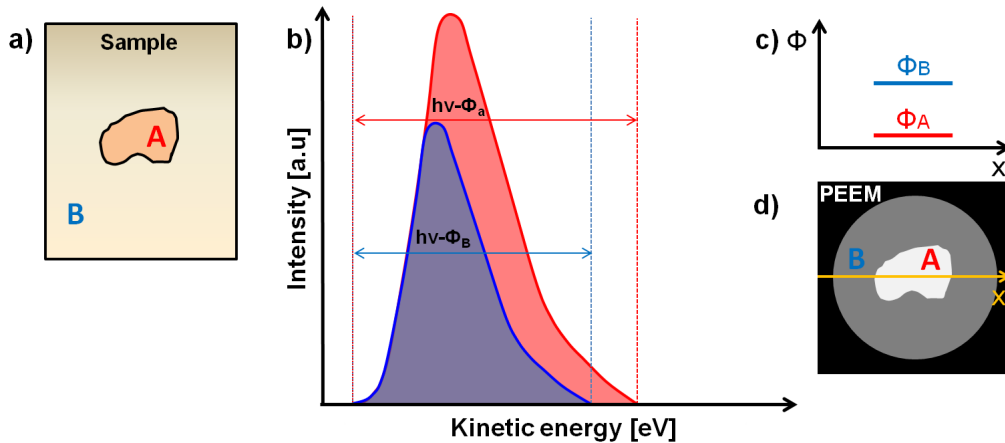


Figure 4.3: Formation of the image contrast in a *PEEM*: **a)** the sample which consists of two regions of different work function; **b)** schematic comparison of the photoemission spectra of the two different regions of the investigated sample; **c)** the work functions of two regions of the sample; **d)** the *PEEM* image of the sample shown in **(a)**. The brightness of two different regions on the *PEEM* image.

The difference in the work function for different sample regions leads to the different width of the spectra and subsequently, to the different yield of photoemitted electrons (*photocurrent density*). This leads to the different brightness of these two regions on the *PEEM* screen. The relation between the sample work function on the local *PEEM* image brightness can be expressed as follows:

low work function \implies *high photocurrent density* \implies *bright PEEM image*
high work function \implies *low photocurrent density* \implies *dark PEEM image*

Design of the PEEM apparatus

In the present thesis the *PEEM-150* (STAIB instruments) was used, whose construction is presented schematically in Fig. 4.4 a, b. The microscope consists of: an excitation source, a lens system, an electron amplifier (the microchannel plate), a phosphor screen.

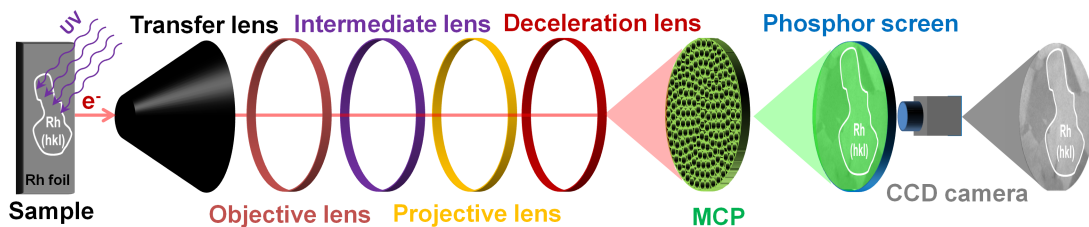


Figure 4.4: Schema of the UV-*PEEM*. Illumination of the sample with *UV*-light leads to the emission of photoelectrons. The photoemitted electrons are focused by a system of electrostatic lenses on the microchannel plate where number of electrons is amplified. Finally, the electrons are projected onto the phosphor screen and the image from the screen is recorded by a *CCD* camera.

As the *excitation source*, a water cooled *UV*-lamp (D200, Heraeus, Germany) with cut off photon energy of 6.8 eV is used. This value of cut off energy allows the imaging of the surfaces of noble metals. Between the sample and the *UV*-lamp a system of two condenser lenses is placed. They allow focusing of the *UV*-beam on the sample to a spot of several millimetres in diameter.

The electrostatic *lens system* of the microscope consists of a transfer lens, an objective lens, an intermediate lens, a projective lens and a deceleration lens (Fig. 4.4 a).

The *transfer lens* (or *anode*) serves for the acceleration of the photoelectrons which are emitted from the sample (or *cathode*). The anode voltage applied between the sample and the transfer lens is $U_a=15$ keV. The *objective lens* forms the first real image of the sample and is used for focusing the electron beam. The potential applied to this lens lies in the range of $U_{obj}=2-4$ keV. Next, the *intermediate lens*, magnifies the sample real image. During the experiments which are presented in the present thesis, the potential applied to the intermediate lens was constant and equal to $U_{int}=10$ keV. The *projective lens* and the *deceleration lens* have an applied potential of 1.58 keV and 1.25 keV respectively, serving for decreasing of the kinetic energy of the beam of photoemitted electrons. This deceleration is necessary because the *microchannel plate* (*MCP*), which serves as the *electron amplifier* has a maximum sensitivity in the range of 0.2-2 keV. The *MCP* amplifies the electron signal by multiplication of the electrons via generation of secondary electrons. The *MCP* consists of array of separated channels which act as an array channeltrons. After leaving the *MCP*, the amplified electron beam is again accelerated with a potential of 3 keV and is projected onto the *phosphor screen*, which converts electron impact into the light. The image which is created by the phosphor screen is recorded by a *CCD camera* (Hamamatsu Orca flash), which is mounted outside the vacuum system. Using of the CCD camera allows the achievement of the temporal resolution in the μs range. The *PEEM-150* allows a lateral resolution of about $1 \mu m$ and images a field of view of about $500 \mu m$. The distance between the sample and the the entrance cone could be varied in order to adjust the image sharpness.

X-ray photoelectron spectroscopy

The first *XPS* setup was developed by Kai Siegbach in Uppsala University in 1954. For this achievement, Kai Siegbach was awarded the Nobel prize in physics in 1981 "for his contribution to the development of high-resolution electron spectroscopy" [154]. Nowadays, the *XPS* is one of the most frequently used techniques in surface science.

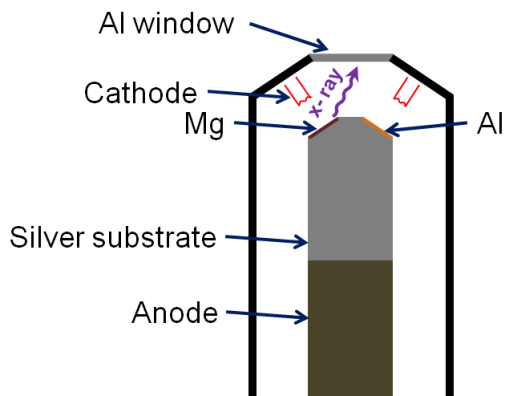


Figure 4.5: Twin anode X-ray source. Characteristic X-ray radiation ($AlK\alpha$ or $MgK\alpha$) is emitted from the anode (Al or Mg) upon the bombardment with the high energy electrons.

The high surface and elemental sensitivity of the *XPS* provides the possibility to monitor even small changes of the composition of the surface and thus to elucidate the processes which occur on the surface.

Instrumentation

The *XPS* apparatus used in the present thesis consists of two main components: the X-ray source and the hemispherical analyser. As a *X-ray source* for *XPS* measurements, a twin anode X-ray source was used (Fig 4.5). In this source, the X-ray photons are generated by bombarding the anode with high energy electrons, which are emitted from the electrically heated cathode. The material of the anode determines the energy of the emitted X-ray radiation. In the X-ray source used in the present thesis *Al* and *Mg* anodes were used. Upon bombardment with high energy electrons, *Al* and *Mg* anodes emit $AlK\alpha$ (1486.6 eV) and $MgK\alpha$ (1253.6 eV) X-rays, respectively. Since by changing of the kinetic energy of incoming X-ray photons Auger peaks are shifted, but photoelectron peaks stay on the same positions, the use of the twin anode X-ray source makes possible to differentiate between overlapping Auger and photoelectron peaks [136].

The *hemispherical analyser (HSA)* is presented in Fig. 4.6. The *HSA* consists of two stainless steel hemispheres which are positioned concentrically. The inner sphere has the radius R_1 and the outer sphere the radius R_2 , respectively. The hemispheres are separated by a gap.

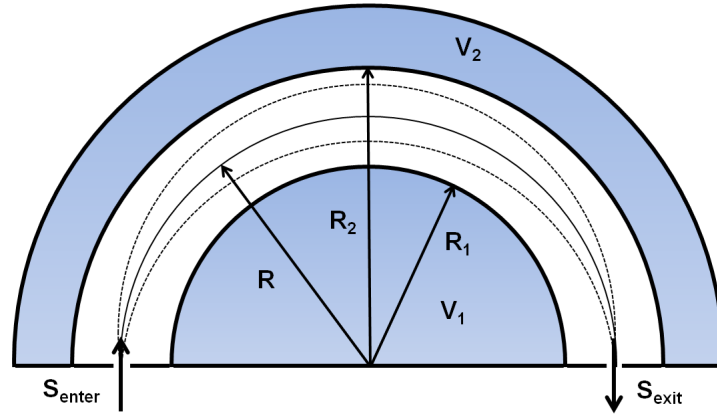


Figure 4.6: Schema of a hemispherical analyser.

Through this gap, the electrons can reach the detector. Potentials which are applied to the inner and outer hemispheres are V_1 and V_2 respectively. The potential, which is applied to the outer sphere is more negative than the potential which is applied to the inner one. After passing the lens system, the electrons enter the analyser through the slit (S_{enter}). If the kinetic energy of the incoming electrons is equal to the pass energy (E_{pass}) which is set by the analyser, the electrons will follow the trajectory with radius R and subsequently will enter the exit slit (S_{exit}) and will reach the detector. These electrons will contribute to the *XPS* spectrum. The passing energy E_{pass} is determined by following equation [135]:

$$E_{pass} = e \cdot \Delta V \cdot \left(\frac{R_1 \cdot R_2}{R_2^2 - R_1^2} \right) \quad (4.3)$$

In contrary, the electrons which enter the slit (S_{enter}) with kinetic energy which differs from the E_{pass} , will not reach the detector and will not contribute to the *XPS* spectrum. By changing of the potentials V_1 and V_2 , one achieves that the electrons of desired kinetic energy reach the detector and contribute to the *XPS* spectrum.

Interpretation of XPS spectra

For the excitation of photoelectrons, *XPS* uses X-rays, e.g. $\text{AlK}\alpha$ 1486.6 eV and $\text{MgK}\alpha$ 1253.6 eV whose energy is sufficient to excite electrons from core levels of atoms. Since the core levels are unique for particular elements, the *XPS* provides straightforward information about chemical composition of the investigated sample.

After excitation by X-ray photons with kinetic energy $h\nu$, the photoelectrons travel towards the sample surface. After leaving the sample surface, the photoelectrons have to pass the lens system and enter the *HSA*. Since the Fermi levels of the analyser and the sample are different, the kinetic energy of the photoelectrons are measured in respect to the Fermi level of the analyser (Fig 4.7).

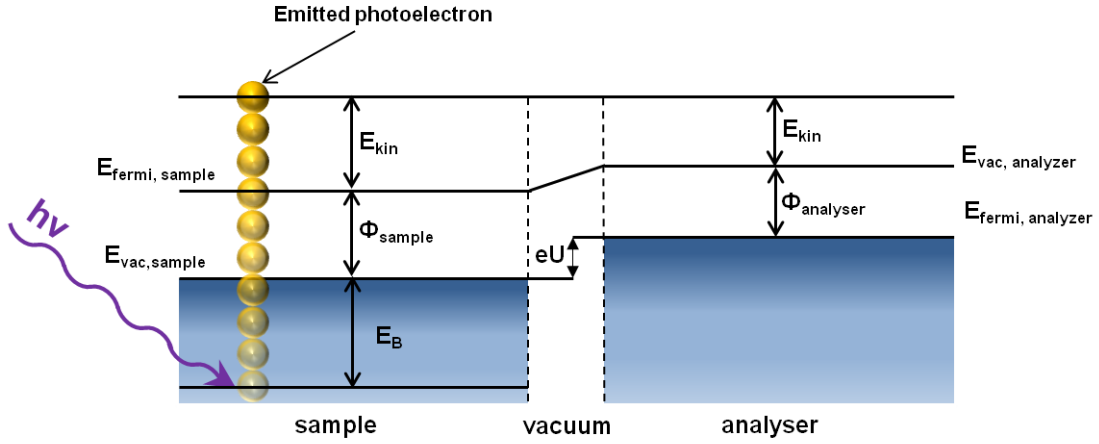


Figure 4.7: Schematic representation of the measurement of the photoelectron kinetic energy in *XPS*. The kinetic energy of the electron, photoemitted from the sample is measured in respect to the Fermi level of the analyser.

The kinetic energy (E_{kin}) of the emitted photoelectrons can be determined from eq. 4.6:

$$E_{kin} = h\nu - E_B - \Phi_s - (\Phi_a - \Phi_s) = h\nu - E_B - \Phi_a \quad (4.4)$$

In Figure 4.8 a, a typical photoemission survey spectrum of metallic *Zr* polycrystalline sample and in Fig. 4.8 b high resolution spectrum of the *Zr* 3d region for the same sample are presented. The spectra exhibit several well distinguishable 3s, 3p, 3d, 4s and 4p peaks of *Zr* (Fig. 4.8 b). The high resolution spectrum of *Zr* 3d region exhibits two $3d_{\frac{1}{2}}$ and $3d_{\frac{3}{2}}$ peaks (Fig. 4.8 c). Such a splitting is typical for the p, d and f atomic orbitals, i.e for atomic orbitals with angular momentum quantum number l which is higher than 0. The reason of such splitting is the *spin-orbit interaction (coupling)* which means that the total angular momentum of the electron is a sum of angular momentum quantum number l and the spin s i.e:

$$j = l + s \quad (4.5)$$

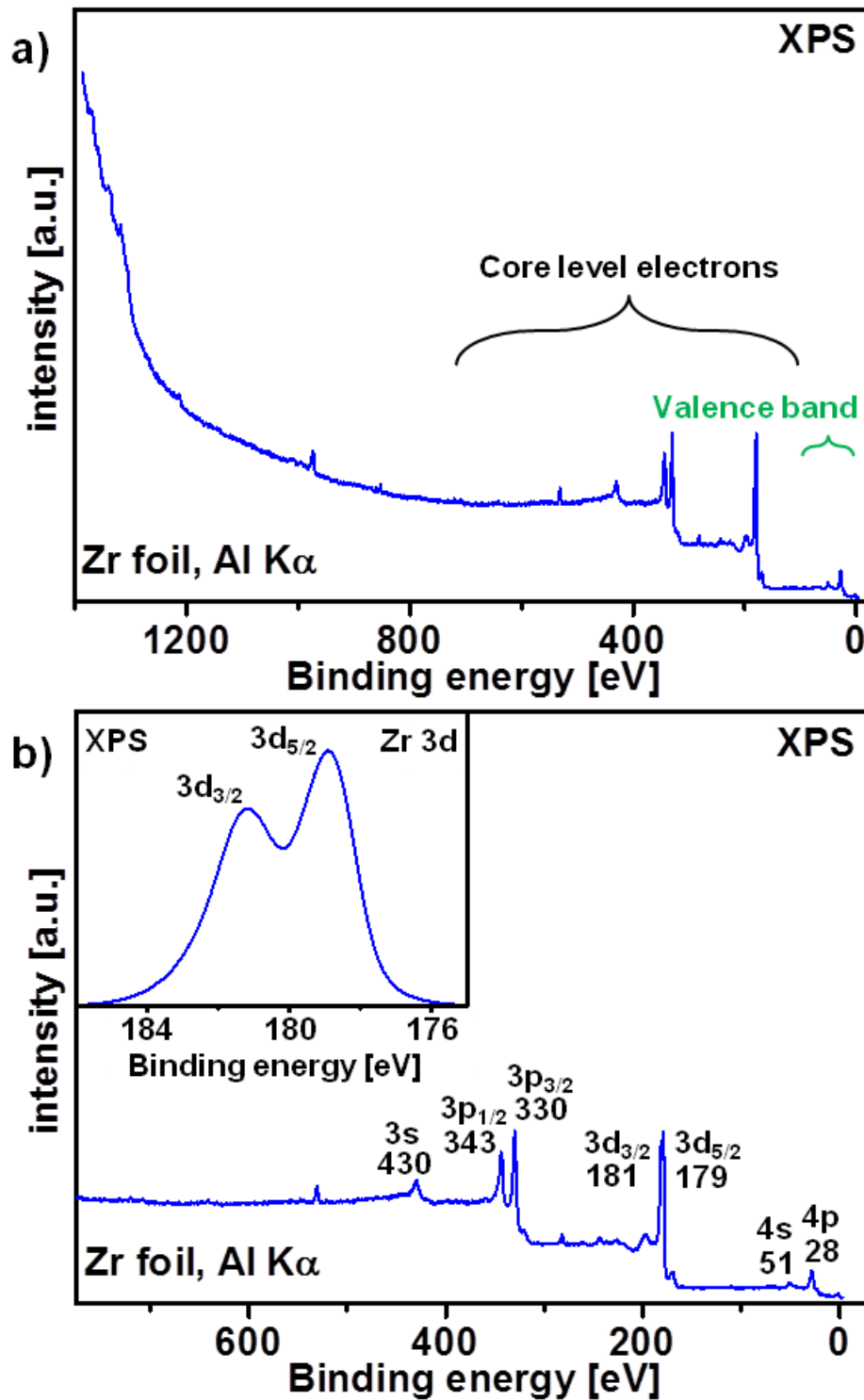


Figure 4.8: The X-ray photoelectron spectra of a *Zr* polycrystalline foil obtained using $AlK\alpha$ radiation: a) *Zr* survey photoelectron spectrum: the region of the core levels, the valence band and the Fermi edge are marked; b) a selected part of the *Zr* survey spectrum which shows the main photoemission peaks of *Zr* (i.e. 3s, 3p, 3d, 4s and 4p) and corresponding binding energies for these peaks. The *Zr* 3d region, consisting of the two $3d_{3/2}$ and $3d_{5/2}$ peaks which are separated by 2.4 eV is shown in the inset.

Since the spin of the electron can vary between $-\frac{1}{2}$ and $\frac{1}{2}$, the d - atomic orbital total angular momentum can be either $\frac{3}{2}$, either $\frac{5}{2}$. The area ratio for these peaks is related to degeneracy of each spin state, e.g. for 3d, where the principal quantum number n is 3 and l is 2 the area ratio between peaks is 2:3.

Usually, a *XPS* spectrum contains also the *X-ray satellites*, which are common for the non-monochromatic X-ray sources. These peaks occur at lower binding energies than the photoelectron peaks. The reason for these peaks is that the non-monochromatic X-ray radiation consists of not only photons with characteristic energy, but also photons with higher energy [155]. Besides the *X-ray satellites*, the *XPS* spectrum can show the *X-ray ghost lines*. These lines occur due to the impurities in the anode material. The *shake-up lines* may appear in the *XPS* spectrum when photoelectron is emitted from an atom in the excited state (in opposite to normal photoemission from atom in ground state). In this case, a part of the energy of the photoelectron is transferred to another electron and subsequently the energy of the photoelectron is reduced. Such lines are shifted in the direction of higher binding energy in comparison with photoelectron peaks.

For proper quantification of *XPS* peaks, the background signal has to be subtracted by using different subtraction algorithms. In the present thesis for subtracting the background signal from *XPS* spectra, the Shirley algorithm was used [156].

Estimation of the thickness of surface layers

Besides obtaining information about the composition of the sample, the photoemission spectrum provides information about the concentration of the certain element in the surface region of the investigated sample. Also, by proper quantification of *XPS* high resolution spectra, information about the thickness of the overlayers which contribute to the sample can be obtained [155].

The intensity of the photoemission peak of element A is related to the concentration of this element in the sample through following equation:

$$I_A = \sigma \cdot n_A \cdot \lambda \cdot k \quad (4.6)$$

σ -photoionization cross section for certain atomic orbital, n_a -number of atoms of the element per cm^3 [$\frac{atoms}{cm^3}$], λ -inelastic mean free path (IMFP) [nm] which determines the distance which electron can travel in the solid before it will be inelastically scattered and loses his energy, k -instrumental parameter which includes the x-ray photon flux transmission, the transmission function of the analyser and the probability of detection of the photoelectrons with kinetic energy E_{kin} by the analyser.

From the eq. 4.7, n_a can be derived as:

$$n_A = \frac{I_A}{S}, \quad S = \sigma \cdot \lambda \cdot k \quad (4.7)$$

Where S is a sensitivity factor, which determines the fact that the probability of the photoemission of the photoelectrons electrons from the different atomic orbitals is different. Using eq. 4.9, the concentration of an element in the sample can be determined as follows:

$$c_A = \frac{n_A}{\sum n_i} \cdot 100\% \quad (4.8)$$

The surface sensitivity of *XPS* is based on that fact that electrons of the certain kinetic energy may only travel the certain distance in the solid or in other words, the electrons of different kinetic energy have different inelastic mean free path in the solid. After passing the distance equal to the inelastic mean free path in the solid, the electron might be inelastically scattered and thus cannot contribute to the *XPS* spectrum. Within the energy ranges which are used in the laboratory-based *XPS* (100-1400 eV), the electrons interact strongly with atoms of the solid sample and the inelastic mean free path of electrons is therefore only several monolayers long. Hence, all the information about composition of the sample obtained from the analysis of the *XPS* spectrum is related to the surface layers of the sample [155].

The inelastic mean free path (IMFP) λ is one of the most important parameters in quantitative analysis of *XPS*. As was mentioned before, λ is energy dependent. The relation between the kinetic energy of the electron E_{kin} travelling inside solid and inelastic mean free path λ is given by the *universal curve* (Fig. 4.9). Exact knowledge about λ for the certain photoemission peak gives the opportunity to determine the thickness of the overlayers which contribute to the sample.

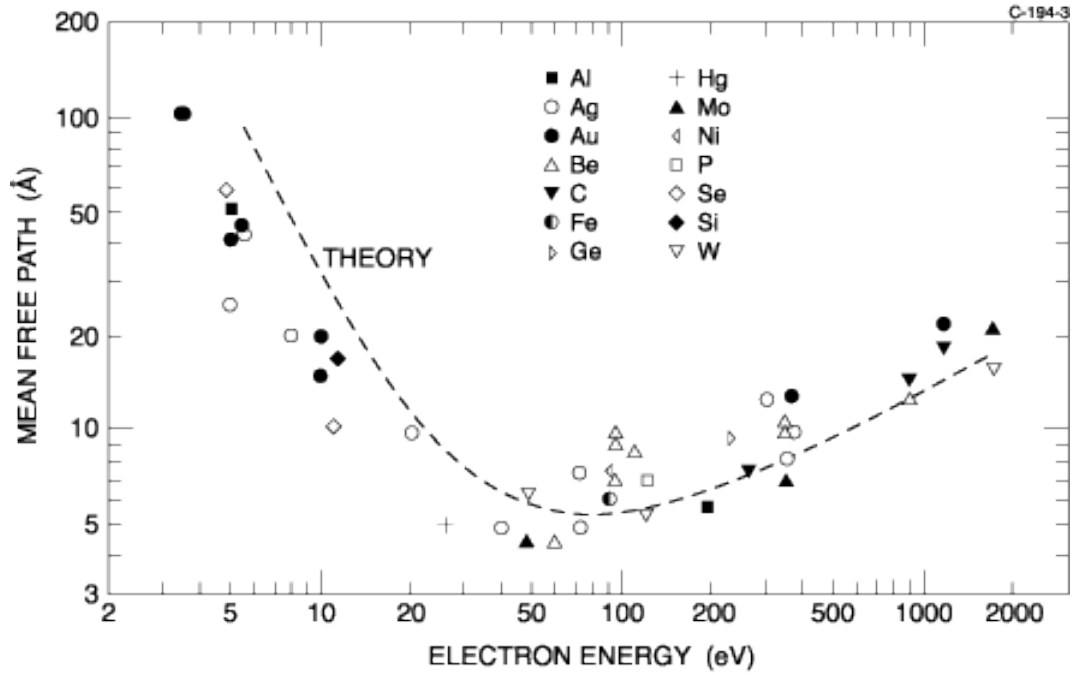


Figure 4.9: Universal IMFP curve. The graph is adapted from the ref. [157].

The determination of the thickness of the overlayer structures is based on the assumption that photoelectron intensity is attenuated exponentially with increase of the overlayer thickness. The relation between photoelectron intensity and thickness of the overlayer is determined by eq. 4.10:

$$I_x = k \cdot \sigma_x \cdot \lambda_x \int_0^d C_x^M \cdot \exp\left(\frac{-z}{\lambda_x \cdot \cos\theta}\right) dz \quad (4.9)$$

Here, λ_x , [nm]-is the mean free path of the electrons emitted from the element x, which are escaping the solid with E_{kin} , I_x -intensity of photoelectron signal from element x, C_x^M -molar density an the element x [mol/dm³] z -coordinate, d -is a thickness of the overlayer, [nm], θ -collection angle which is the angle of between surface and the analyser (Fig 4.10).

Eq. 4.10 allows the determination of the thickness of the different overlayers, contributing to the different multi-layered systems, e.g. metal-oxide structures, different multi-layered materials, deposited on the substrate, etc.

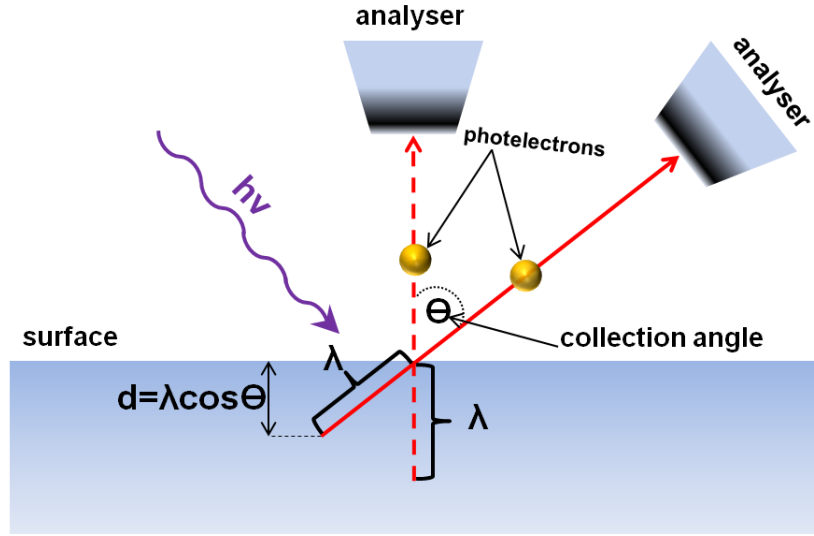


Figure 4.10: Illustration of collection of the photoelectrons under the different collection angle Θ . Changing of the collection angle changes the surface sensitivity of the XPS.

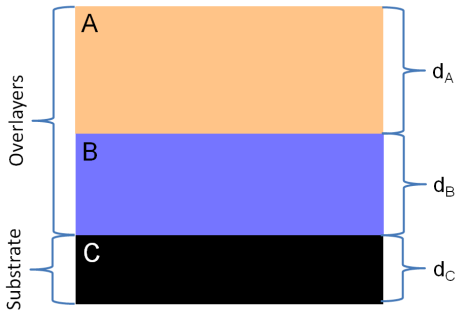


Figure 4.11: Schema of the multi-layer system, consisting of two overlayers and a substrate.

For the case of multi-layered system, consisting of two overlayers on the substrate (Fig. 4.11), eq. 4.12 can be transformed into the following set of equations [69]:

$$I_A = k \cdot \sigma_A \cdot \lambda_A(E_{kin}) \cdot C_A^M \cdot (1 - \exp(\frac{-d_A}{\lambda_A(E_{kin}) \cdot \cos\theta})) \quad (4.10)$$

$$I_B = k \cdot \sigma_B \cdot \lambda_B(E_{kin}) \cdot C_B^M \cdot (1 - \exp(\frac{-d_B}{\lambda_B(E_{kin}) \cdot \cos\theta})) \cdot (\exp(\frac{-d_A}{\lambda_A(E_{kin}) \cdot \cos\theta})) \quad (4.11)$$

$$I_C = k \cdot \sigma_C \cdot \lambda_C(E_{kin}) \cdot C_C^M \cdot (\exp(\frac{-d_B}{\lambda_B(E_{kin}) \cdot \cos\theta})) \cdot (\exp(\frac{-d_A}{\lambda_A(E_{kin}) \cdot \cos\theta})) \quad (4.12)$$

Eq. 4.11-4.13 are derived in assumption that all overlayer structures and a substrate are flat and their composition is homogeneous. The effect of the surface structure on the signal of the photoemitted electron and the inhomogeneities in the composition of

the overlayers and the substrate is not considered here. Using eq. 4.11-4.13, from the intensity ratio one can calculate the thickness of the layers A and B.

Quadrupole mass spectrometry (QMS)

Principle of QMS operation

Nowadays, the *quadrupole mass spectrometry* (*QMS*) is a commonly used method for registration of the products of chemical processes which take place in the gas phase. The *QMS* also found a wide application for the determination of the partial pressures of gaseous reactants.

In the present thesis, the *QMS* was used for the monitoring of the partial pressures of reactive gases (*CO* and *O₂*) and for the monitoring of *CO₂* production during the ongoing catalytic reaction. Additionally, the *QMS* served for monitoring of the helium partial pressure during a leak check.

The principle of the *QMS* operation is based on measurement of *mass-to-charge ratio* (m/z) of charged particles. Neutral molecules enter the *QMS* and become ionized by the electron impact. Resulting ions are accelerated towards the mass filter where the ions are separated in respect to their *mass-to-charge ratio* (m/z). Ions with the desirable m/z will enter the detector and subsequently contribute to the mass spectrum. The rest of the ions are neutralized and will leave the mass filter without detection. The typical mass spectrum (Fig. 4.12) consists of a set of narrow lines. Each line corresponds to the certain chemical compound. Height of the each certain line is proportional to amount of this compound in the gas phase.

Instrumentation

The *QMS* consists of an ionizer, a quadrupole mass analyser and an ion detector. Principal schema of a typical *QMS* is presented in the Fig. 4.13. Prior to the mass spectrometric analysis, the gaseous compounds should be ionized in the *ionizer* using an appropriate method. Most frequently, as a method of ion production in the gas phase, electron impact ionization is used. In general, the electron impact ionization process is described by eq. 4.16:

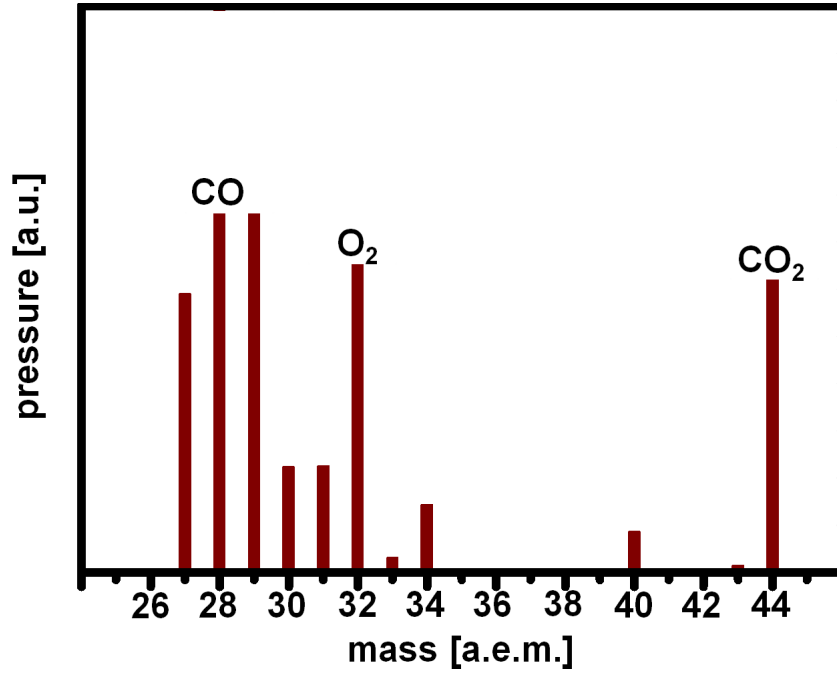


Figure 4.12: Mass spectrum recorded during ongoing CO oxidation on transition metal surfaces.



Here, A -analysed gas phase molecule, e^{-} -electron, A^{+} -positive ion, which is formed during the electron impact ionization. The electrons from the thermoemission source are accelerated and collide with gaseous molecules with subsequent production of positive ions (Fig. 4.13).

The resulting ion beam passes the *focusing lenses* where the ions are focused and equilibrated in their speeds in order to provide better mass selection.

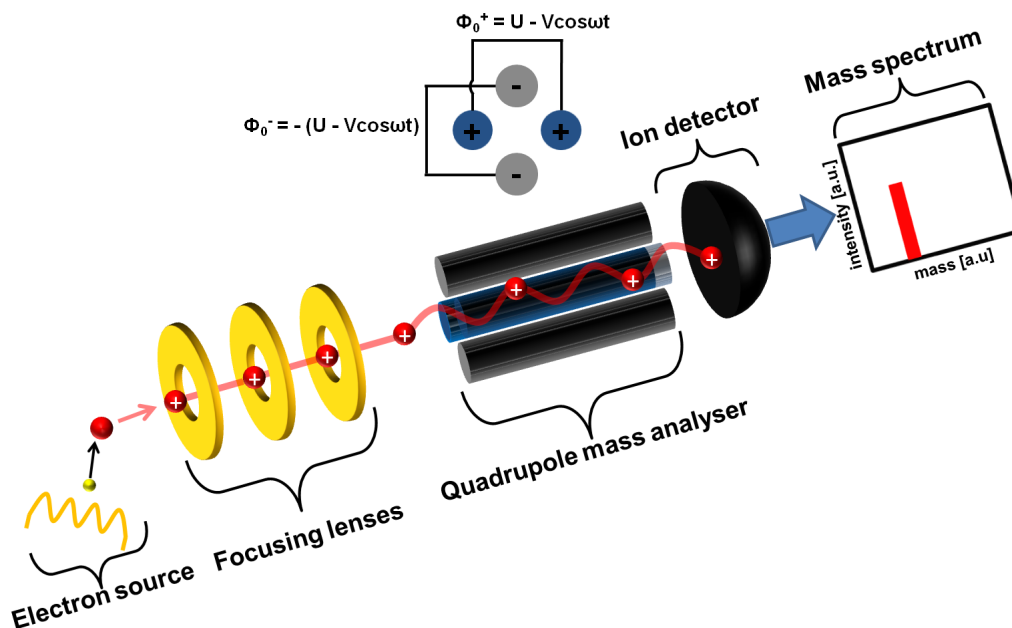


Figure 4.13: Schema of a quadrupole mass spectrometer. Molecules from the gas phase are ionized by means of electron impact. After passing the focusing lenses, the ions reach the quadrupole mass analyser where they are selected in respect to the m/z ratio. Only ions with desired m/z ratio can enter the detector and contribute to the mass spectrum.

Afterwards, the ion beam enters the *Quadrupole mass analyser*. This analyser consists of four cylindrical parallel rods. Opposing rods are electrically connected with each other. Between opposing rods positive and negative potentials Φ_0 are applied. These potentials affect the motion of the ions inside the mass analyser. The potential Φ_0 for opposing rods is described by eq. 4.17:

$$\Phi_0^+ = +(U - V \cos \omega t) \quad \Phi_0^- = -(U - V \cos \omega t) \quad (4.14)$$

Here, Φ_0 -applied potential, U -DC voltage, $V \cos \omega t$ -AC voltage, V -peak voltage of AC voltage, ω -angular frequency.

The potential Φ_0 which is applied to the rods in the quadrupole mass analyser affects the trajectory of the incoming ions. At a certain value of Φ_0 , only ions with certain m/z ratio can pass through the quadrupole mass analyser and reach the detector. By tuning of the Φ_0 value, it can be scanned through all desired m/z ratios.

Usually, as a ion detector in a *QMS*, either a Faraday cup or a channeltron are used. The Faraday cup is a cup which measures electron current originating from hitting the ions with the metal which causes the neutralization of the ions. In the case of

the low gas pressures (i.e. small ion currents) detection of the ions can be performed by the channeltron. The channeltron acts as an amplifier of the signal from incoming ions. The amplification occurs via emission of secondary electrons due to collision of the incoming ions with the walls of the channeltron.

Electron backscatter diffraction

Electron backscatter diffraction (EBSD) is a method which provides quantitative crystallographic characterisation of solid crystalline surfaces. *EBSD* may provide useful information about crystallographic orientation of μm - sized grains of polycrystalline materials. Additionally, this method reveals the size of the grains of polycrystalline materials, grain boundaries, different phases and misorientation of the grains [157].

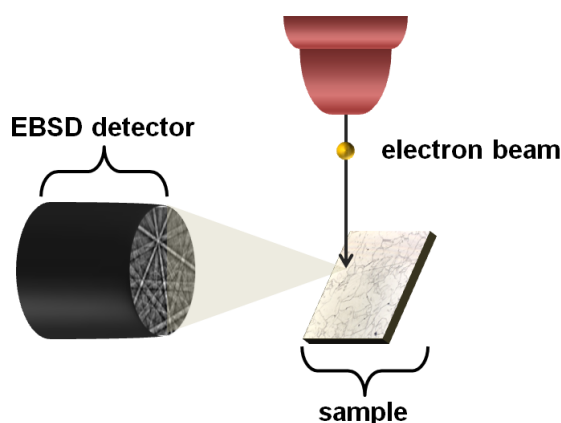


Figure 4.14: Schema of the *EBSD* experiment. The electron beam from the *SEM* is focused on the polycrystalline sample. Some of the electrons which have reached the sample become backscattered and diffract with formation of Kikuschi bands on the phosphor screen. Analysis of the image gives information about crystallographic orientation of the certain region of the sample.

EBSD experiments are usually performed in a scanning electron microscope (*SEM*) with an attached *EBSD* detector. Spatial resolution in the *EBSD* is limited by spatial resolution of the *SEM*. In an *EBSD* experiment an incident electron beam scans along the sample which is mounted in the *SEM* stage at the angle of 70° in respect to normal position. Usually, the accelerating voltage for the incident electron beam is (10-30) keV and the current of the incident beam is (1-50) nA. Upon interaction of

the primary electron beam with the sample, the electrons experience several acts of diffraction among the crystallographic planes of the sample. These acts of diffraction lead to the formation of diffraction patterns which are composed from the intersecting band (Kikuchi bands). These Kikuchi bands reflect the crystallographic structure of the lattice of the examined spot [158]. The resulting pattern is recorded by the *EBSD* detector which is attached to a *CCD* camera. As the result of the *EBSD* measurements an *orientation map* of the sample (Fig. 4.15), i.e a map which contains information about crystallographic orientation of each examined spot of the sample, can be composed.

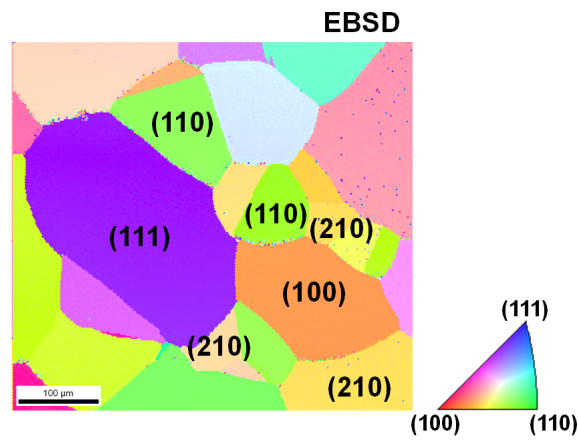


Figure 4.15: An example of an *EBSD* image of a polycrystalline *Pd* sample. Colours of different domains correspond to different crystallographic orientation in respect to inverse polar figure in the bottom right corner. Taken from ref. [127]

5 | *Reaction kinetics by imaging*

Basic idea

The idea of the *reaction kinetics by imaging* approach is based on the correlation of the change of the local *PEEM* brightness for the selected region of a model catalyst with the change of its catalytic activity which is monitored by means of a *QMS* [47]. Schematically, the basic idea of the approach is illustrated on a Fig. 5.1.

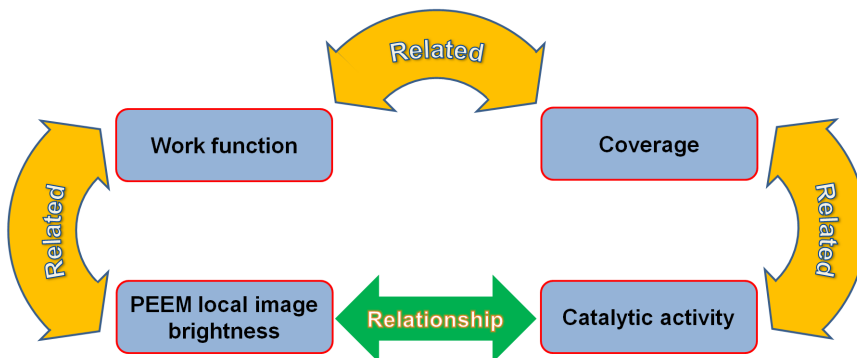


Figure 5.1: Illustration of the basic idea of the *reaction kinetics by imaging*. Change of the catalytic activity of the sample during the heterogenously catalysed reaction is related to the change of the sample surface coverage. The sample surface coverage, in turn, is related to change of the sample local work function. The local work function of the sample is related to local *PEEM* image brightness. Therefore, change of the local *PEEM* image brightness reflects change of catalytic activity of the sample.

As mentioned in section 4.1.2, the local brightness of the *PEEM* image is related to the local sample work function. In turn, the local sample work function is dependent on the coverage of the sample surface by adsorbed species. This relationship means that by monitoring the changes of the local *PEEM* image brightness for the *region of interest* (*ROI*), one can obtain information about the change of the surface coverage for this region. In turn, the coverages of the adsorbates affect the catalytic activity of the

sample. As mentioned in sections 2.4 and 2.5, in the case of the CO oxidation reaction on transition metal surfaces, the CO and oxygen coverages determine the catalytic activity of the model catalyst. In turn, the correlation of the catalytic activity of the model catalyst with work function dependent local $PEEM$ image intensity opens a possibility for monitoring the catalytic activity of a selected region of the model catalyst surface during ongoing CO oxidation by analysis of $PEEM$ video sequences which were recorded during the reaction, i.e. for study of the CO oxidation reaction on model catalyst surfaces using the *reaction kinetics by imaging*.

Experimental realization

In the present thesis, the experimental realization of the *reaction kinetics by imaging* was performed by using a $PEEM$ -150 (STAIB instruments). By monitoring the region of interest by $PEEM$ during the ongoing catalytic reaction (e.g. CO oxidation) and correlation of the obtained data with the CO partial pressure which is measured by a QMS , information about local reaction kinetics can be obtained. In parallel, by measurement of the partial pressure of the reactants (CO and oxygen) and reaction products (CO_2) by a QMS , the information about global (spatially averaged) reaction kinetics can be obtained (Fig. 5.2). By plotting the $PEEM$ intensity curves for the selected ROI on the sample as a function of CO partial pressure at constant oxygen pressure and constant temperature, the local hysteresis curves can be constructed. From these curves we can obtain the local information about kinetic transitions from active to inactive state and *vice versa**. By performing such experiments at the same oxygen partial pressures but at different temperatures, the local kinetic phase diagram for the selected ROI of the sample can be constructed. Comparison of kinetic phase diagrams for different regions of the sample allows to obtain information about the catalytic activity of different components of the model catalyst. Additionally, by evaluation of the data obtained by a QMS , the global R_{CO_2} hysteresis and thus the global kinetics phase diagram of the selected sample can be obtained. In the case of such a global kinetic phase diagram, all the information is attributed to the whole sample.

*see section 2.5 for details

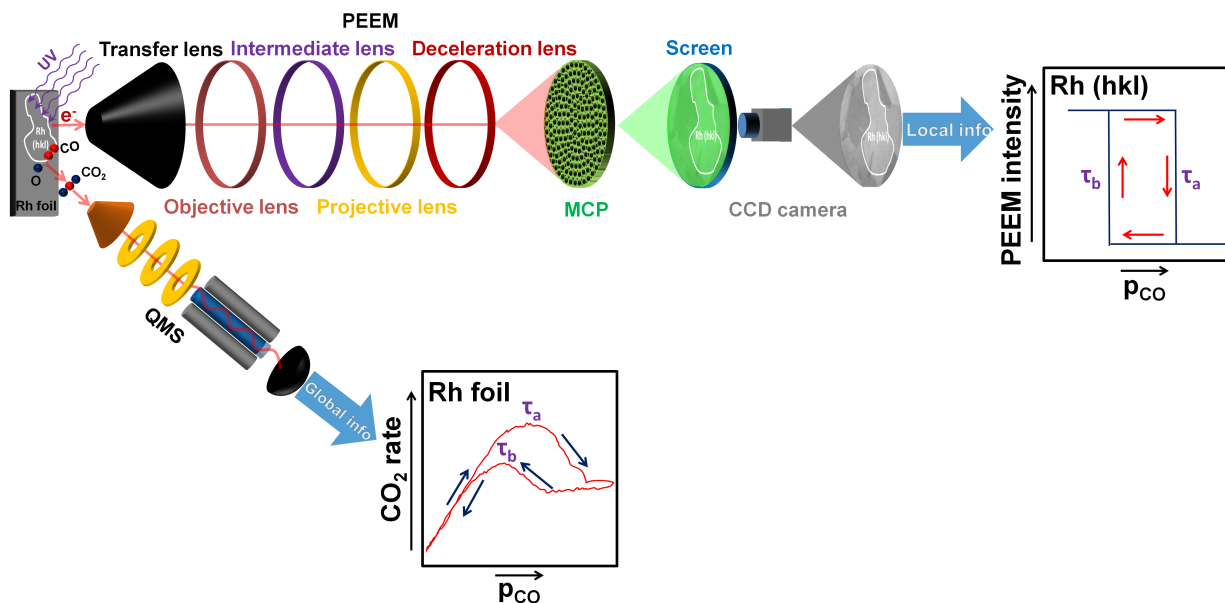


Figure 5.2: Experimental realization of the reaction kinetics by imaging. During the ongoing reaction the sample is simultaneously monitored by a *PEEM* and by a *QMS*. The global (spatially averaged) data which is obtained by a *QMS* (presented in lower inset) is correlated with the local (spatially resolved) data which was obtained by a *PEEM* (upper inset)

Since industrial catalysts are composed of different components, the spatially averaged techniques are less suitable for collecting information about the catalytic activity of individual components distributed on the sample surface. The *PEEM* allows monitoring of the catalytic activity of the selected spatially confined regions on the sample surface in real-time at exactly the same reaction conditions[†]. This allows a direct comparison of the components with different structure and composition, e.g. individual domains of polycrystalline foils, as well as μm -sized metal agglomerates supported by different supports.

[†]for more information see section 4.1

6 | *Experimental study of CO oxidation on stepped Rh surfaces*

Preparation and characterisation of the μm -sized stepped Rh domains

Formation and identification of high Miller index domains on Rh foil surface

To form well-defined domains of different crystallographic orientations on the *Rh* surface, the polycrystalline *Rh* foil was subjected to sputtering with Ar^+ ions of 1 keV energy (emission current 8 μA , *Ar* partial pressure of 10^{-5} mbar) for 15 min, followed by *UHV* annealing at 1173 K for 10 min. The procedure was repeated until formation of individual crystalline domains was observed by *PEEM*. The resulting surface consisted of μm -sized domains of 20 - 100 μm size of different crystallographic orientations (Fig. 6.1). For calibration of the magnification of the *PEEM* image, the same field of view was imaged using a differential interference contrast microscope (Polyvar 2 MET). The optical micrographs together with corresponding *PEEM* image are presented in Fig. 6.1.

In section 4.1.2 it was already discussed that the local intensity of the *PEEM* image is dependent on the local work function of the surface which, in turn, depends on the crystallographic orientation of the surface. This dependence might provide the orientation of surface domains just by comparison of the relative *PEEM* intensities with the values of the work functions for different crystallographic orientations.

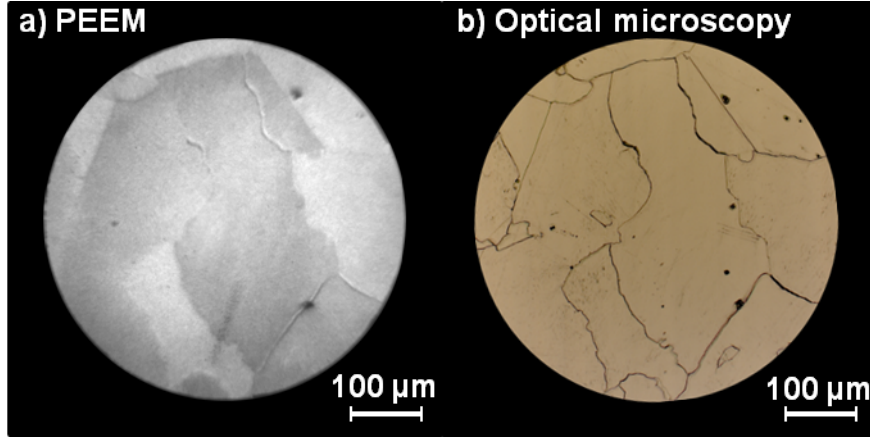


Figure 6.1: *PEEM* field of view showing the polycrystalline *Rh* surface: a) photoemission electron microscopy (*PEEM*); b) differential interference contrast microscopy.

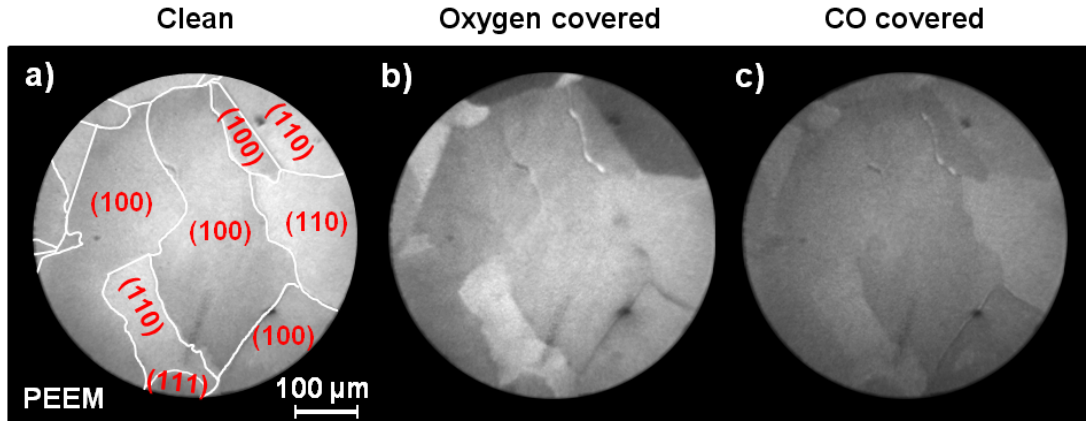


Figure 6.2: Contrast in *PEEM*: a) Clean *Rh* foil surface with marked individual domains, orientations are estimated from the work function values; b) the same region covered with oxygen; c) the same region covered with *CO*.

For such identification, the local intensity of a *PEEM* image for the chosen domains (Fig 6.2) was compared with the values of work function for low Miller index *Rh* single crystalline surfaces. The Table 6.1 summarizes the values of local work function for clean, *CO*- and oxygen covered *Rh* low Miller index single crystalline surfaces.

Table 6.1: Values of work function for the clean, oxygen and *CO* covered *Rh* (110), *Rh* (100), *Rh* (111) surfaces.

	Clean	Oxygen	CO
Rh(110)	4.94 eV [159]	not reported	+0.97 eV [160]
Rh(100)	5.25 eV [159]	+0.38 eV [160]	+1.30 eV [160]
Rh(111)	5.44 eV [159]	+0.75 eV [160]	+1.10 eV [160]

Based on the values presented in Table 6.1, the crystallographic orientations of the domains of the *Rh* polycrystalline sample were estimated and are marked in the Fig. 6.2 a. However, since only relative values can be compared in this way, the existence of vicinals cannot be excluded. In this case, additional measurements are necessary, e.g. *EBSD*. The *EBSD* measurements were carried out in a scanning electron microscope (FEI, Quanta 200F) which is equipped with a *EBSD* detector. The visualisation of the structure of domains of different crystallographic orientations was performed using VESTA software package. As was described in section 4.4, as a result of the *EBSD* measurements an color-coded orientation map of crystallographic orientations can be produced, where each colour, according to the *inverse pole figure* (IPF), is related to a certain set on Miller indices. The resulting *EBSD* image of the present *PEEM* field of view is shown in the Fig. 6.3 b.

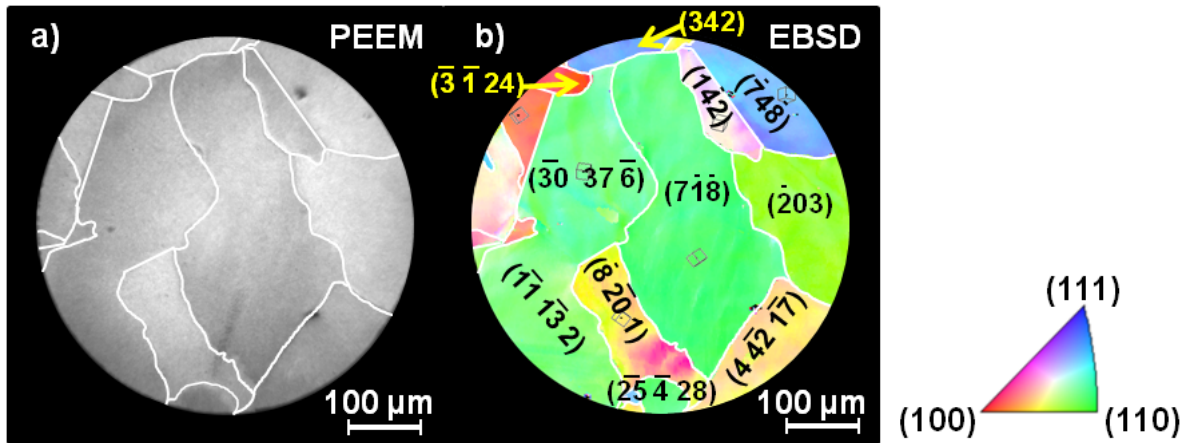


Figure 6.3: *PEEM versus EBSD*: a) *PEEM* image with marked grain boundaries of individual domains; b) the same but imaged with *EBSD*, where the exact orientations are labeled.

Based on the *EBSD* measurements, the exact crystallographic orientations of the domains were determined. The quantitative results from Fig. 6.3 show that the qualitative results based on the evaluation of work function (Fig. 6.2 a) are not always correct: in fact, the exact orientations are vicinals and only the basic type of the vicinal orientation can be estimated from the work function in present case. It appeared from *EBSD* measurements that all the domains in the field of view are vicinals, thus high index stepped *Rh* surfaces.

XPS characterization of Rh sample surface

The chemical composition and the cleanness of the studied sample were controlled by XPS. In the Figure 6.4, a survey spectrum and a high resolution Rh 3d spectrum of clean polycrystalline Rh sample are presented. Deconvolution of the Rh 3d spectrum was performed using CasaXPS software package. The Rh 3d spectrum was fitted using the Gaussian/Lorentzian sum function with asymmetric peak shape, with the peak shape and peak extension asymmetry having identical values for both $3d_{3/2}$ and $3d_{5/2}$ peaks. The full width at half maximum (FWHM) was identical for both $3d_{3/2}$ and $3d_{5/2}$ peaks and had a value of 1.8 eV. The binding energy of the Rh $3d_{3/2}$ and Rh $3d_{5/2}$ peaks were 311.8 eV and 307.1 eV, respectively. The value of spin-orbital splitting for these two peaks was 4.7 eV. From the Figure 6.4 one can see that carbon, presented on the surface, was in negligible amounts. Presence of another impurities on the sample surface was not detected. Formation of Rh oxide after the cleaning procedure was also not detected.

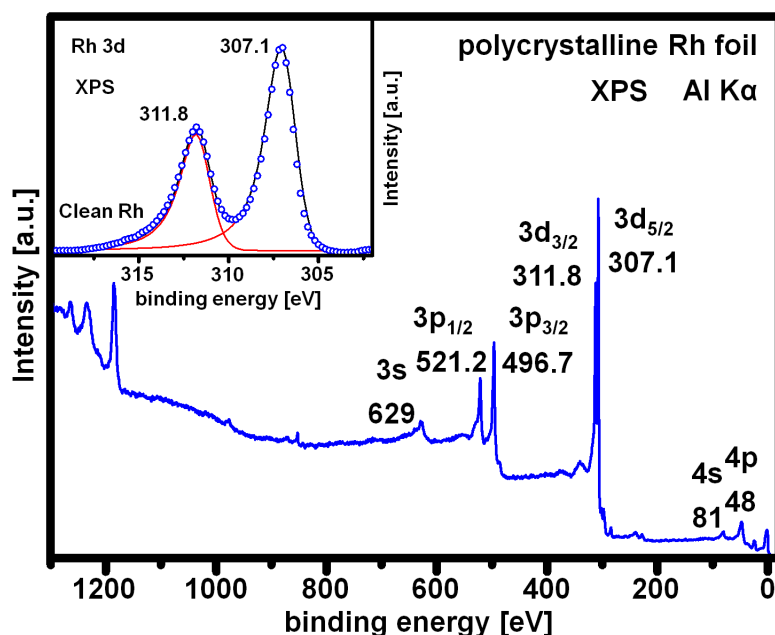


Figure 6.4: XPS survey spectrum of the clean polycrystalline Rh foil. The inset shows a detailed XPS spectrum measured from Rh 3d region.

Global reaction kinetics of CO oxidation on polycrystalline Rh foil

In the present section, the study of the global kinetic behaviour of CO oxidation on the whole Rh sample surface is presented. For global measurements, QMS monitoring of the CO_2 production rate (R_{CO_2}) was conducted while the CO partial pressure was varied cyclewise from 10^{-9} mbar to 10^{-4} mbar and *vice versa*. Oxygen pressure and Rh sample temperature were kept constant. An exemplary R_{CO_2} curve as a function of CO partial pressure at constant oxygen pressure of 1×10^{-6} mbar and temperature of 433 K is shown as the inset in the Fig. 6.5. This curve has a hysteresis shape with two characteristic transition points: τ_a and τ_b . These transition points mark the global kinetic transitions from the active (oxygen covered) steady state to the inactive (CO covered) steady state or *vice versa*.

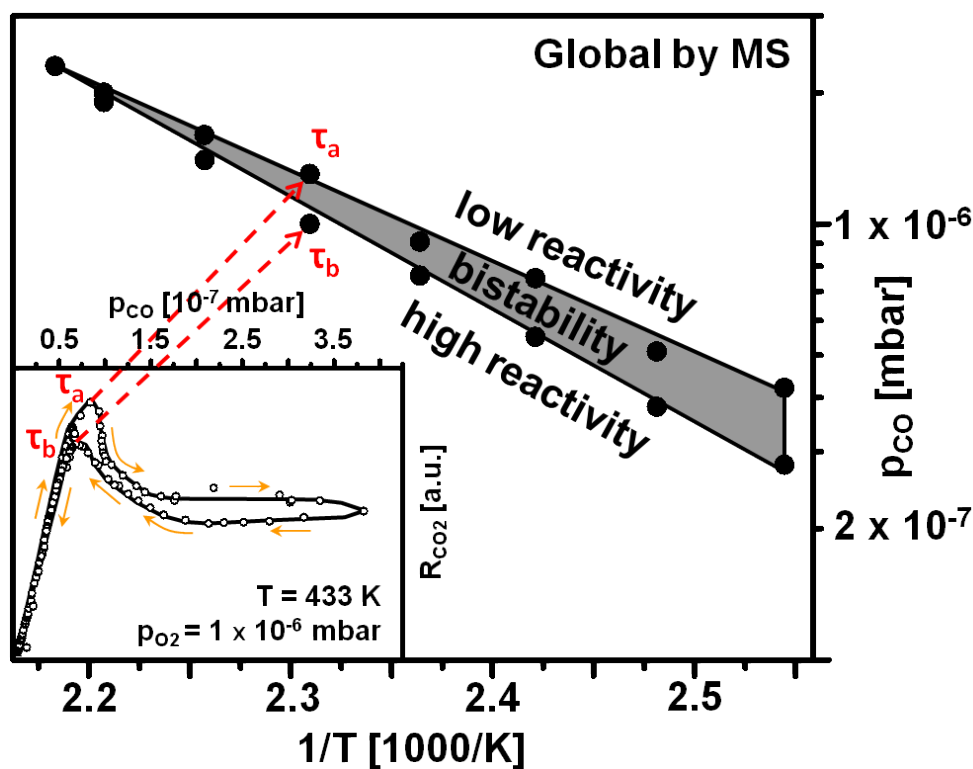


Figure 6.5: Global reaction kinetics of CO oxidation on stepped polycrystalline Rh surface. The inset shows the global R_{CO_2} hysteresis measured at constant oxygen pressure of 1×10^{-6} mbar and constant temperature of 433 K. From such hysteresis curves measured at constant oxygen pressure of 1×10^{-6} mbar and in the temperature range of 393 to 458 K, the global kinetic phase diagram is constructed.

The first kinetic transition point τ_a is defined here as a point where CO_2 production rate starts to drop at increasing p_{CO} . At low CO pressure, the Rh surface is covered with oxygen and resides in active steady state, where an increase of the CO partial pressure leads to the linear increase of the CO_2 production (R_{CO_2}). At τ_a the CO adsorption rate is so high, that adsorbed CO blocks adsorption sites necessary for dissociative adsorption of oxygen and therefore CO_2 production drops down. When one decreases the CO partial pressure, at certain CO partial pressure the R_{CO_2} increases again and the surface switches back to oxygen covered (active) steady state: the kinetic transition τ_b occurs. This kinetic transition usually occurs at lower CO partial pressures than (τ_a) which can be explained by asymmetry of adsorption properties of oxygen and CO on the transition metal surfaces. By repeating the measurements at identical constant partial pressure of oxygen of 1×10^{-6} mbar, but for different temperature in the range of 393 to 458 K a set of τ_a and τ_b values was obtained. These τ_a and τ_b values are plotted as *kinetic phase diagram* in the Fig. 6.5, where the steady state regions of high and low activity and region of bistability are marked. This plot summarizes all possible catalytic states of the studied system (in present case, polycrystalline Rh foil) for given ranges of pressure and temperature. However, such global diagrams provide just average characteristics of the catalytic behaviour of the sample. The individual behaviour of the different domains cannot be considered in this way, thus local measurements with spatial resolution in μm -range are necessary.

Local reaction kinetics of CO oxidation on stepped Rh surfaces

CO oxidation on (111)-type vicinal Rh surfaces

In the present section, the study of kinetic behaviour of CO oxidation on individual high Miller index Rh surfaces is presented. The studies were performed by measurements of local *PEEM* intensity during the cyclic variation of CO partial pressure at constant oxygen pressure and at constant temperature as described in the previous section for global *QMS* measurements. We concentrate first on (111)-type vicinal Rh surface, namely on $Rh(1\bar{1}2)$ (Fig. 6.6).

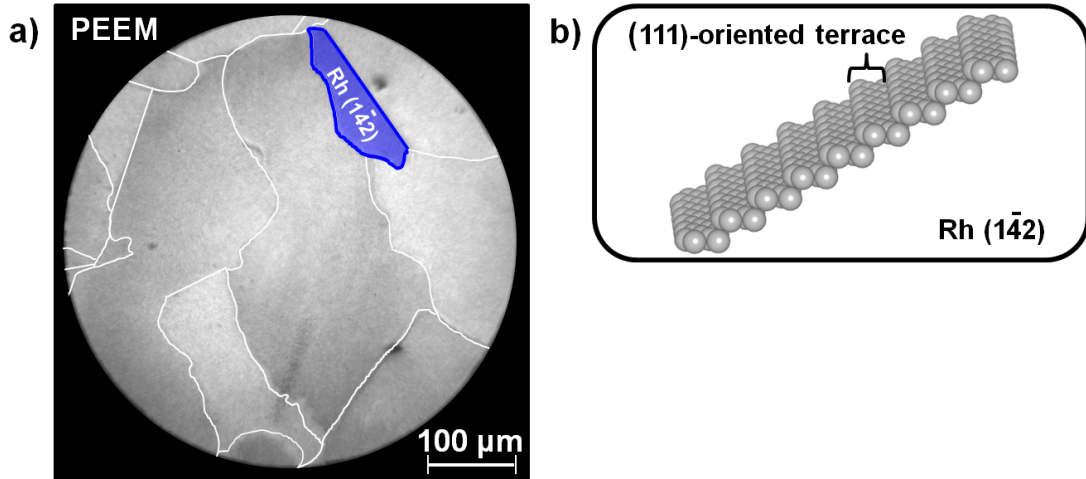


Figure 6.6: $Rh(1\bar{4}2)$ surface: **a)** $Rh(1\bar{4}2)$ domain marked on the *PEEM* image of polycrystalline Rh foil; **b)** a ball model of $Rh(1\bar{4}2)$ surface structure.

The $Rh(1\bar{4}2)$ domain is composed of (111)-oriented terraces (4 atomic rows wide) and steps of one atom height. The variations of the *PEEM* intensity for a *ROI*, virtually placed on this surface, is presented in the inset of the Fig 6.7 as a function of CO partial pressure varied cyclically at constant oxygen partial pressure of 1×10^{-6} mbar and at constant temperature of 403 K. Again, as in the global measurements, the hysteresis curve provides information about the local kinetic transitions τ_a and τ_b , from active to inactive steady states and *vice versa*. The *PEEM* video frames corresponding to the selected points on the local *PEEM* intensity hysteresis are also presented in the Fig. 6.7. In frame 1, the surface is covered by oxygen and resides in the active steady state. Frame 2 illustrates the local kinetic transition τ_a , i.e. the transition from active (oxygen covered) steady state to inactive (CO covered) steady state which occurs on the $Rh(1\bar{4}2)$ domain. During this kinetic transition, the dark CO reaction-diffusion front propagates along the surface of the $Rh(1\bar{4}2)$ domain. This propagating front is confined by the grain boundaries, which indicate individual reaction behaviour of the $Rh(1\bar{4}2)$ domain. Propagation of the CO reaction front leads to sharp decrease of the local intensity of the image within the selected domain. Frame 3, in turn, corresponds to the surface residing in an inactive (CO covered) steady state. Frame 4 shows the surface residing in the active (oxygen covered) steady state again.

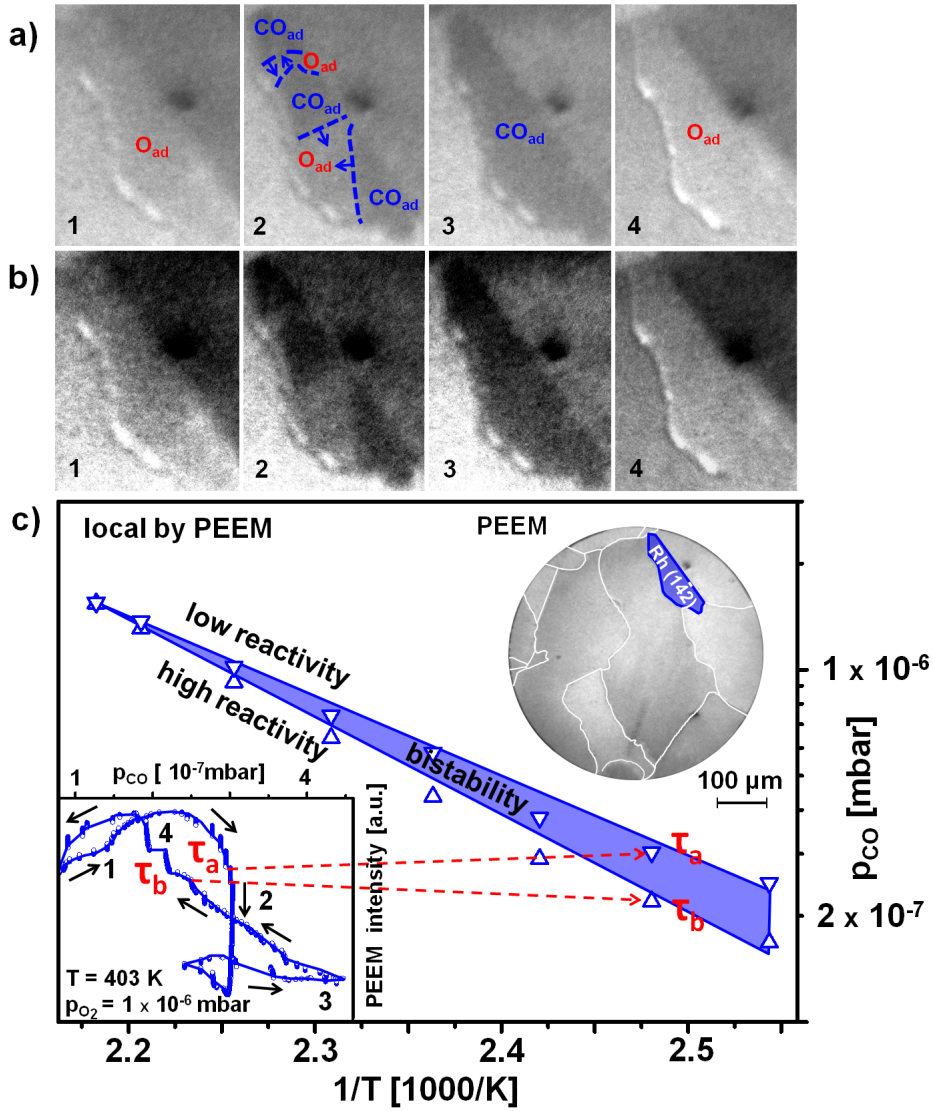


Figure 6.7: Local reaction kinetics of CO oxidation on an individual $Rh(142)$ domain: **a)** *PEEM* images recorded *in situ* during the CO oxidation on $Rh(142)$ surface during a cyclewise variation of CO pressure at constant $p_{O_2} = 1 \times 10^{-6}$ mbar and at constant temperature $T = 403$ K: **(1)** $Rh(142)$ domain covered with oxygen (active steady state); **(2)** the same domain, but during the local kinetic transition from active steady state (oxygen covered) to inactive steady state (CO covered); **(3)** the same domain, but covered with CO (inactive steady state); **(4)** the same domain, but again in the active steady state; **b)** the same images as in **(a)**, but with enhanced contrast for a better visibility of the reaction fronts; **c)** corresponding local kinetic phase diagram for the constant oxygen pressure of 1×10^{-6} mbar in the temperature range of 393 to 458 K. The inset shows the local *PEEM* intensity hysteresis which measured at constant oxygen pressure of 1×10^{-6} mbar and at constant temperature of 403 K. The numbers on the hysteresis curve correspond to the *PEEM* frames in **(a)**.

By performing of series of local kinetic measurements at pressure of 1×10^{-6} mbar, but at different temperatures in the range of 393 to 458 K, the local kinetic phase

diagram for the particular $Rh(1\bar{4}2)$ domain was constructed (Fig. 6.7). As in the case of the global kinetic phase diagrams, the local kinetic phase diagram summarizes steady states of high and low activity and bistability. But, in the case of local kinetic measurements by *PEEM* all these states are not averaged over the whole sample, but are attributed to the selected spatially confined part of the sample.

CO oxidation on (100)-type vicinal Rh surfaces

The kinetic behaviour of *CO* oxidation reaction was also studied on the (100)-type vicinal *Rh* surfaces. As in the previous section, the studies were performed by measurements of local *PEEM* intensity during cyclic variation of *CO* partial pressure at constant oxygen pressure and at constant temperature. In present section, the attention was paid to the $Rh(4\bar{4}2\bar{1}7)$ surface (Fig 6.8).

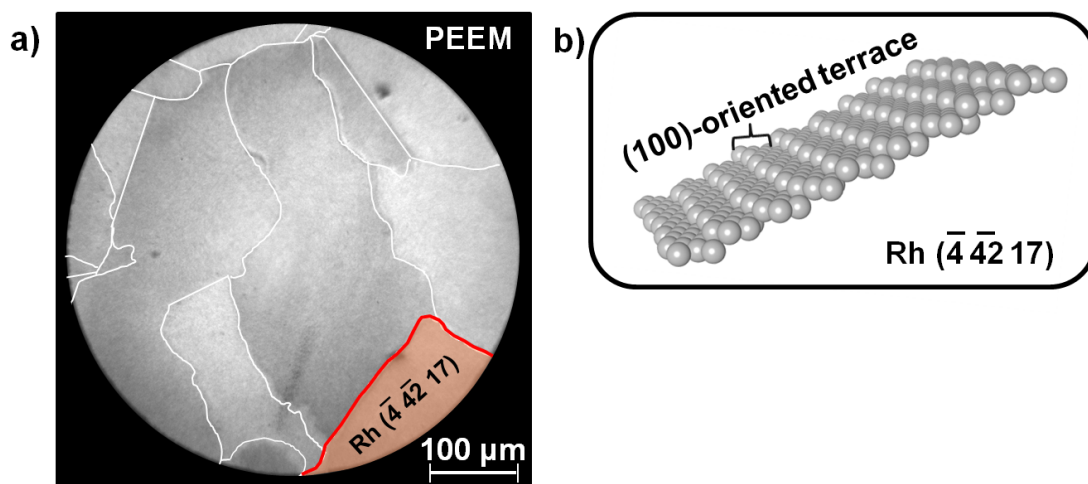


Figure 6.8: $Rh(4\bar{4}2\bar{1}7)$ surface: a) $Rh(4\bar{4}2\bar{1}7)$ domain marked on the *PEEM* image of *Rh* polycrystalline foil; b) a ball model of $Rh(4\bar{4}2\bar{1}7)$ surface structure.

The studied $Rh(4\bar{4}2\bar{1}7)$ surface is composed of (100)-oriented terraces (4 atomic rows wide) and steps of the one atom height. The *PEEM* intensity for a *ROI* placed on this surface is presented in the inset of Fig 6.9 as a function of *CO* partial pressure which was varied cyclically at a constant oxygen partial pressure of 1×10^{-6} mbar and at a constant temperature of 403 K. Similarly to the previous type of the surface, the hysteresis curve provides information about the local kinetic transitions τ_a and τ_b , from active to inactive steady states and *vice versa*. The *PEEM* video frames corresponding to the selected points on the local *PEEM* intensity hysteresis are presented

in the Fig. 6.9. In the frame 1, the whole domain surface is covered with oxygen and resides in the active steady state.

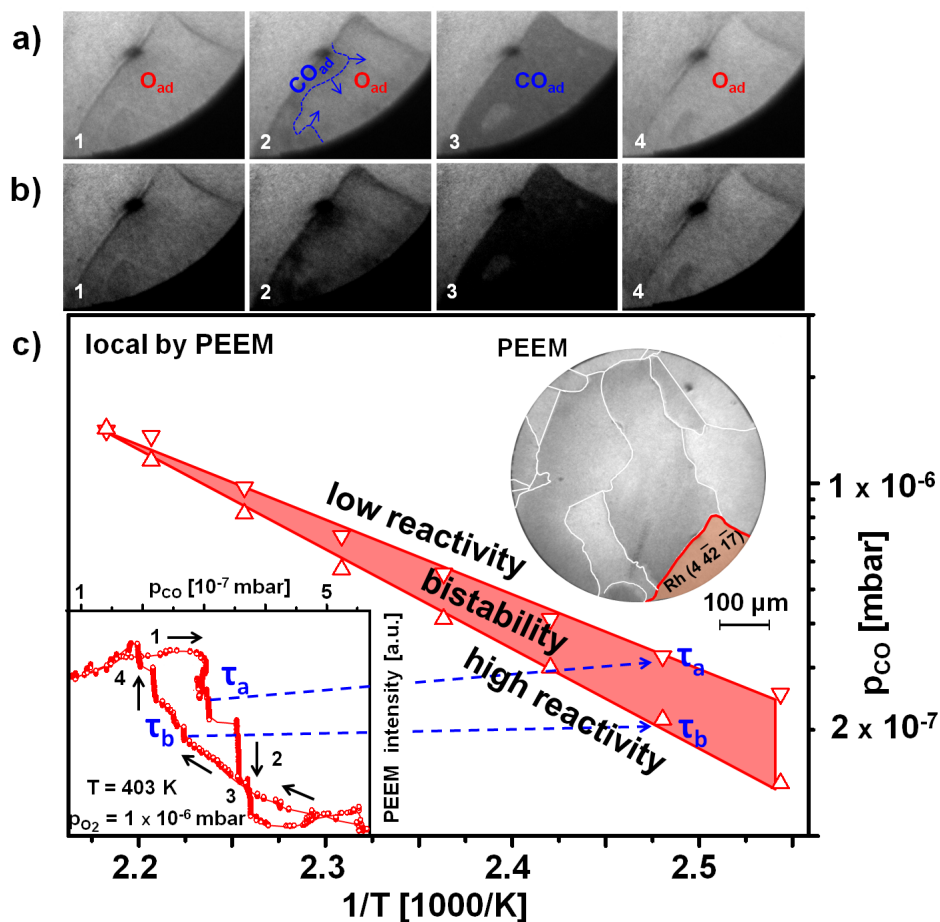


Figure 6.9: Local reaction kinetics of CO oxidation on an individual $Rh(4 \bar{4}2 \bar{1}7)$ domain: **a)** *PEEM* images recorded *in situ* during the CO oxidation on a $Rh(3\bar{0}37\bar{6})$ surface: (1) $Rh(4 \bar{4}2 \bar{1}7)$ domain covered with oxygen (active steady state); (2) the same domain, but during the local kinetic transition from the active steady state (oxygen covered) to the inactive steady state (CO covered); (3) the same domain, but covered with CO (inactive steady state); (4) the same domain, but again in the active steady state; **b)** the same images as in (a), but with enhanced contrast; **c)** local kinetic phase diagram constructed at constant oxygen pressure of 1×10^{-6} mbar in the temperature range of 393-458 K. The inset shows local *PEEM* intensity hysteresis measured at constant oxygen pressure of 1×10^{-6} mbar and at constant temperature of 403 K. Numbers on the hysteresis curve correspond to the *PEEM* frames in (a).

Frame 2 illustrates the local kinetic transition from active steady state (oxygen covered surface) to inactive steady state (CO covered surface), which occurs on the $Rh(4 \bar{4}2 \bar{1}7)$ domain, i.e kinetic transition τ_a . The kinetic transition τ_a is accompanied by the propagation of a dark CO reaction-diffusion front, which propagates along the

surface of the $Rh(4\bar{4}2\bar{1}7)$ domain. As in the case of (111)-type vicinal Rh surface, the propagation of the CO reaction-diffusion is confined by the grain boundaries, which indicated the individual reaction behaviour of the selected $Rh(4\bar{4}2\bar{1}7)$ domain. The frame 3 shows the surface covered with CO , i.e. in the inactive steady state. The kinetic transition τ_b , i.e. kinetic transition from the inactive to the active steady state during the CO oxidation on $Rh(4\bar{4}2\bar{1}7)$ domain surface is accompanied by a rapid change of local $PEEM$ image intensity. Frame 4 shows the surface domain $Rh(4\bar{4}2\bar{1}7)$ residing in the active (oxygen covered) steady state. By performing of series of local kinetic measurements at an identical pressure of 1×10^{-6} mbar, but at different temperatures in the range of 393 to 458 K, the local kinetic phase diagram was constructed (Fig 6.9 b). Similarly to the $Rh(1\bar{4}2)$ in the previous section, this diagram summarizes steady states of high activity, low activity and bistability for a spatially confined part of the sample, in the present case for the $Rh(4\bar{4}2\bar{1}7)$ domain.

CO oxidation on (110)-type vicinal Rh surfaces

Apart of the (111)-and (100)-type surfaces, the kinetic behaviour of CO oxidation reaction was studied on the (110)-type vicinal Rh surfaces, in this case, on the $Rh(7\bar{1}\bar{8})$ surface (Fig 6.10). The $Rh(7\bar{1}\bar{8})$ surface is composed of (110)-oriented terraces (7 atomic steps wide) and steps of one atom height.

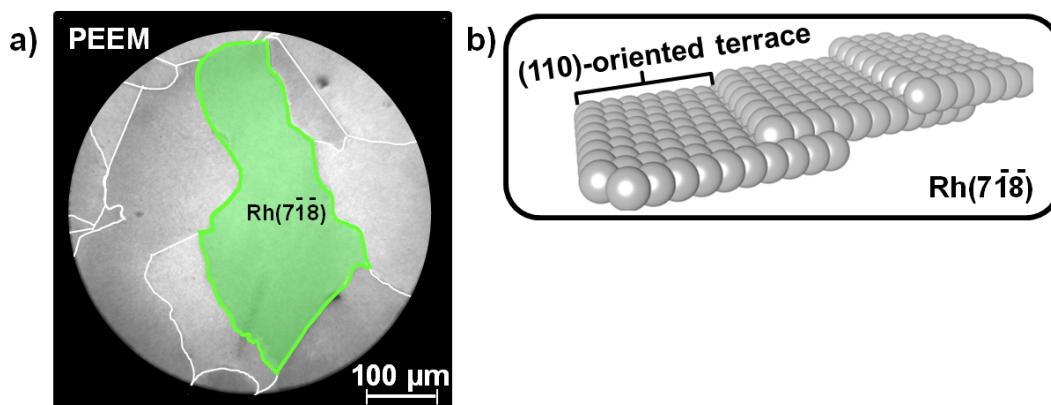


Figure 6.10: $Rh(7\bar{1}\bar{8})$ surface: **a)** $Rh(7\bar{1}\bar{8})$ domain marked on the $PEEM$ image of Rh polycrystalline foil; **b)** a ball model of $Rh(7\bar{1}\bar{8})$ surface structure.

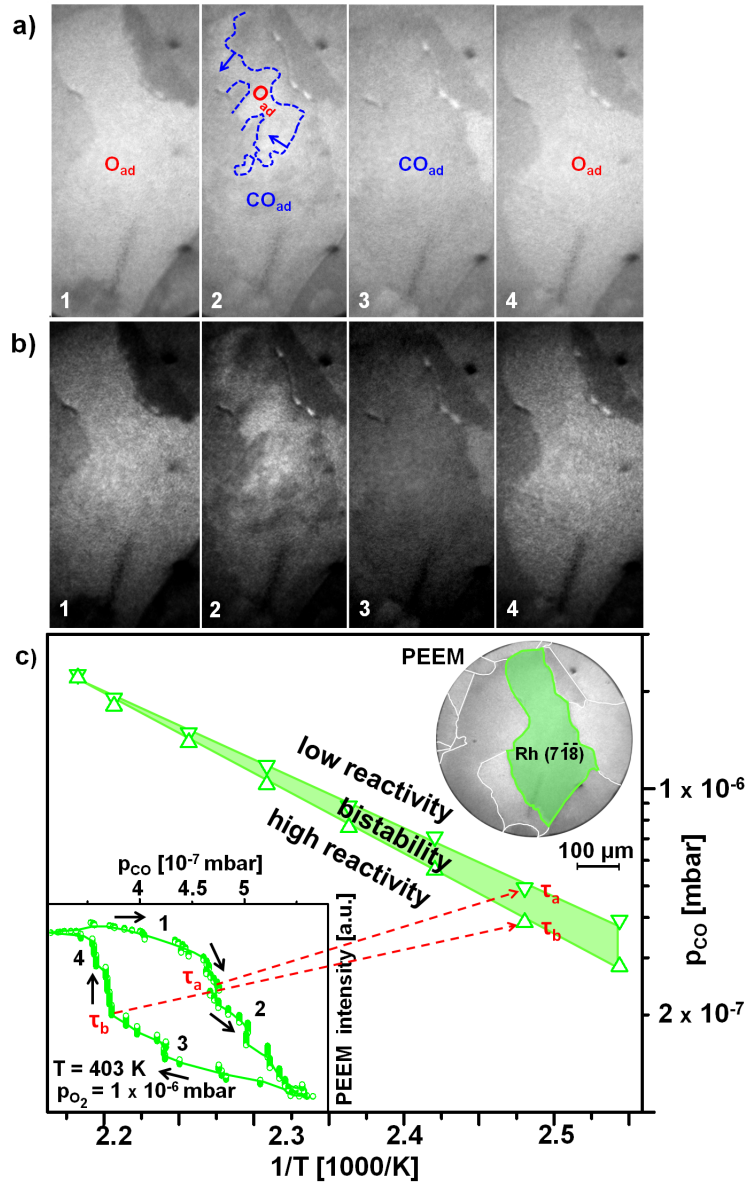


Figure 6.11: Local reaction kinetics of CO oxidation on an individual $Rh(7\bar{1}\bar{8})$ domain: **a)** *PEEM* images recorded *in situ* during the CO oxidation on $Rh(7\bar{1}\bar{8})$ domain: (1) $Rh(7\bar{1}\bar{8})$ domain covered with oxygen (active steady state), (2) the same domain, but during the local kinetic transition from active steady state (oxygen covered) to inactive steady state (CO covered), (3) the same domain, but covered with CO (inactive steady state), (4) the same domain, but in the active steady state again; **b)** the same images as in (a), but with enhanced contrast; **c)** local kinetic phase diagram constructed at constant oxygen pressure of 1×10^{-6} mbar in the temperature range of 393–458 K. The inset shows local *PEEM* intensity hysteresis which was measured at constant oxygen pressure of 1×10^{-6} mbar and constant temperature of 403 K. Numbers on the hysteresis curve correspond to the *PEEM* frames in (a).

As for (111)- and (100)-type vicinal surfaces, information about local reaction behaviour of the selected $Rh(7\bar{1}\bar{8})$ domain was obtained by evaluation of local *PEEM*

intensity during cyclic variation of CO partial pressure at constant temperature and oxygen partial pressure. The inset of the Fig 6.11 shows the local $PEEM$ intensity hysteresis curve as a function of CO partial pressures measured at constant oxygen partial pressure of 1×10^{-6} mbar and constant temperature of 403 K. Again, as in the previous sections, analysis of the local $PEEM$ intensity hysteresis curve provides the local kinetic transition points τ_a and τ_b . The hysteresis curve is illustrated by corresponding *in situ* $PEEM$ video frames (Fig. 6.11 a, b).

Frames 1 and 4 show the $Rh(7\bar{1}\bar{8})$ domain residing in the active steady state, frame 2 shows the transition τ_a and frame 3 an inactive steady state, correspondingly. By performing of series of such local kinetic measurements at an identical oxygen pressure of 1×10^{-6} mbar, but at different temperatures in the range of 393 to 458 K, the local kinetic phase diagram could be constructed (Fig 6.11 b). This diagram summarizes steady states of high activity, low activity and bistability for a spatially confined part of the sample, in the present case for the $Rh(7\bar{1}\bar{8})$ domain.

Step density and other structure effects in the CO oxidation on vicinal Rh surfaces

In this section, more results for the surfaces vicinal to the $Rh(111)$, $Rh(110)$ and $Rh(110)$ are presented in order to compare the behaviour of different orientations and to reveal the structure effects.

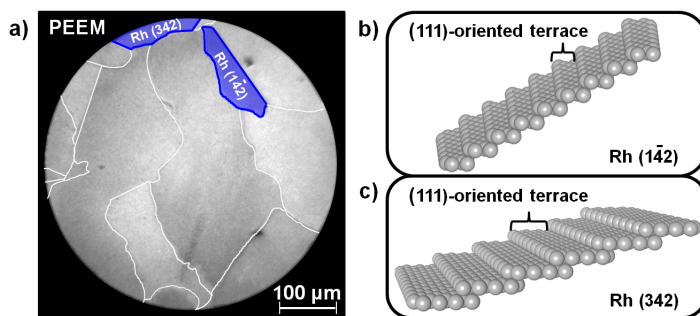


Figure 6.12: $Rh(1\bar{4}2)$ and $Rh(342)$ surfaces, both vicinal to $Rh(111)$: **a)** $Rh(1\bar{4}2)$ and $Rh(342)$ domains marked on the $PEEM$ image of a Rh polycrystalline foil; **(b, c)** ball models of $Rh(1\bar{4}2)$ and $Rh(342)$ surfaces, correspondingly.

An *in situ* recording of the *PEEM* images during the *CO* oxidation reaction allows the simultaneous tracking of *PEEM* intensity for all surfaces within the *PEEM* field of view. Based on these measurements, the local kinetics phase diagrams could be obtained under the identical conditions for all selected surface. First, we compare two *Rh* surfaces vicinal to *Rh* (111), namely *Rh* (342) and *Rh* ($\bar{1}\bar{4}2$) (Fig. 6.12 a-c). These surfaces, are composed of (111)-oriented terraces (6 and 4 atomic rows wide, respectively) and steps of 1 atom height (Fig. 6.12 b,c). The comparison of corresponding local kinetic phase diagrams is shown in the Fig. 6.13.

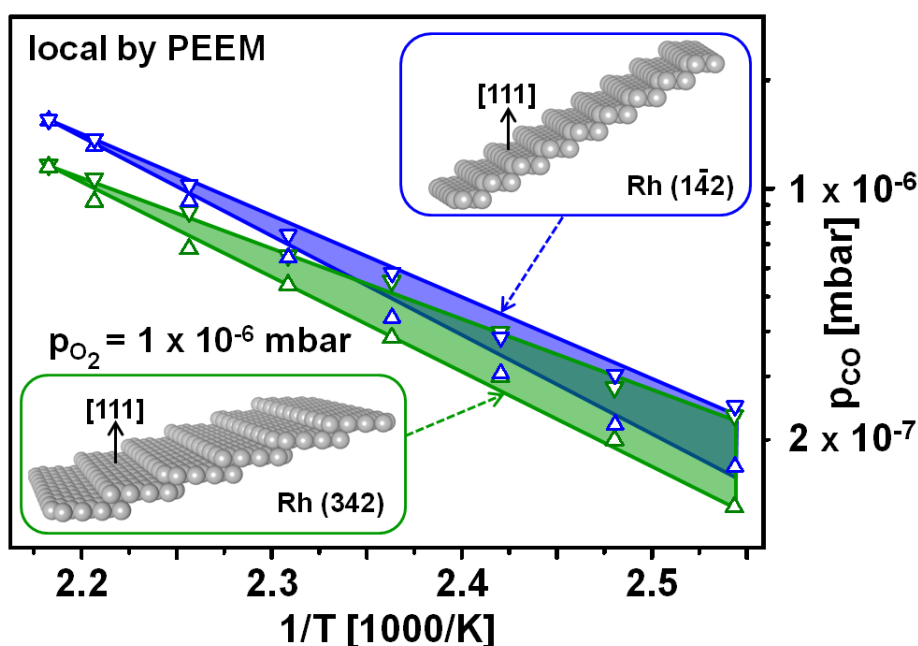


Figure 6.13: Comparison of the local kinetic phase diagrams for *Rh* ($\bar{1}\bar{4}2$) and *Rh* (342) surfaces constructed at constant oxygen pressure of 1×10^{-6} mbar and in the temperature range of 393 to 458 K. Ball models of stepped *Rh* ($\bar{1}\bar{4}2$) and *Rh* (342) surfaces are shown in the insets.

The comparison shows that the kinetic phase diagram measured for *Rh* ($\bar{1}\bar{4}2$) surface is shifted towards the higher *CO* partial pressures in comparison to the diagram measured for *Rh* (342). Such a shift of the kinetic phase diagram shows that the *Rh* ($\bar{1}\bar{4}2$) surface exhibits higher tolerance towards the *CO* poisoning, than the *Rh* (342) surface. Moreover, the ability of *Rh* ($\bar{1}\bar{4}2$) to reactivation is higher than for *Rh* (342), due to the fact that kinetic transition τ_b from inactive to active steady state takes place on

$Rh(1\bar{4}2)$ at higher CO partial pressures than on the $Rh(342)$ surface.

A similar comparison was also performed for the $Rh(110)$ -vicinal surfaces, namely $Rh(4\bar{4}2\bar{1}7)$ and $Rh(\bar{3}\bar{1}24)$, which are composed of (100) -oriented terraces (11 and 4 atomic rows wide, respectively) and a step of 1 atom height (Fig. 6.14 b,c).

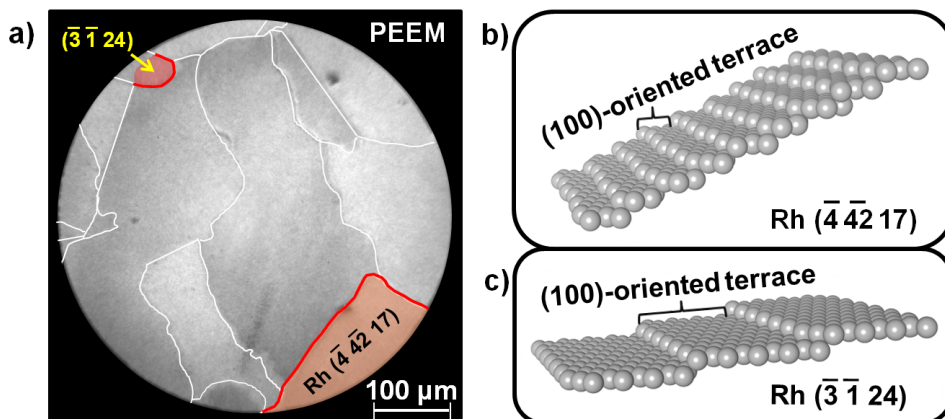


Figure 6.14: $Rh(4\bar{4}2\bar{1}7)$ and $Rh(\bar{3}\bar{1}24)$ surfaces, vicinal to $Rh(100)$: a) $Rh(4\bar{4}2\bar{1}7)$ and $Rh(\bar{3}\bar{1}24)$ surfaces marked on the PEEM image of Rh polycrystalline foil; (b, c) ball model of the $Rh(4\bar{4}2\bar{1}7)$ and $Rh(\bar{3}\bar{1}24)$ surfaces.

Again, the catalytic performance of these surfaces was compared by the comparison of the local kinetic phase diagrams, which were constructed for these surfaces at exactly the same reaction conditions (Fig. 6.15). The diagram, constructed for Rh surface $Rh(4\bar{4}2\bar{1}7)$ appears to be located at higher CO partial pressures than the corresponding diagram for $Rh(\bar{3}\bar{1}24)$ surface. Such a shift of local phase diagram for $Rh(4\bar{4}2\bar{1}7)$ shows the higher tolerance of this surface towards the CO poisoning and higher ability to reactivate in comparison to $Rh(\bar{3}\bar{1}24)$.

Generally, we see similar peculiarities in the catalytic behaviour of the (111) -type and (100) -type vicinal surfaces: the shift of the diagrams for (111) - and (100) -vicinal surfaces to higher CO pressure is correlated with the differences in step atom density for these surfaces. Indeed, in the case of (111) -vicinal surfaces, the surface, which is poisoned by CO at lower pressures is composed of (111) -oriented terraces of 6 atoms wide and steps of one atom height. On the other hand, a surface, which is poisoned at higher pressures is composed of 3 atoms wide and one-atom height steps.

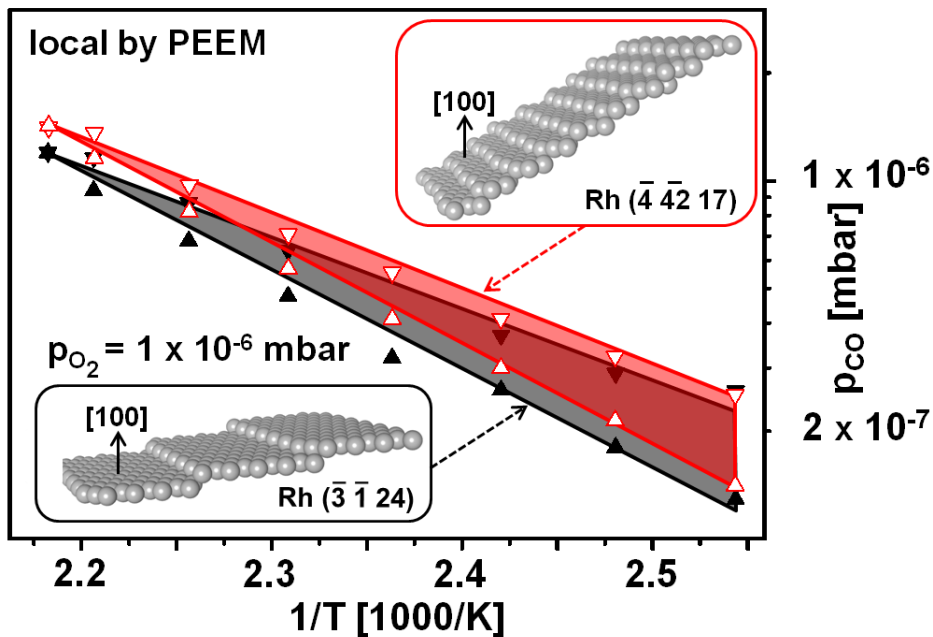


Figure 6.15: Comparison of the local kinetic phase diagrams for $Rh (4 \bar{4} 2 \bar{1} 7)$ and for $Rh (\bar{3} \bar{1} 2 4)$ surfaces constructed at constant oxygen pressure of 1×10^{-6} mbar and in the temperature range of 393 to 458 K. Ball models of stepped $Rh (4 \bar{4} 2 \bar{1} 7)$ and $Rh (\bar{3} \bar{1} 2 4)$ surfaces are shown in insets.

Comparison of the ball models of these two surfaces showed that a surface with higher tolerance to CO poisoning has 25% step atom density, whereas, the surface with lower tolerance to CO poisoning has only 16% step atom density. This means that the surface with higher tolerance to CO poisoning contains twice as many steps per unit area than the surface with lower tolerance to CO poisoning. Similar effect, namely an increase of the catalytic performance of the surface with increase step atom density, was observed for the case of the (100)-vicinal terraces. The vicinal surface with higher step atom density of 33% ($Rh (4 \bar{4} 2 \bar{1} 7)$) exhibited higher tolerance to CO , than the stepped surface with lower density of step atoms of 12% ($Rh (\bar{3} \bar{1} 2 4)$). Or, in other words, in this case the surface, which is poisoned at relatively high CO partial pressures has three times more steps than the surface which is poisoned by CO at lower CO partial pressures.

Such a difference in catalytic performance for surfaces with different step atom densities could be explained by the fact that adsorption properties of oxygen and CO are dependent on the density of defects (in present case, step atom densities), which are exhibited on the surfaces. Indeed, for the case of Rh single crystalline surfaces, it was

shown that oxygen binds more strongly on the surfaces with higher defect density, than on the less defected surfaces [161, 162]. The binding energy of CO on the Rh surfaces can be increased by increase of density of defect on the surface. However, the increase of CO binding energy is relatively small in comparison with that of oxygen [163, 164]. Therefore, due to the relation between kinetics and energetics of competitive oxygen and CO co-adsorption, poisoning by CO on the highly stepped surfaces, takes place at higher CO pressures than on the less stepped surfaces. On the other hand, the surface with high defect density has more adsorption sites for oxygen on CO covered surface, therefore the reactivation takes place at higher CO pressures on such surfaces .

A similar comparison was also performed for the (110)-type vicinal surfaces. Within the $PEEM$ field of view there are also two such surfaces visible, namely $Rh(7\bar{1}\bar{8})$ and $Rh(\bar{1}\bar{1}\bar{1}\bar{3}\bar{2})$. They are composed of (110)-oriented terraces (7 and 5 atoms wide, respectively) and steps of one atom height (Fig. 6.16).

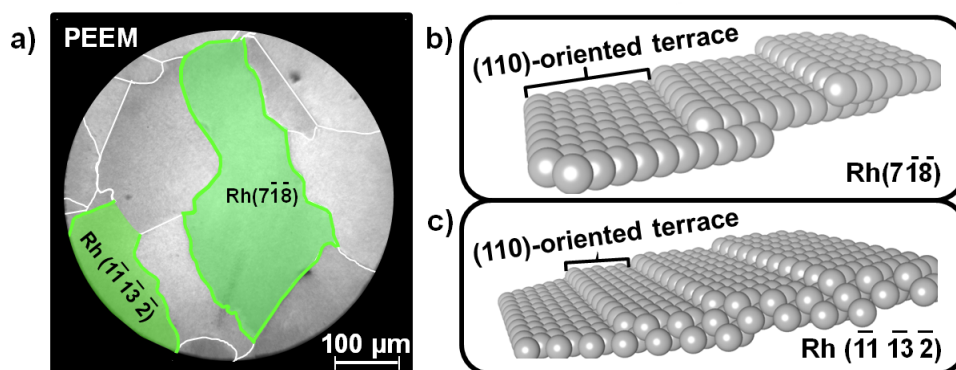


Figure 6.16: $Rh(7\bar{1}\bar{8})$ and $Rh(\bar{1}\bar{1}\bar{1}\bar{3}\bar{2})$ surfaces, vicinal to $Rh(110)$: **a)** $Rh(7\bar{1}\bar{8})$ and $Rh(\bar{1}\bar{1}\bar{1}\bar{3}\bar{2})$ surfaces marked on the $PEEM$ image of Rh polycrystalline foil; **(b, c)** ball models of $Rh(7\bar{1}\bar{8})$ and $Rh(\bar{1}\bar{1}\bar{1}\bar{3}\bar{2})$ surfaces.

Since the $PEEM$ video data is obtained for the whole field of view, it contains also data for the $Rh(7\bar{1}\bar{8})$ and $Rh(\bar{1}\bar{1}\bar{1}\bar{3}\bar{2})$, thus the local kinetic phase diagrams can be constructed for these surfaces (Fig. 6.17). The comparison of the diagrams shows unexpectedly, that an increase the step density, i.e decrease of the width of the terraces from 7 to 6 atomic rows leads to the shift of local kinetic phase diagram to the lower CO pressures. This is in the opposite direction as observed for $Rh(111)$ - and $Rh(110)$ -vicinal surfaces. To explain such an "opposite" shift of the diagrams for the (110)-type vicinals we refer to the fact that the $Rh(110)$ -type surface has generally more open surface structure than $Rh(110)$ - and $Rh(111)$ -type surfaces and therefore

may incorporate oxygen more easily. This incorporation could lead to formation of subsurface oxygen or a surface oxide under present reaction conditions and may hence lead to significant changes of the catalytic behaviour of selected Rh (110)-vicinal surfaces.

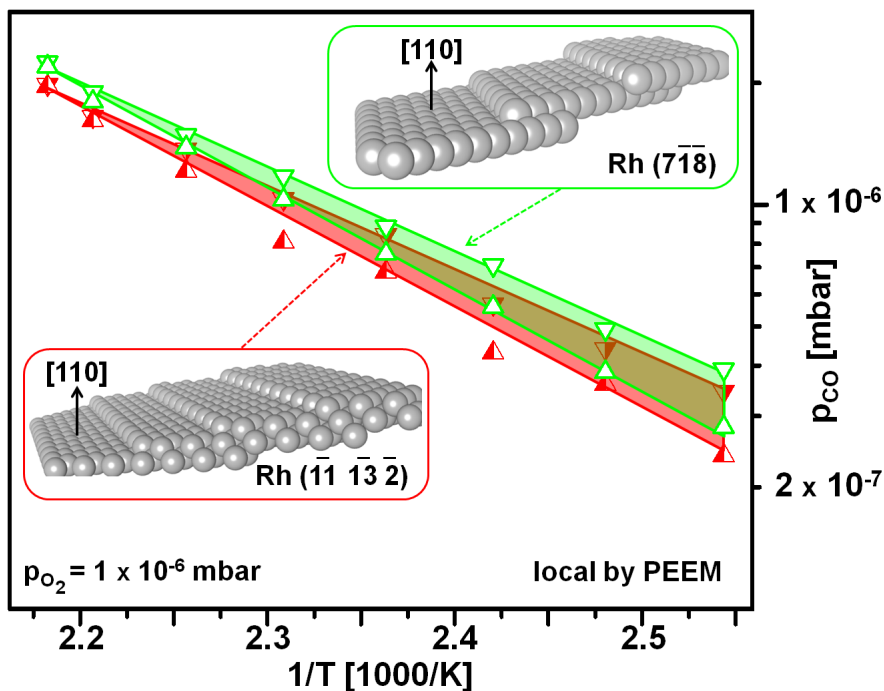


Figure 6.17: Local reaction kinetics of the CO oxidation reaction on (110)-type vicinal Rh surfaces: local kinetic phase diagram for Rh ($7\bar{1}8$) and Rh ($\bar{1}1\ \bar{1}3\ \bar{2}$) vicinal surfaces constructed at constant oxygen pressure of 1×10^{-6} mbar and in the temperature range of 393 to 458 K. Insets show ball models of stepped Rh ($7\bar{1}8$) and Rh ($\bar{1}1\ \bar{1}3\ \bar{2}$) vicinal surfaces.

Formation of subsurface oxygen could change the sticking coefficients for oxygen and CO adsorption, which influences the occurrence of the kinetic transitions τ_a and τ_b [165]. This results in the shift of diagrams for studied Rh (110)-type vicinal surfaces. The main problem in studying subsurface oxygen formation on metal surfaces is that detection of these species is a very difficult task [166]. However, some indications of subsurface oxygen formation during an ongoing catalytic reaction could be observed *in situ* by *PEEM* [167]. Indeed, formation of subsurface oxygen changes the dipole moment of the oxygen atoms adsorbed on the surface. This, in turn, reduces the value of the local work function. Due to the work function-based contrast, *PEEM* is very sensitive to such changes, namely the spatial surface region, where formation of subsurface oxygen occurs will appear bright in comparison with the regions where sub-

surface oxygen is not formed. This allows direct observation of indications of formation of subsurface oxygen species during an ongoing catalytic reaction. Such indications of subsurface oxygen formation were observed in present study during the hydrogen oxidation reaction on the same region on polycrystalline *Rh* sample, where the *CO* oxidation reaction was studied. It was observed that the collision of the reaction-diffusion fronts on the *Rh* surface during H_2 oxidation leads to the formation of a net of extended areas ("stripes") of very high *PEEM* image intensity (Fig. 6.18).

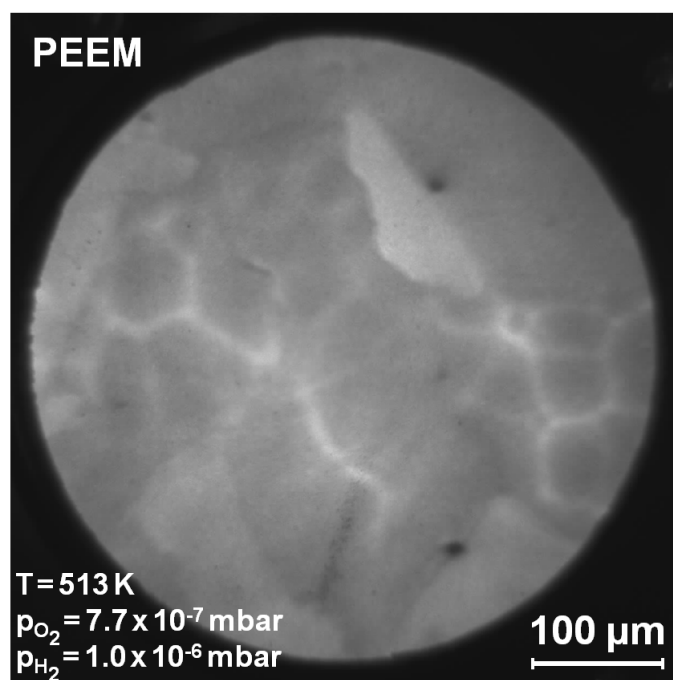


Figure 6.18: Formation of a net of bright stripes during the H_2 oxidation on the polycrystalline *Rh* surface. Bright areas are regions with reduced work function where presumably subsurface oxygen is formed.

Formation of these stripes with reduced work function was observed on the almost all domains within *PEEM* field of view. However, the stripes formed on the *Rh* (110)-type surfaces appeared as somewhat brighter than those formed on *Rh* (111)- and *Rh* (100)-type surfaces. Removing the oxygen from the reactive atmosphere leads to the disappearance of these stripes due to reduction by hydrogen. Again, the stripes on (110)-type vicinals appeared to be "longer living" than those on the rest of the surface (Fig. 6.19).

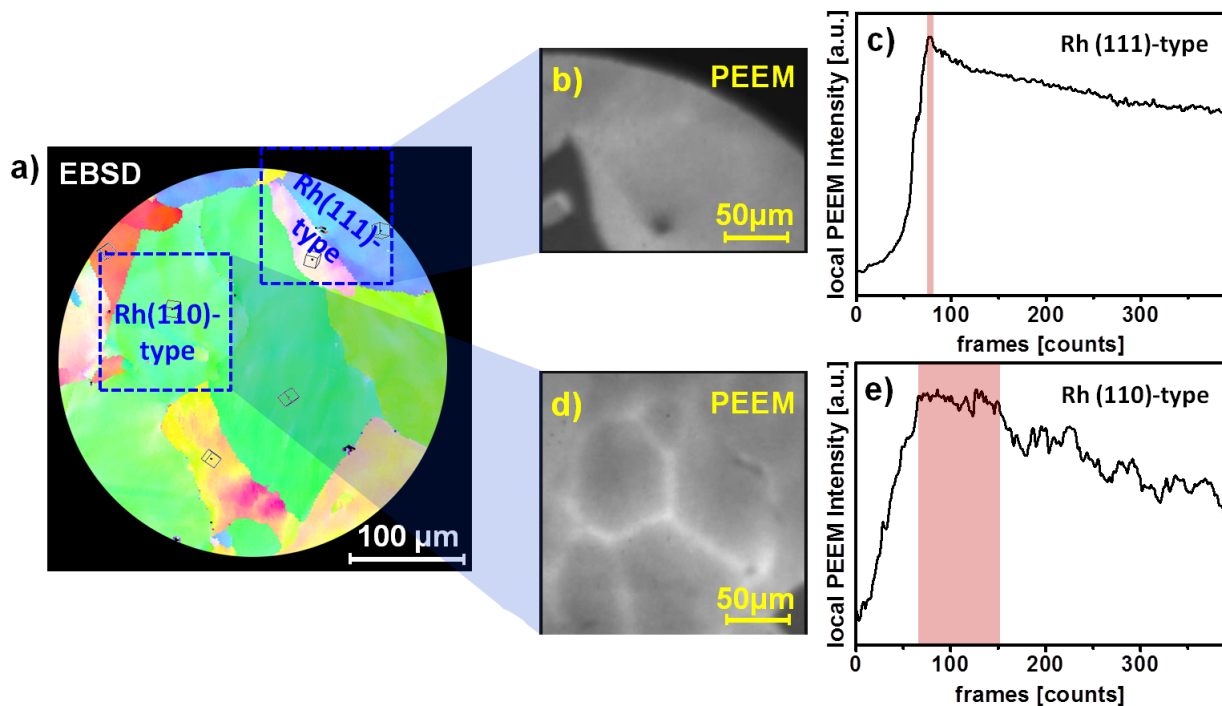


Figure 6.19: Comparison of the lifetime of regions of reduced work function for $Rh(111)$ - and $Rh(110)$ -type surfaces: **a)** *EBSD* image with marked regions on $Rh(111)$ - and $Rh(110)$ -type surfaces; **b)** *PEEM* video-frames (snapshots) of the (111)-type region with visible bright stripes of reduced work function; **c)** change of local *PEEM* intensity for the region shown in **(b)** as a function of time illustrating the lifetime of the region with the reduced work function; **d, e)** the same, as in **(b)** and **(c)** but for the (110)-type surface. The supposed existence time of subsurface oxygen is marked in **(c)** and **(e)**.

As is clearly seen from the Fig. 6.19 c and e, the existence period for supposed subsurface oxygen in (110)-type region is significantly longer than for the (111)-type region. The presence of subsurface oxygen may influence the occurrence of the kinetic transitions in CO oxidation and may also shift the kinetic phase diagram.

Summary

The global reaction kinetics of CO oxidation on polycrystalline stepped Rh surface was examined by QMS in the 10^{-6} mbar pressure range and the global kinetic phase diagram for this surface was constructed.

Based on $PEEM$ and EBS measurements, the exact crystallographic orientations of individual Rh (hkl) domains of the studied polycrystalline Rh sample were obtained. The domains, visible in the $PEEM$ field of view appeared to be stepped vicinals of the (111)-, (100)- and (110)-type.

The local (domain-specific) kinetics of CO oxidation on Rh (111)-, Rh (100)- and Rh (110)- type vicinal surfaces was studied by $PEEM$ in the 10^{-6} mbar pressure range. By analysing of local intensity of $PEEM$ video sequences which were recorded during ongoing CO oxidation reaction, the local kinetic phase diagrams for Rh (111)-, Rh (100)- and Rh (110)- type vicinal surfaces were constructed.

The comparison of local kinetic phase diagrams constructed for (111)-type vicinal Rh surfaces with different step density showed that an increase of step atoms density on these surfaces influences the catalytic performance of these surfaces, leading to an increase of tolerance of these surfaces towards CO poisoning. By performing a similar comparison for the (100)-type vicinal Rh surfaces, the same effect was observed.

In turn, the (110)-type vicinal Rh surfaces, show an opposite effect, namely the higher step density leads to a decrease of catalytic performance in the sense of tolerance to CO . This opposite trend results presumably from the facilitated formation of subsurface oxygen on (110)-type vicinal Rh surfaces due to a more open surface structure. $PEEM$ observations during H_2 oxidation on the same Rh sample fortify this suggestion: the net of bright stripes occurring on the Rh surface and associated with subsurface oxygen appears to be more intensive and more long-living in the (110)-type regions in comparison to the rest of the surface.

7 | *XPS and PEEM study of initial oxidation of polycrystalline Zr foil*

Sample preparation

The cleaning procedure

To clean the studied sample from surface contaminations, the *Zr* polycrystalline sample was subjected to sputtering with Ar^+ ions (Ar pressure 10^{-5} mbar, $E_{kin} = 1$ keV) at room temperature, followed by annealing in *UHV* in the temperature range of 973 to 1173 K. The composition and cleanness of the studied sample was controlled by *XPS*. Obtaining a clean *Zr* surface is a challenging task. The main challenge in cleaning *Zr* surfaces originates from the fact that *Zr* incorporates oxygen from the environment very easily and tends to form an oxidic layer on the surface even at *UHV* conditions. Even during the *XPS* measurements on the cleaned *Zr* sample, which are usually performed after a cleaning cycle, the oxygen from the *UHV* environment could be incorporated into the clean *Zr* sample surface and the resulting *XPS* spectrum might show presence of the *O* 1s peak. In some cases, formation of *Zr* oxide can be even detected by a shift of the *Zr* 3d peaks. Therefore, obtaining an absolutely "*oxygen-free*" *Zr* surface is hardly possible. Another difficulty in cleaning of *Zr* surface is originating from the fact that carbon, which is the most common impurity in the bulk of the *Zr* sample, segregates to the sample surface upon annealing in *UHV*. Therefore, the sample was cleaned by means of repeating " Ar^+ sputtering - annealing"

cycles until the C 1s and O 1s XPS peaks showed minimal amount of carbon and oxygen and Zr 3d high resolution spectrum showed absence of Zr oxide on the sample surface. Presence of another impurities on the Zr surface was not detected by XPS .

XPS characterization of the Zr sample surface

The XPS survey spectrum and Zr 3d high resolution spectrum of the clean Zr polycrystalline surface are presented in Fig. 7.1.

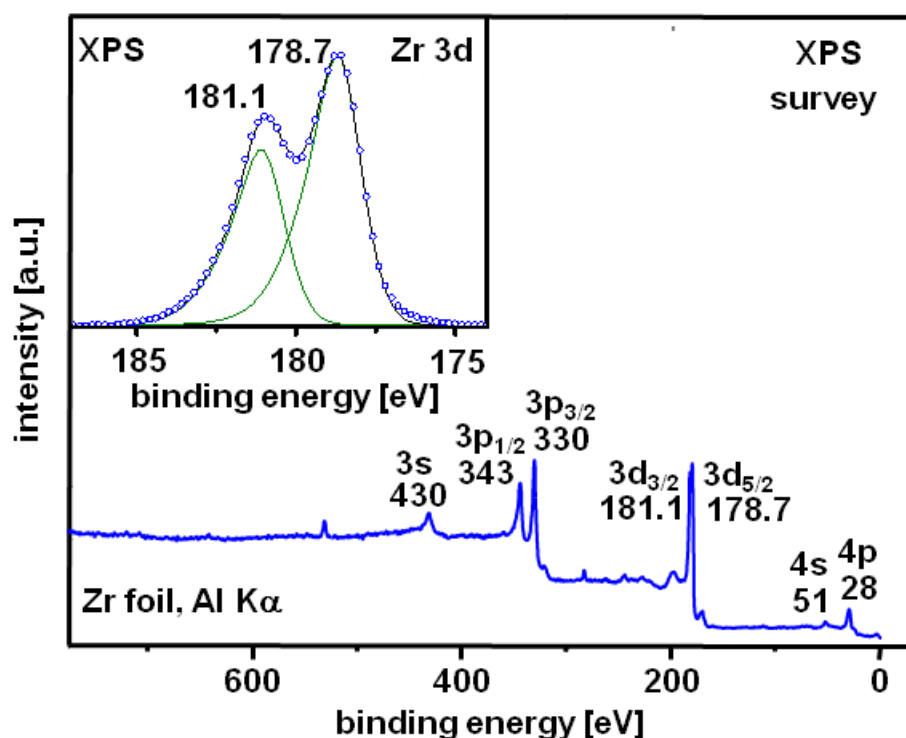


Figure 7.1: XPS survey spectrum of clean polycrystalline Zr foil. The inset shows a detailed XPS spectrum measured from the Zr 3d region.

The Zr 3d peaks were fitted using a Gaussian/Lorentzian sum function with asymmetric peak shape. The asymmetry parameters and full width at half maximum ($FWHM$) were fixed for all sets of XPS measurements which were presented in present chapter. For deconvolution of XPS spectra and subtraction of the background (Shirley), CasaXPS software package was used. For the metallic and oxidic contributions of the Zr 3d peak, $FWHM$ was 1.8 eV and 2.2 eV, respectively. The absolute values for the $3d_{5/2}$ and $3d_{3/2}$ peaks were 178.7 eV and 181.1 eV, respectively. The binding energies of the XPS peaks were calibrated in respect to the Fermi edge. The spin-orbit splitting

between $3d_{5/2}$ and $3d_{3/2}$ peaks was 2.4 eV. This values of the peaks positions and spin-orbit splitting between the peaks as well as relation between $FWHM$ for metallic and oxidic contribution of the Zr 3d high resolution spectrum are in agreement with the literature data obtained by other authors [156].

Formation of individual domains on Zr foil surface

Well-defined μm -sized Zr domains were prepared on the polycrystalline Zr surface by means of repeating cycles of Ar^+ sputtering followed by annealing in UHV at high temperature under $PEEM$ control. $PEEM$ allows direct observation of the structural transformations of the sample surface which take place in μm -range. However, due to using of the very high temperature for formation of the domains on the polycrystalline Zr surface, *in situ* observation of the domain formation process via $PEEM$ was not possible in present work. Monitoring the changes of the sample surface was performed in a "*imaging - annealing (sputtering) - imaging*" way, i.e. $PEEM$ imaging of the surface was performed just before and after each sputtering or annealing cycle. Selected $PEEM$ images, recorded after different stages of "*sputtering-annealing*" treatment of the polycrystalline Zr surface are presented in Fig. 7.2. Figure 7.2 a shows a $PEEM$ image of the polycrystalline Zr sample surface which was visualised immediately after mounting the sample into the $PEEM$ chamber. After imaging the sample, the sample was cleaned by one cycle of Ar^+ sputtering at 1 keV followed by UHV annealing at 873 K (Fig 7.2 b). Comparison of the frames a) and b) from the Fig 7.2 showed no significant change in the surface morphology. The same situation was observed after two cycles of Ar^+ sputtering at 1 keV. However, the surface morphology changes dramatically after additional cycle of UHV annealing at 973 K (Fig 7.2 d). After the "*sputtering-annealing*" treatment, the surface exhibits a well-defined structure with domains of different brightness, which, due to the relationship of the local intensity of the $PEEM$ image to the crystallographic orientation of the imaged surface, indicates their different crystallographic orientation.

Further, "*sputtering-annealing*" treatment does not change the morphology of the imaged surface significantly. The final $PEEM$ image, exhibiting well-defined domains of different orientations is presented in Fig. 7.2 f.

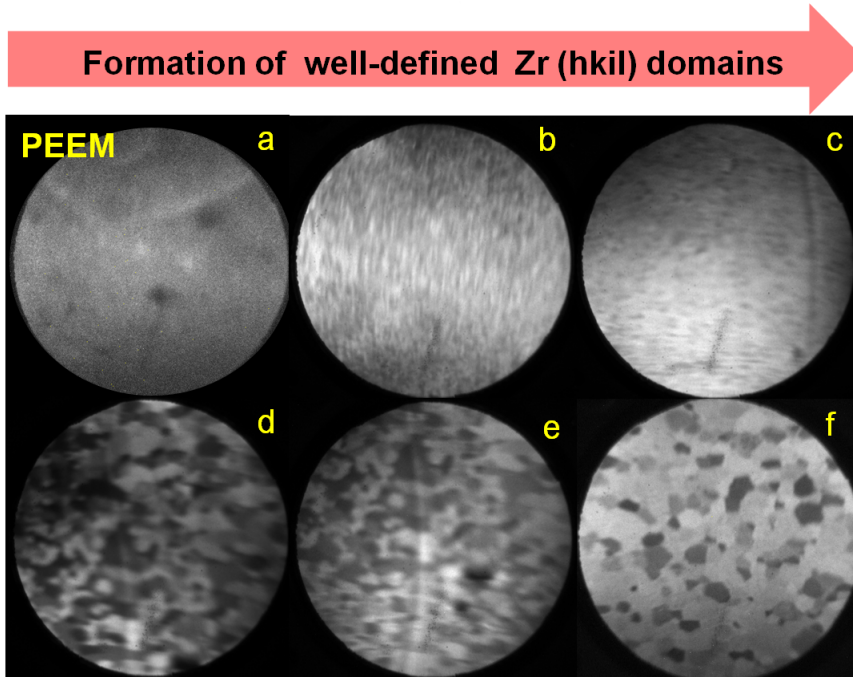


Figure 7.2: Formation of well-defined $Zr(hkil)$ domains on the polycrystalline Zr foil surface: **a)** *PEEM* image of the polycrystalline Zr sample surface after mounting the sample into the chamber; **(b-e)** change of the sample surface morphology upon the different cycles of sputtering and annealing; **f)** final *PEEM* image of the polycrystalline Zr sample surface with well-defined domains.

Phase transition hcp-bcc in Zr

The structural changes of the Zr polycrystalline sample surface due to the martensitic-like *hcp-bcc* phase transition (Fig. 7.3) in the μm -range were visualised by *PEEM*. At low temperatures, Zr exhibits a hcp crystal structure ($\alpha - Zr$), which changes to a bcc structure ($\beta - Zr$) at 1136 K in a martensitic-like phase transition (Fig. 7.3). Due to the difference in the volume filling fractions in hcp (Fig. 7.3 a) and bcc (Fig. 7.3 b) structures, i.e. increase of the atomic packing factor during the "hcp-to-bcc" phase transition [168], distortions and corrugation at both microscopic and macroscopic scales could be expected .

The set of *PEEM* images recorded after different periods of *UHV* annealing in the temperature range of "hcp-to-bcc" phase transition (1173 K) is presented in the Fig. 7.4.

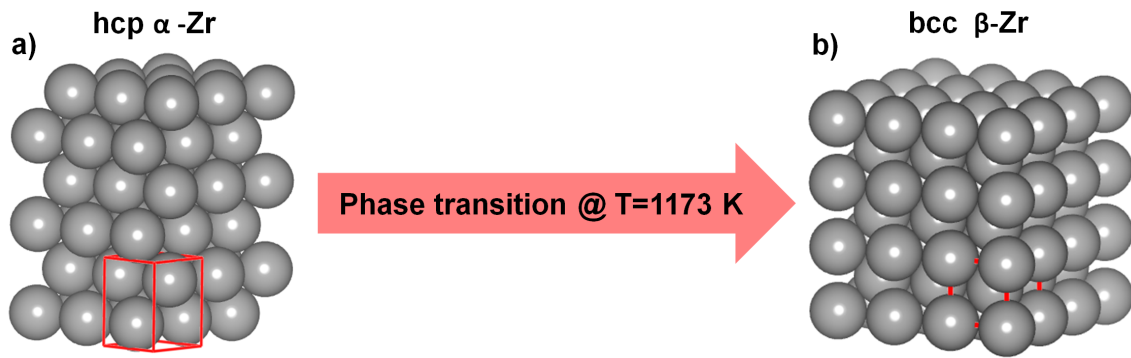


Figure 7.3: Phase transition in *Zr*. The transition "hcp-to-bcc" leads to rearrangement of the *Zr* atoms within the sample and therefore may cause changes of the morphology of the sample surface.

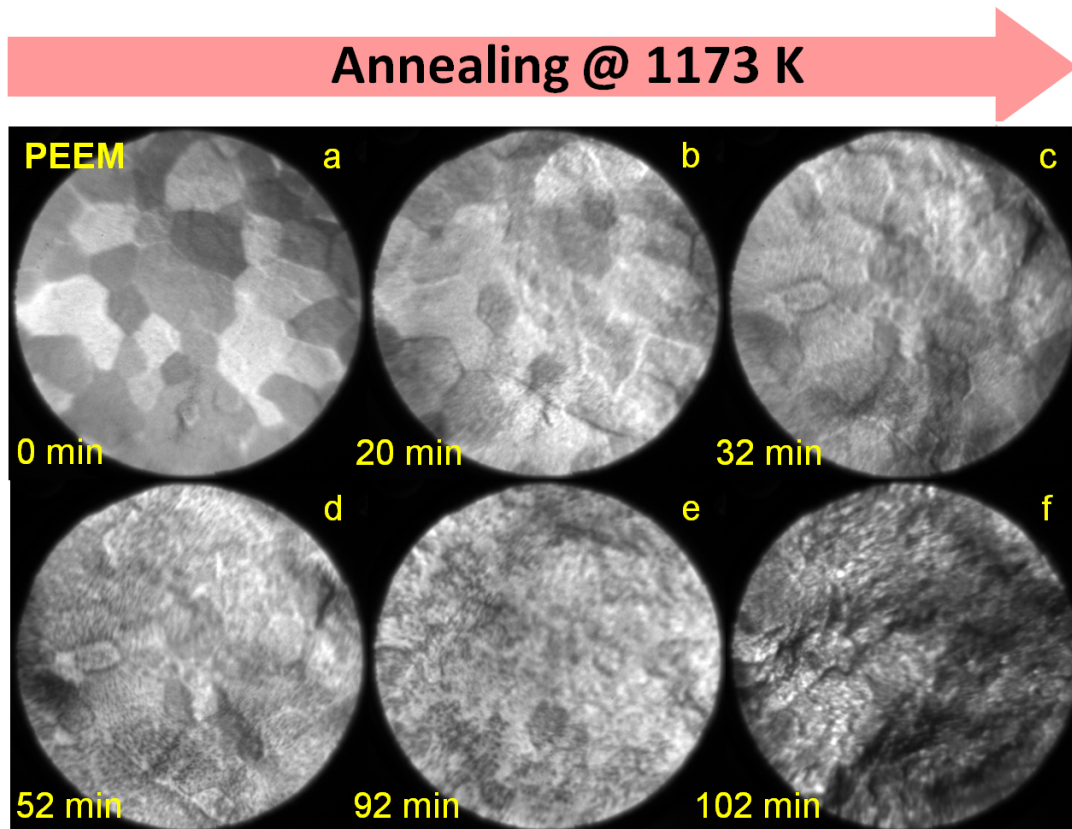


Figure 7.4: Changes of the polycrystalline *Zr* sample surface due to the "hcp-to-bcc" phase transition as imaged by *PEEM*: (a-f) *PEEM* visualization of a martensitic-like "hcp-to-bcc" phase transition in a *Zr* polycrystalline foil upon annealing in *UHV* at 1173 K. Corrugations of the initial state (a) and final state (f) differ significantly.

As was mentioned in the previous section, heating of the sample surface to the high temperatures in front of the *PEEM* during the microscope operation is hardly possible. Hence, the monitoring of the surface morphology change was performed in a

"*imaging-annealing-imaging*" way. The experiments started with a clean (sputtered, annealed and *XPS* controlled) surface. The annealing temperature during the cleaning procedure was 973 K which is lower than the expected temperature of the "hcp-to-bcc" phase transition. Comparison of the *PEEM* images recorded before and after *UHV* annealing at 973 K within one cleaning cycle did not reveal changes of the sample surface morphology.

However, annealing of the *Zr* polycrystalline surface at temperature of 1173 K initiates a martensitic-like phase transition (Fig 7.4 a, b). From the comparison of Fig. 7.4 a and 7.4 b, which were recorded immediately after cleaning of the sample (Fig. 7.4 a) and annealing at 1173 K for 20 min (Fig. 7.4 b), significant change of the surface morphology can be observed. The sample surface becomes corrugated, but individual domains are still visible. Further annealing of the sample at the same temperature leads to even more significant corrugation of the sample surface.

Cooling down the sample to the room temperature which causes reversed transition "bcc-to-hcp" did not reveal reverse change of the surface morphology: even after several hours, the surface remains in a metastable state. The stability of the surface with "new" morphology opens a possibility to investigate different chemical processes (e.g. surface oxidation) on the samples with two different morphologies (annealed at 973 K and 1173 K respectively).

Initial oxidation of polycrystalline Zr foil

Detection of substoichiometric Zr oxide species

The oxidation of polycrystalline *Zr* at low oxygen pressures was investigated by *XPS*. As was discussed in section 2.6.2, the formation of the oxide on the clean metal surface can be divided into two stages. The first, rapid oxidation stage takes place at the very beginning of the oxidation process, i.e. at a very low oxygen exposure and low oxidation temperature. At this stage, substoichiometric *Zr* oxide species could be formed. However, the amount and composition of *Zr* suboxidic species is still under debate. This stage is followed by the second, slow stage which takes place at higher oxygen exposures and higher oxide layer thickness.

In order to follow the first oxidation stage of Zr oxidation and to capture the formation of the substoichiometric ($ZrO_x, x < 2$) oxidic species, XPS measurements of the Zr polycrystalline sample after oxidation at constant temperature of 398 K and at constant oxygen pressure of 2×10^{-8} mbar were performed. The oxygen exposure was varied in the range of 4 to 51 L. The choice of this temperature was dictated by the fact that the time needed for cooling down of the sample to room temperature is much longer, than the time needed for formation of the oxide on the Zr surface even under UHV conditions.

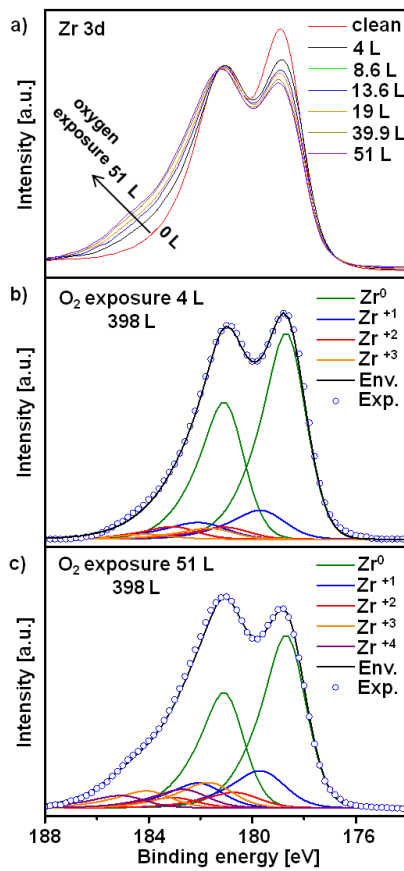


Figure 7.5: *In situ* XPS of the initial stages of Zr oxidation: **a)** a set of Zr 3d spectra at different oxygen exposures in the range 4-51 L at oxygen pressure of 2×10^{-8} mbar, and $T=398$ K; **b)** deconvolution of the spectrum taken at 4 L. Apart from metallic Zr only the suboxide contribution of Zr^{+1} , Zr^{+2} , Zr^{+3} are visible; **c)** the same, but for 51 L, the ZrO_2 contribution is clearly visible.

In turn, upon cooling down of the sample from high temperatures to 398 K, formation of the oxide on the sample surface can be decelerated.

Figure 7.5 a, b, c shows the Zr 3d XPS spectra obtained after exposure of the polycrystalline Zr sample surface in oxygen in the range of 4 to 51 L at a constant temperature of 398 K and at constant oxygen pressure of 2×10^{-8} mbar. The Zr 3d spectrum which was obtained after exposure of 4 L shows only minor contributions of suboxidic species, apart from the metallic Zr (Fig. 7.5 b). With increase of the oxygen exposure

the Zr 3d spectrum become more broader, i.e. an oxidic part starts to develop, while the contribution of the metallic part decreases (Fig. 7.5 a). At higher exposures apart from the suboxide contribution, a signal from the stoichiometric (ZrO_2) appears. The spectrum taken after exposure of 51 L of oxygen clearly shows the presence of substoichiometric ($ZrO_x, x < 2$) oxides and stoichiometric (ZrO_2) oxides.

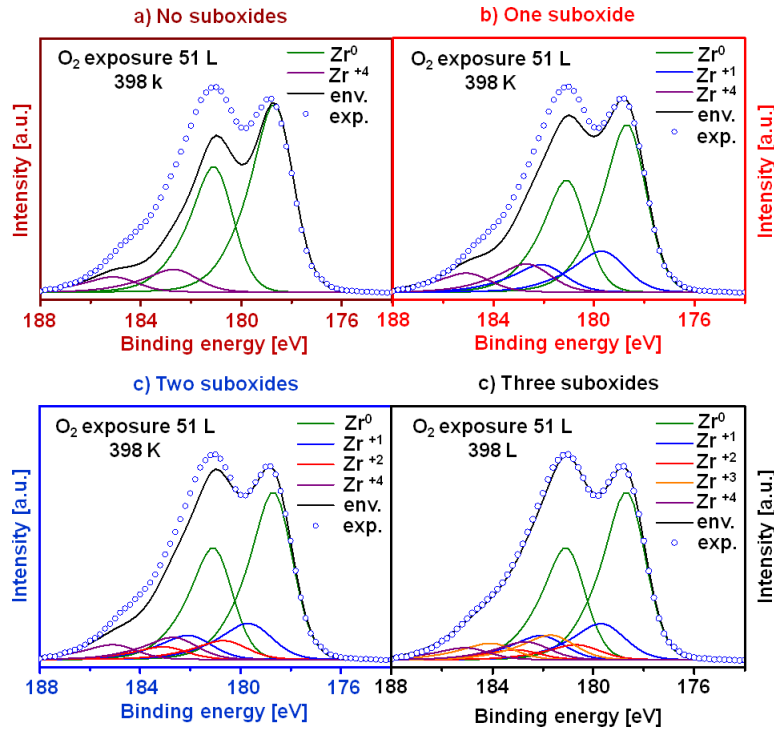


Figure 7.6: Zr 3d peaks recorded after the oxidation of the polycrystalline Zr sample at $T=398$ K of 51 L of oxygen at an oxygen pressure of 8×10^{-7} mbar. (a-d) Zr 3d peak fitted with different amount of substoichiometric oxidic species: a) The same Zr 3d peak without addition any of substoichiometric oxides. Only metallic and stoichiometric ZrO_2 are presented; b) The same Zr 3d peak, but with one substoichiometric oxidic specie (i.e Zr^{+1}); c) The same Zr 3d peak, but with two substoichiometric oxidic species (i.e Zr^{+1} and Zr^{+2}); d) The same Zr 3d peak, but with three substoichiometric oxidic species (i.e Zr^{+1} , Zr^{+2} , Zr^{+3}).

In order to prove the number of Zr suboxidic species, the Zr 3d XPS spectrum of the Zr polycrystalline sample, which was exposed to 51 L of oxygen at 398 K was fitted with different amount of the substoichiometric oxidic species. The results of the fitting are presented in Fig. 7.6. From Figure 7.6 one can clearly see that accurate fitting on the Zr 3d spectrum of the oxidized Zr polycrystalline sample could not be performed with only metallic (Zr^0) and stoichiometric oxide (ZrO_2). Moreover, obtaining of the reliable fitting is also not possible with one (Zr^{+1}) or two (Zr^{+1} and Zr^{+2}) substoicho-

metric species, which were introduced between metallic and stoichiometric oxide. The best fit was obtained only by using three substoichiometric oxides (i.e. Zr^{+1} , Zr^{+2} and Zr^{+3}) which are placed between metallic and stoichiometric oxide species.

The values of the binding energy for for all the oxidic species species, contributing the Zr 3d are shown in the Table 7.1:

Table 7.1: Values of binding energies for suboxidic species contributing to the Zr 3d region.

	$Zr\ 3d_{\frac{3}{2}}$	$Zr\ 3d_{\frac{5}{2}}$	FWHM
Zr^0	181.10 eV	178.70 eV	1.8
Zr^{+1}	182.15 eV	179.75 eV	2.2
Zr^{+2}	183.20 eV	180.80 eV	2.2
Zr^{+3}	184.25 eV	181.85 eV	2.2
Zr^{+4}	185.30 eV	182.90 eV	2.2

Effect of the temperature on initial oxidation of Zr

As was discussed before, apart from the first, rapid oxidation stage, oxide growth on the clean metallic surface contains also a second, slow oxidation stage, which follows after the fast one.

In order to follow the second oxidation stage, the clean (sputtered, annealed and *XPS* controlled) metallic polycrystalline Zr surface was exposed to a constant oxygen pressure of 8×10^{-7} mbar and constant oxygen exposure of 200 L, but at different temperatures in the range of 324 to 473 K. Each new measurement started with clean (sputtered, annealed and *XPS* controlled) Zr surface.

The selected Zr 3d *XPS* spectra of clean and oxidized polycrystalline Zr surfaces are presented in Fig 7.7. From Figure 7.7, one can clearly see that the spectra of oxidized Zr sample show presence of three substoichiometric oxidic species (i.e. Zr^{+1} , Zr^{+2} , Zr^{+3}) between the metallic (Zr^0) and the stoichiometric oxide (Zr^{+4}) species. Increase of the oxidation temperature leads to attenuation of the Zr^0 signal and increase of the Zr^{+4} signal. In turn, the amount of the substoichiometric oxidic species remains constant within the experimental error bar in investigated temperature range. Comparison of the *XPS* results for the oxidized Zr polycrystalline sample of different morphologies (i.e. smooth sample annealed at 973 K and rough sample annealed at 1173 K) did not reveal significant difference in oxidation behaviour.

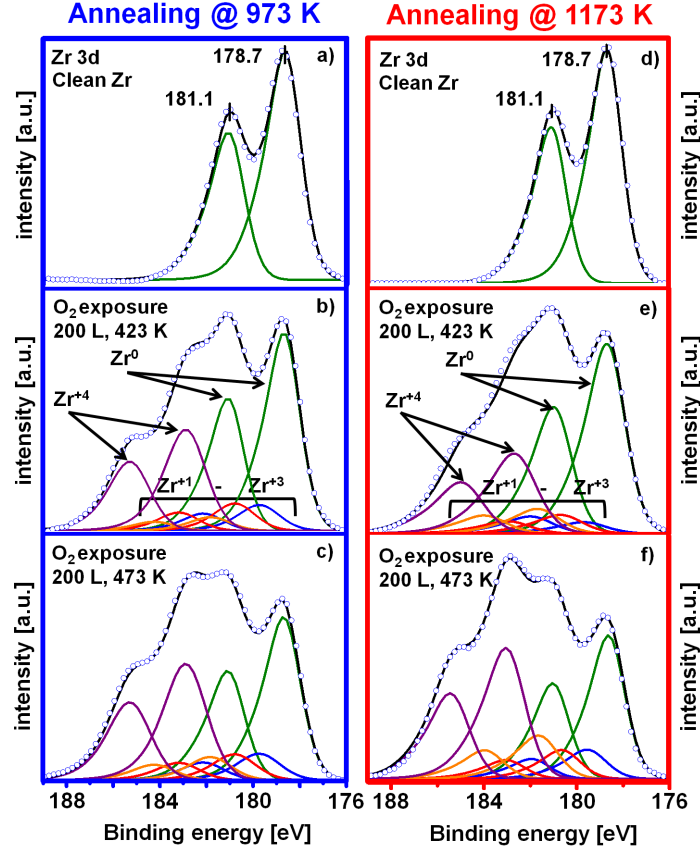


Figure 7.7: Comparison of the initial *Zr* oxidation for the samples annealed at two different temperatures: 973 K (blue rectangle) and 1173 K (red rectangle): (a, d) *Zr* 3d XPS region of the clean surface before the oxidizing oxygen treatment; (b, e) the same, but after oxidation at constant oxygen pressure of 8×10^{-7} mbar at 423 K (200 L); (c, f) the same as in (b), but at 473 K.

Usually, the XPS spectrum contains not only information about the chemical composition of the investigated sample, but also information about the thickness of the overlayer structures contributing to the sample. The thickness of the overlayer structures can be estimated from the intensity of the *Zr* 3d peak, or, more precise, from the intensity of each component contributing to the whole *Zr* 3d spectrum. Estimation of the thickness of the oxidic layer, formed on the clean metallic *Zr* polycrystalline surface was performed using a set of the equations described in the section 4.2.3. For estimation of the oxidic layer thickness, it was assumed that the *Zr* substrate is homogeneous and is covered with a uniform layer of stoichiometric oxide with an intermediate layer of substoichiometric oxide which is placed between ZrO_2 and metallic *Zr* layer (i.e. two layer model).

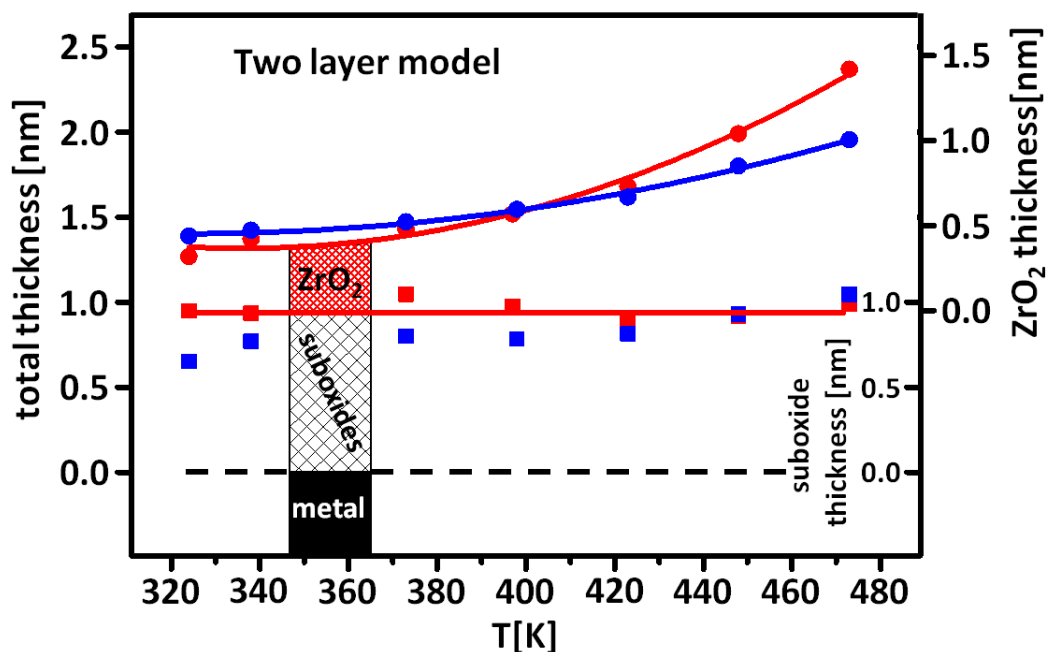


Figure 7.8: Thickness of the ZrO_x interlayer, ZrO_2 overlayer and total Zr oxide layer thickness as obtained from XPS measurements at different temperatures for samples with different morphology: blue line and blue rectangles correspond to the sample annealed at 973 K, in turn, red line and red rectangles correspond to the sample annealed at 1173 K to the Results for the 423 K and 473 K are taken from the data shown in Fig. 7.7. The inset schematically illustrates the two-layer model.

Figure 7.8 shows the thickness of stoichiometric and substoichiometric oxidic layers as a function of the oxidation temperature at constant oxygen pressure of 8×10^{-7} mbar and constant exposure of 200 L. From Figure 7.8, one can clearly see that the thickness of the suboxidic interlayer remains constant in the investigated temperature range within experimental error bar, while the stoichiometric ZrO_2 overlayer grows continuously with an increase of the oxidation temperature.

Additionally, comparison of the oxidic layer growth for the samples of different morphology did not reveal a significant difference in growth of the stoichiometric or substoichiometric oxidic layers.

***In situ* observation of initial Zr oxidation by PEEM**

In order to visualize the oxidation process *in situ*, the same oxidation procedure which was studied by XPS , was repeated in $PEEM$. The clean (sputtered, annealed and XPS controlled sample) was exposed to 200 L of oxygen at a constant temperature of

473 K and at constant pressure of 8×10^{-7} mbar. During the exposure, the oxidation process was monitored by *PEEM*. Analysis of the *PEEM* image intensity change upon oxidation was performed by integration of the intensity in a region of interest (about $480 \mu\text{m}$) within the field of view of the *PEEM*. The integrated image intensity was analyzed "frame-by-frame", and the resulting *PEEM* intensity curve is presented in the Fig. 7.9.

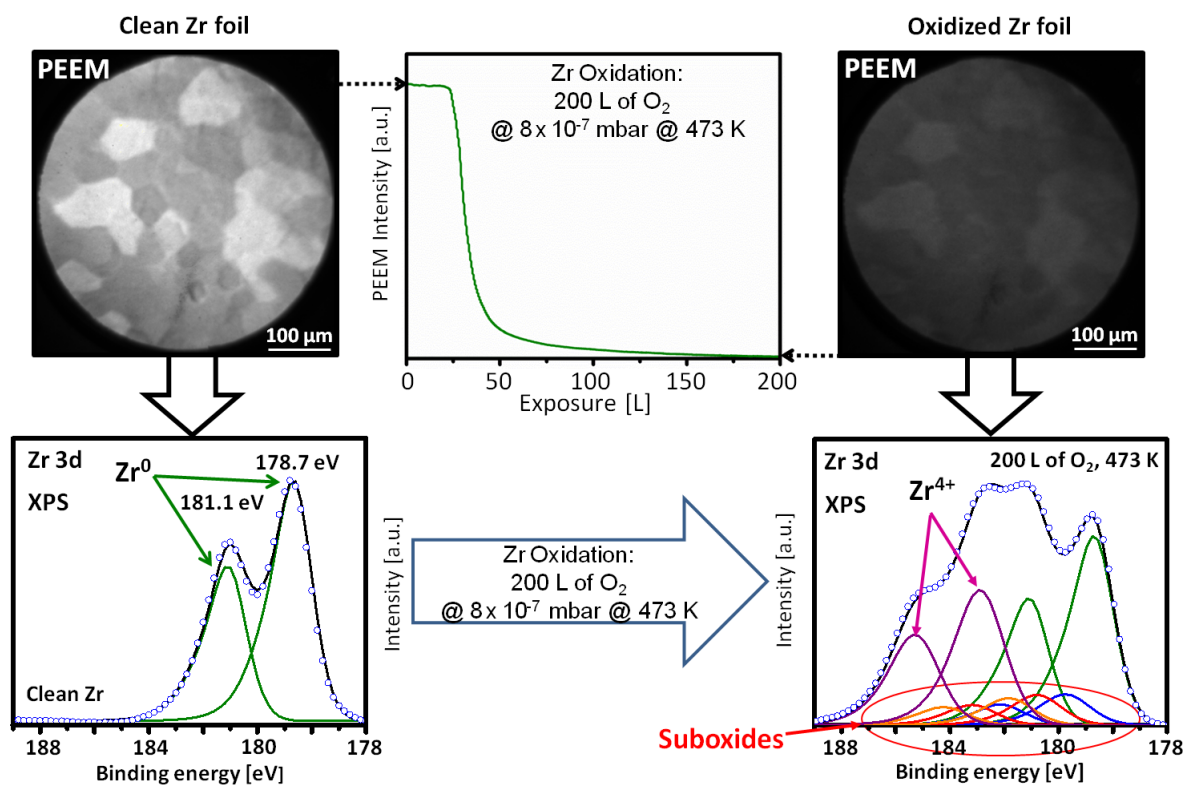


Figure 7.9: *In situ* *PEEM* observation of the oxidation of the polycrystalline *Zr* foil. The left hand inset shows the *PEEM* image of the clean *Zr* foil and corresponding XPS *Zr* 3d spectrum of the same clean *Zr* sample. The right hand inset shows the same region of interest, but after oxidation at 473 K at oxygen pressure of 8×10^{-7} mbar (oxygen exposure 200 L). The green curve in the center represents the integrated *PEEM* image intensity read out frame-by-frame.

As it is seen from Fig. 7.9, the *PEEM* intensity curve consists of two parts, whereas the first part shows rapid decrease of the local *PEEM* intensity of the image with increase of the oxygen exposure which ends at an oxygen exposure of about 40 L. The second part, in turn, shows a relatively slow decrease of the local *PEEM* intensity of the image. The existence of these two regions in the *PEEM* intensity curve is in a good agreement with the two stage oxidation process as observed in our XPS studies.

Summary

Well-defined (hkil) domains were formed on the polycrystalline *Zr* sample surface by means of repeating cycles of Ar^+ sputtering followed by annealing in *UHV*.

Initial oxidation of polycrystalline *Zr* at low pressure conditions (10^{-8} - 10^{-7} mbar) was studied by *XPS*. The *XPS* measurements revealed formation of suboxides as an interlayer between the metal surface and a stoichiometric ZrO_2 overlayer during the first stage of oxide formation on the *Zr* surface. The sole suboxide layer without contribution of any stoichiometric oxide was observed by *XPS* at oxygen exposure of about 4 L. Comparison of the oxidic layer growth during the initial oxidation of polycrystalline *Zr* for the samples of different morphology samples did not reveal a significant difference in growth of the stoichiometric or substoichiometric oxidic layers. The martensitic-like "*hcp-to-bcc*" phase transition, which is caused by heating of the *Zr* sample to about 1173 K, was visualised by *PEEM*. The *PEEM* observations revealed a significant change of the surface morphology during the phase transition. Upon cooling down of the sample to room temperature, a reverse change of morphology was not observed.

In situ PEEM studies of the initial oxidation of polycrystalline *Zr* sample performed at the same conditions as in *XPS* experiments are in accord with the two stage process of oxidation of *Zr*.

8 | *PEEM and XPS study of CO oxidation on supported Pd model catalysts*

Sample preparation

The cleaning procedure and XPS characterization of the sample

The preparation of the model system consisting of *Pd* powder supported by ZrO_x was discussed in section 3.2.1. To clean the *Pd/ZrO_x* sample surface, the sample was subjected to several cycles of sputtering with Ar^+ ions of 1 keV energy (emission current $4.5 \mu A$, *Ar* partial pressure of 6×10^{-6} mbar). To avoid alloying between *Pd* and *Zr* [169], it was reasonable to abstain from prolonged annealing in *UHV*.

The cleanness and composition of the *Pd/ZrO_x* sample was controlled by *XPS*. The survey spectrum and the high resolution *Zr* 3d, *Pd* 3d and *Zr* 3p *XPS* spectra of clean *Pd/ZrO_x* sample are shown in Fig. 8.1. Deconvolution of the *Zr* 3d *XPS* spectrum for clean *Pd/ZrO_x* was performed using fitting parameters, which are the same to those used for polycrystalline *Zr* foil in chapter 7. The values of asymmetric peak shape, peak extension asymmetry and *FWHM* are the same for $Zr\ 3d_{\frac{3}{2}}$ and $Zr\ 3d_{\frac{5}{2}}$. The *FWHM* for metallic and oxidic contributions of *Zr* 3d high resolution spectrum was 1.8 eV and 2.2 eV, respectively. The value of spin-orbital splitting for $Zr\ 3d_{\frac{3}{2}}$ and $Zr\ 3d_{\frac{5}{2}}$ was 2.4 eV, which is in agreement with literature data [156]. Carbon on *Pd/ZrO_x* sample surface was presented only in negligible amounts (Fig. 8.1). Presence of other contaminations was not observed by *XPS*.

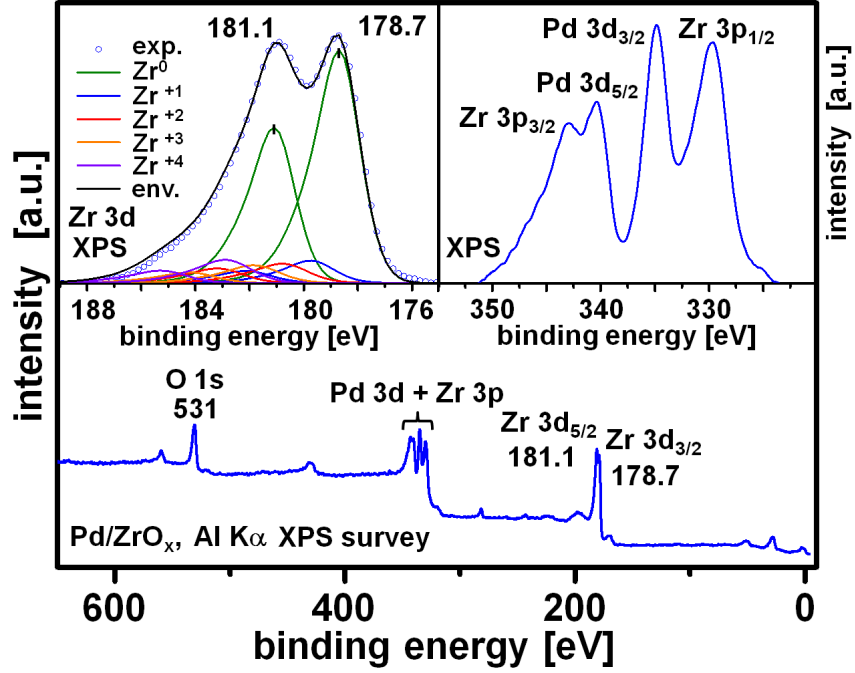


Figure 8.1: XPS survey spectrum of clean Pd/ZrO_x sample. The left and right insets show detailed XPS spectra measured from Zr 3d and Pd 3d regions, respectively.

Deconvolution of the XPS data for Zr 3d region for clean Pd/ZrO_x sample has show, as expected, not only the metallic Zr , but also suboxidic (ZrO_x , $x \leq 2$) species and stoichiometric oxide (ZrO_2) (Fig 8.1). The values of binding energies and $FWHM$ for metallic and oxidic contributions of Zr 3d high resolution spectrum are summarized in Table 8.1.

Table 8.1: Values of binding energies for metallic and oxidic contributions of the Zr 3d region of the clean Pd/ZrO_x sample. All the values are taken from the chapter 7.

	Zr $3d_{\frac{3}{2}}$	Zr $3d_{\frac{5}{2}}$	FWHM
Zr^0	181.10 eV	178.70 eV	1.8
Zr^{+1}	182.15 eV	179.75 eV	2.2
Zr^{+2}	183.20 eV	180.80 eV	2.2
Zr^{+3}	184.25 eV	181.85 eV	2.2
Zr^{+4}	185.30 eV	182.90 eV	2.2

However, for the case of the Pd 3d, difficulties in deconvolution appear, which originate from the fact that the Pd 3d overlaps with Zr 3p XPS spectrum (Fig. 8.1). Therefore, in order to answer the question about formation of Pd oxide during the cleaning procedure, the similar cleaning procedure was performed for the Pd/Pt sample consisting of μm -size Pd powder agglomerates supported by a polycrystalline Pt

foil. For the case of the *Pd/Pt* sample, *Pd* 3d do not overlap with any *XPS* peaks of *Pt* and hence reliable fitting could be obtained. The deconvoluted *Pd* 3d high resolution spectrum of the clean *Pd* agglomerates supported by *Pt* is presented in the Fig. 8.2.

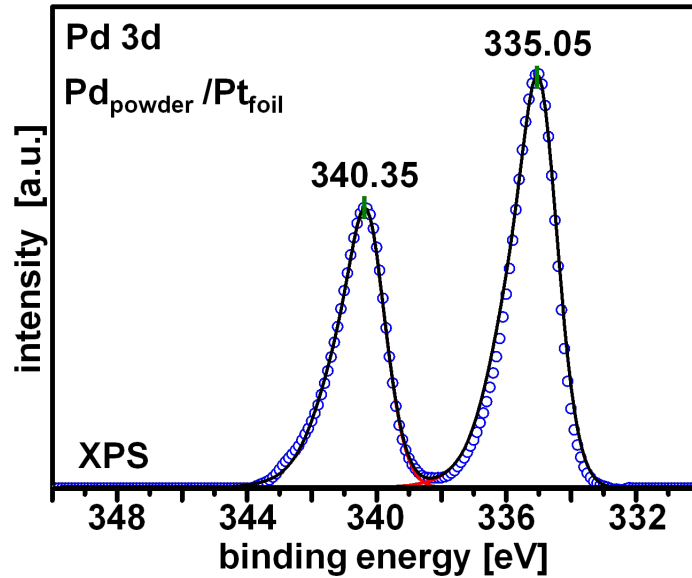


Figure 8.2: Detailed *XPS* spectrum measured from *Pd* 3d region of the *Pd/Pt* sample.

The *Pd* 3d was deconvoluted using only two *Pd* 3d_{3/2} and *Pd* 3d_{5/2} peaks corresponding to metallic *Pd*. The value of spin orbit splitting was 5.3 eV. The value of *FWHM* was 1.45 eV for both the *Pd* 3d_{3/2} and the *Pd* 3d_{5/2} peaks. The binding energies for *Pd* 3d_{3/2} and *Pd* 3d_{5/2} were 340.35 eV and 335.05 eV, respectively. The fitting parameters used for the *Pd* 3d spectrum of the *Pd/Pt* sample are in a good agreement with literature data [156]. Presence of *Pd* oxide on the *Pd/Pt* sample after the cleaning procedure was not observed. This proves that formation of *Pd* oxide on the *Pd/ZrO_x* sample after the cleaning procedure can also be neglected.

Identification of Pd and ZrO_x in PEEM

Beside the work function contrast mechanism, which was discussed in section 4.1.2, for the samples with varying roughness, such as, for example, μm -sized metal powder agglomerates supported by relatively flat polycrystalline foil, *PEEM* image also have topographical contribution to the contrast. This allows a distinguishment between the

μm -sized Pd powder agglomerates and the relatively flat ZrO_x support (Fig. 8.3.a).

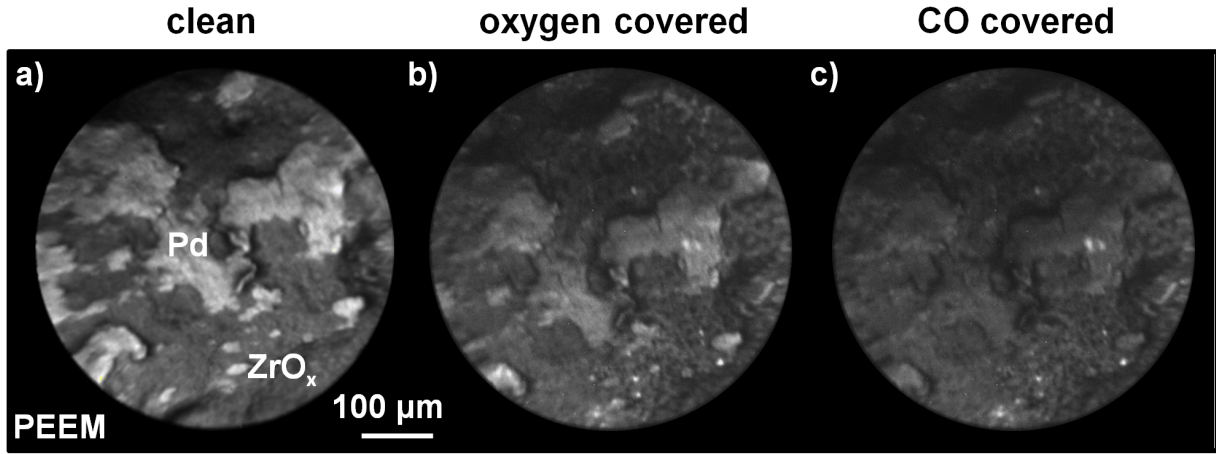


Figure 8.3: Model system Pd/ZrO_x imaged in $PEEM$: **a)** clean Pd/ZrO_x surface; **b)** the same region, but covered with oxygen; **c)** the same region, but covered with CO .

Additionally to the topographical contrast between the Pd powder agglomerates and ZrO_x , the difference in values of the work function for Pd and for ZrO_x helps to distinguish between these two materials in $PEEM$. The work function value for clean polycrystalline Pd is about 5.22 eV [170]. In turn, ZrO_2 is expected to have a photoelectric threshold of about 8.2 eV [149]. Therefore, the regions of the clean Pd/ZrO_x sample containing Pd agglomerates are expected to be significantly brighter than those of ZrO_x support. The difference in contrast between Pd powder agglomerates and ZrO_x support remains also upon oxygen and CO adsorption (Fig. 8.3. b, c). In the Table 8.2, the reference values for clean, oxygen and CO covered low Miller Pd single crystalline surfaces are presented.

Table 8.2: Values of work function for the clean, oxygen and CO covered Pd (110), Pd (100), Pd (111) surfaces.

	Clean	Oxygen	CO
$\text{Pd}(110)$	5.20 eV [171]	+0.7 eV [160]	+1.26 eV [160]
$\text{Pd}(100)$	5.65 eV [171]	not reported	+0.94 eV [160]
$\text{Pd}(111)$	5.95 eV [171]	+0.8 eV [160]	+0.98 eV [160]

From Table 8.2 one can see that adsorption of oxygen on the clean low Miller Pd surfaces leads to an increase of the work function and hence may lead to a decrease of the $PEEM$ intensity for the region of the sample covered with Pd powder agglomerates (Fig 8.2 b). Adsorption of CO on low Miller Pd surfaces causes an even bigger

decrease of the work function for *Pd* surfaces, and hence may lead to even darker *Pd* powder agglomerates in the *PEEM* image (Fig 8.2 c). As it is also seen from Figures 8.2 b, c, adsorption of oxygen and *CO* on the *ZrO_x* support leads to insignificant changes of its *PEEM* intensity.

Local reaction kinetics of CO oxidation on ZrO_x

In the present section, the local kinetic behaviour of *CO* oxidation on μm -sized *Pd* powder agglomerates supported by *ZrO_x* was studied using *PEEM*. The choice of *ZrO_x* as a supporting material is dictated by the fact that this oxide is almost not-reducible and therefore a possible effect of storage of the oxygen on the local reaction kinetics, which is typical for reducible oxides (e.g. for *CeO_x*) could be neglected. As a *ROI* on the *Pd/ZrO_x* sample surface within the *PEEM* field of view, a region of interest of $146 \times 146 \mu\text{m}^2$ size was chosen (Fig 8.4). In order to obtain information about local kinetic behaviour of the *CO* oxidation reaction within the selected *ROI*, the local *PEEM* intensity during a cyclic variation of *CO* partial pressure at constant oxygen partial pressure and constant temperature was evaluated. The inset in Figure 8.5 shows local *PEEM* intensity hysteresis as a function of *CO* partial pressure recorded at constant oxygen partial pressure of 1.3×10^{-5} mbar and at a constant temperature of 473 K.

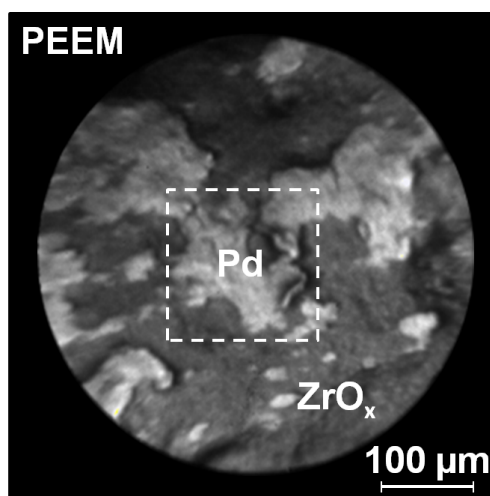


Figure 8.4: *PEEM* image of the *Pd/ZrO_x* sample surface. The white dashed rectangle corresponds to *ROI* used for local *PEEM* studies.

Similarly to the hysteresis curves corresponding to CO oxidation on polycrystalline stepped Rh surfaces presented in chapter 6, the present hysteresis curve provides information about local kinetic transitions τ_a and τ_b , namely transitions from active (oxygen covered) steady state to inactive (CO covered) steady state, but in present case for a particular spatially-confined region on the Pd/ZrO_x sample surface. In Fig 8.5 a, the $PEEM$ video-frames corresponding to the selected points on the hysteresis curve (Fig 8.5 b) are presented.

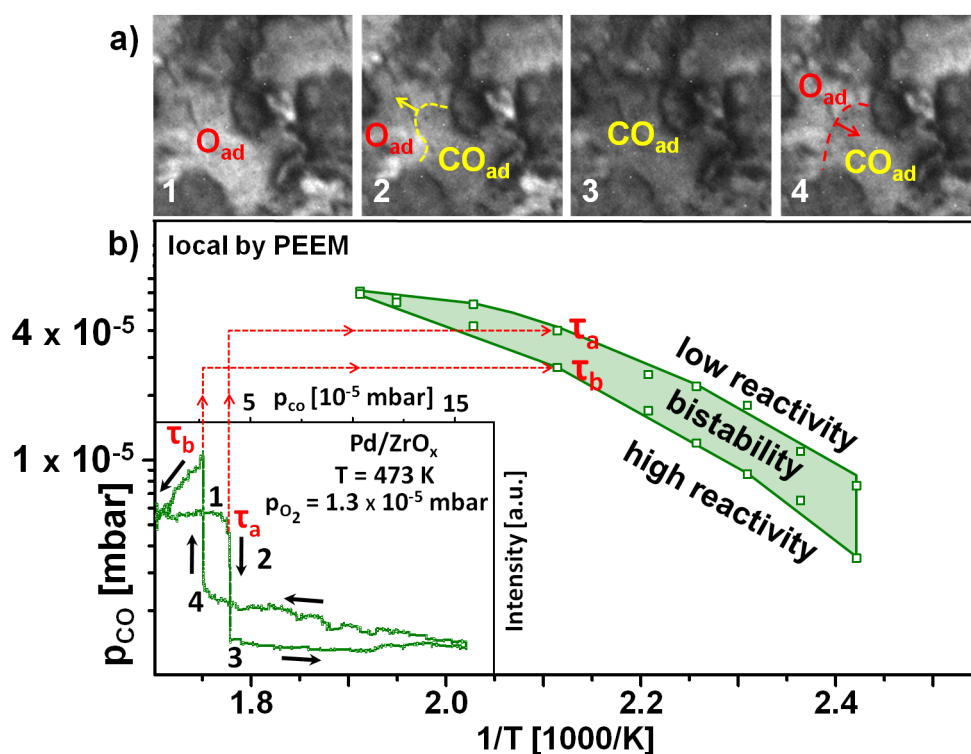


Figure 8.5: Pd/ZrO_x in the CO oxidation reaction: a) video-frames illustrating the behaviour of the region of interest during the cyclic variation of CO pressure at constant temperature of 473 K and constant oxygen pressure of 1.3×10^{-5} mbar. The dotted yellow line indicates the propagating of the CO reaction front during the kinetic transition τ_a and the dotted red line, in turn, indicates the propagating oxygen reaction front during the kinetic transition τ_b ; b) local kinetic phase diagram constructed for the constant oxygen partial pressure of 1.3×10^{-5} mbar in the temperature range of 413 to 523 K. The numbers of the frames correspond to the points on the $PEEM$ intensity hysteresis curve, which is shown in inset on the left hand side.

Frame 1 shows the surface of the Pd/ZrO_x sample covered with oxygen, i.e. residing in the active steady state. Frame 2 shows the local kinetic transition from the active (oxygen covered) steady state to the inactive (CO covered) steady state (τ_a). This local

kinetic transition is accompanied by propagation of a *CO* reaction-diffusion front along the *Pd* agglomerate surface, which leads to decrease of local image intensity and, as the result, to a "drop" in the hysteresis curve. In frame 3 the local kinetic transition from the inactive (*CO* covered) steady state to the active (oxygen covered) steady state (τ_b) is illustrated. The transition τ_b , in turn, is accompanied by propagation of a oxygen reaction-diffusion front, which leads to increase on local *PEEM* image intensity of the selected region and, as a result, to a "jump" of the local *PEEM* intensity in the hysteresis curve. In frame 4, the surface again resides in the active (oxygen covered) steady state.

By carrying out similar local kinetics measurements for the same *ROI* at constant partial oxygen pressure of 1.3×10^{-5} mbar and for different temperatures in the range of 413 to 523 K, the local kinetic phase diagram was constructed (Fig. 8.5 b). In present case, this diagram summarizes steady states of high and low reactivity and bistability state for selected $146 \times 146 \mu\text{m}^2$ size *ROI* on the *Pd/ZrO_x*.

Role of the support in the CO oxidation on Pd

Pd/ZrO_x versus Pd/Pt

In this section, the role of the oxidic support on the local reaction kinetics of *CO* oxidation on μm -sized supported *Pd* powder agglomerates was studied. In order to perform this study, the local kinetic behaviour of the *CO* oxidation reaction on the *Pd/ZrO_x*, which was presented in the previous section, was compared to those on the *Pd/Pt* sample consisting of μm -sized *Pd* powder agglomerates supported by a polycrystalline *Pt* foil. The *PEEM* images of the *Pd/ZrO_x* and the *Pd/Pt* samples are presented in Fig. 8.6. Platinum acts as a reference support in order to demonstrate an effect of the oxidic support, in present case *ZrO_x*, on the behaviour of *CO* oxidation reaction. Indeed, during the *CO* oxidation on the *Pd/Pt* sample, *Pd* powder agglomerates exhibits independent catalytic behaviour, which differs from those on polycrystalline *Pt* support.

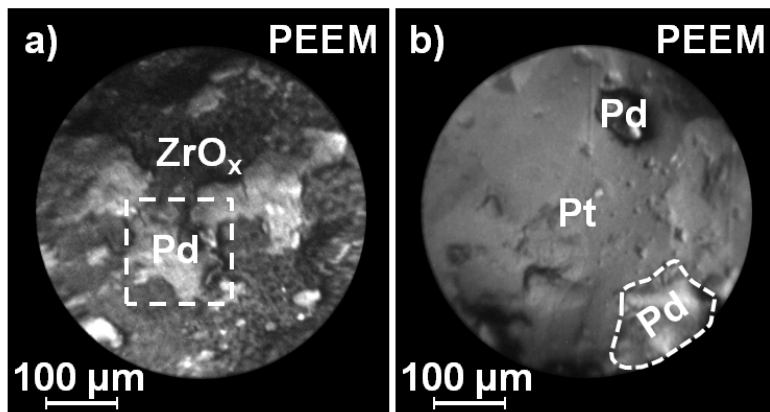


Figure 8.6: Pd/ZrO_x versus Pd/Pt : (a) *PEEM* image of the Pd agglomerates supported by ZrO_x (b) the same, but for Pd supported by Pt . White dotted lines mark regions on interest (*ROIs*) on the samples surfaces where evaluation of local *PEEM* intensity was performed.

Pd powder agglomerates on the Pd/Pt sample behaves similarly to Pd foil with artificially created steps and defects [128], thus the Pd/Pt model system could be considered in the present study as a reference, i.e. as a "quasi-unsupported" model system. For both Pd/Pt and Pd/ZrO_x information about local reaction kinetics of CO oxidation was obtained by evaluation of local *PEEM* intensity from the chosen *ROIs* (Fig. 8.6 a, b) on the samples surfaces during cyclewise variation of CO partial pressure at constant oxygen pressure and at constant temperature.

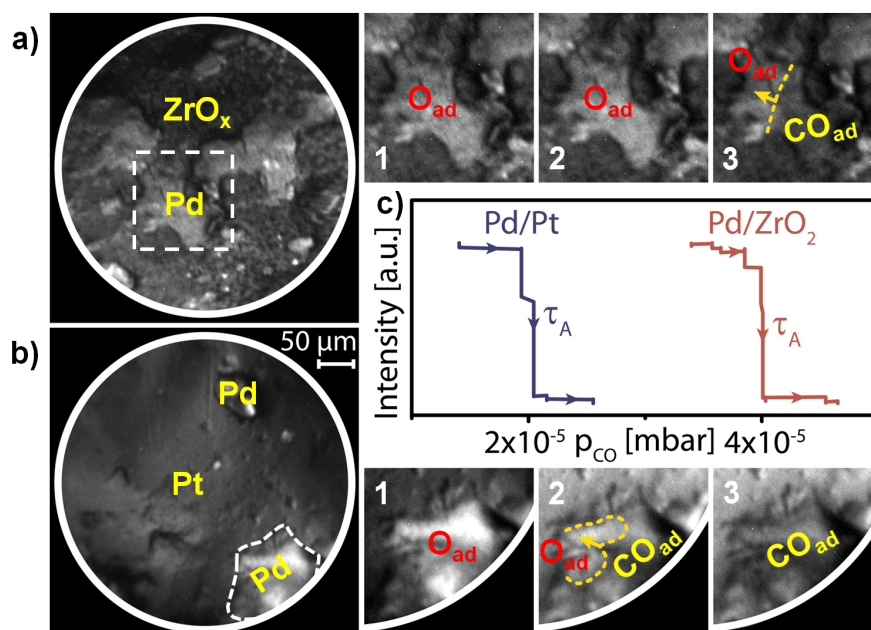


Figure 8.7: Pd/ZrO_2 and Pd/Pt samples in CO oxidation: a) the Pd/ZrO_x sample surface imaged within $PEEM$ field of view; b) the Pd/Pt sample surface imaged within $PEEM$ field of view; c) half-hysteresis curves corresponding to local kinetic transition τ_a on the Pd/ZrO_x and Pd/Pt samples. The $PEEM$ video frames in inset illustrate the behaviour of Pd/ZrO_x and Pd/Pt samples at similar values of CO pressure.

Figure 8.7 c shows the first part of the hysteresis curves, namely the part containing the transition from the active (oxygen covered) steady state to the inactive (CO covered) steady state (τ_a), taking place on Pd powder agglomerates of Pd/Pt and Pd/ZrO_x at constant oxygen partial pressure of 1.3×10^{-5} mbar and at constant temperature of 473 K.

Comparison of these two half-hysteresis curves shows that kinetic transition τ_a on Pd/ZrO_x occurs at higher CO partial pressures in comparison to the Pd/Pt sample. For the more comprehensive comparison of local reaction behaviour of Pd powder agglomerates of Pd/Pt and Pd/ZrO_x , the local kinetic phase diagrams were constructed by evaluation of local $PEEM$ intensity for the selected ROI during cyclic variation of CO partial pressure at constant oxygen pressure of 1.3×10^{-5} mbar and at constant temperature in the range of 413 to 523 K. The comparison of phase diagrams for Pd/Pt and for Pd/ZrO_x samples is presented in Fig. 8.8.

Figure. 8.8. reveals significant difference in the reaction behaviour for these two systems: the kinetic phase diagram for the oxide-supported Pd/ZrO_x sample shows remarkable shift towards higher CO partial pressure in comparison to the "quasi-

unsupported" (Pd/Pt) sample. Indeed, the kinetic transition τ_a i.e transition from active (oxygen covered) to inactive (CO covered), occurs for the oxide-supported (Pd/ZrO_x) sample at higher CO partial pressure than for the "quasi-unsupported" (Pd/Pt) sample. This indicates a higher tolerance of Pd/ZrO_x towards CO poisoning than that of the "quasi-unsupported" Pd . Also, comparison of the widths of bistability regions for oxide-supported and "quasi-unsupported" samples showed that oxidic support, significantly influences catalytic properties of Pd powder agglomerates: the bistability region of the oxide-supported Pd/ZrO_x sample is significantly wider in comparison to that for the "quasi-unsupported" Pd/Pt sample.

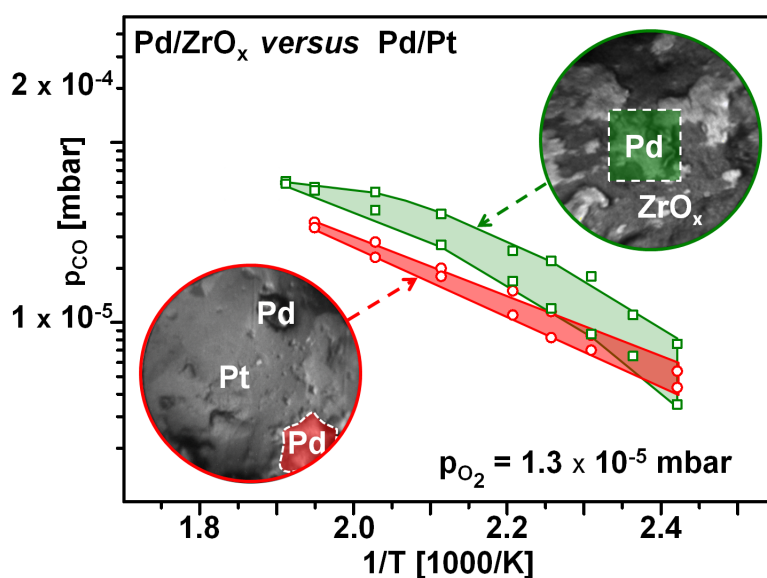


Figure 8.8: Comparison of the catalytic behaviour of the supported and "quasi-unsupported" Pd in the CO oxidation. Kinetic phase diagram for the Pd supported by ZrO_x (green) is shifted to higher CO pressures when compared to that of the "quasi-unsupported" Pd/Pt sample (red).

A possible explanation for the shift of the local kinetic phase diagram for oxide-supported *Pd* powder agglomerates in comparison to "quasi-unsupported" system can be found in metal-support boundary effects, which take place at the metal/oxide interface and can modify the binding energy of *CO* and oxygen, which results in change of adsorption properties of these species. Indeed, for the case of the $FeO_x/Pt(111)$ model system, it was shown that metal oxide interface have a significant influence on the *CO* oxidation reaction kinetics [52]. The FeO_x/Pt interface can act as a "host" for weakly adsorbed oxygen atoms, which can react with strongly bonded *CO* molecule from the *Pt*. Diffusion of oxygen from the oxide side the borderline refills the oxygen at the metal/oxide interface and next catalytic cycle can occurs. Existence of such borderline sites at the metal/oxide interface can lead to the prevention of blocking of oxygen absorption by *CO*. This can lead to change of equilibrium of competitive oxygen and *CO* adsorption, which is indicated in the shift of the kinetic phase diagram for oxide supported *Pd* sample in comparison to the "quasi-unsupported" sample.

In the present study it was shown, that a similar effect may occur on the metallic (in present case, *Pd*) site of the metal/oxide interface. The *Pd* sites bordered by ZrO_x must exhibit different binding energy for oxygen and *CO* than those in the interior of the *Pd* agglomerate surface, since the the reaction front originate from the border line. The modified energetics on the border-sites modifies the nucleation of the reaction fronts and thus the kinetics of the reaction.

Role of the Zr oxide layer thickness in the CO oxidation on ZrO_x model catalyst

Local reaction kinetics: "thin" versus "thick" oxidic support

Apart from the study of the influence of the type of the support (i.e oxidic, non-oxidic) on the local reaction behaviour of *CO* oxidation on *Pd* powder agglomerates, the influence of the thickness of the ZrO_x oxidic layer on the reaction kinetics of *CO* oxidation on oxide-supported μm -sized *Pd* agglomerates was studied. In order to study this, ZrO_x with different thickness was used as a support

In present section, two sets of *PEEM*-based experiments are presented. During the the first set of measurements, the clean (sputtered and *XPS* controlled) *Pd/Zr* sample was exposed in 2.5×10^3 L of oxygen at room temperature. After finishing the exposure, i.e *ZrO_x* formation, the *Pd/ZrO_x* sample was heated up to the desired temperature and the local measurements started.

The second set of measurements was performed at the same pressure and temperature conditions as the first set of measurements. But in this case, the sample was exposed in 35×10^3 L of oxygen at room temperature. For both sets of measurements, the local *PEEM* intensity was evaluated for the selected *ROI* during cyclic variation of *CO* partial pressure at constant oxygen partial pressure on 1.3×10^{-5} mbar and at different temperature in the range of 413 to 523 K. A comparison of the local kinetic phase diagrams, constructed at these experimental conditions for both shortly exposed and longer exposed *Pd/ZrO_x* samples is presented in Fig. 8.9. Figure 8.9 shows an effect of the oxide thickness on the catalytic performance: increase of the thickness leads to a shift of the local kinetic phase diagram towards higher *CO* partial pressures.

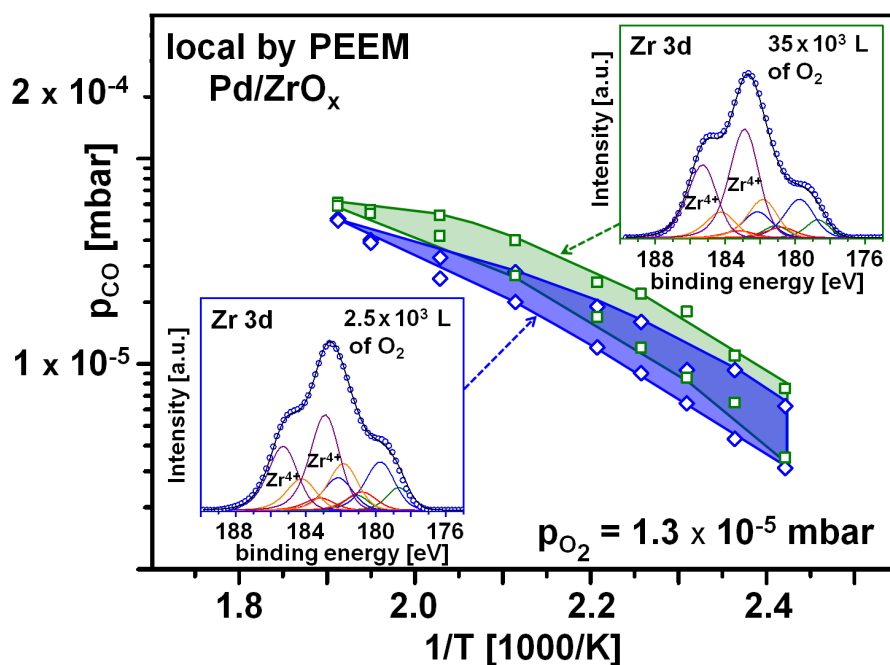


Figure 8.9: "Thin" *versus* "thick" supporting oxide in the *CO* oxidation on *Pd/ZrO_x*. Local kinetic phase diagrams correspond to *Pd/ZrO_x* with "thick" (green) and "thin" (blue) supporting oxide. *XPS* spectra in the inset show compositions of the corresponding supporting oxide layers.

In order to reveal the roots of this shift, *XPS* measurements of Pd/ZrO_x exposed in oxygen at 2.5×10^3 L and 35×10^3 L were performed. The *XPS* of differently exposed Pd/ZrO_x samples revealed formation of oxidic species, which present in higher concentration than on the cleaned Pd/ZrO_x samples which was presented in section 8.2.0. These experimental findings give reason to conclude, that additional exposure of the Pd/ZrO_x sample in oxygen (both for long and short time) leads to additional growth of the oxidic layer. In order to obtain information about the thickness of the oxidic layer grown on the Pd/ZrO_x sample surface during long and short exposure in oxygen, calculations of oxide layer thickness were performed. As a model of the oxidic layer formed on the sample surface during exposure in oxygen the "two layer" model from chapter 7 was used (Fig. 8.11 a). This model considers oxidic layer consisting of two sublayers: the upper overlayer consisting of stoichiometric oxide (ZrO_2) and the interlayer consisting of substoichiometric oxidic species (ZrO_x , $x \leq 2$), which is placed between stoichiometric oxide overlayer and metallic substrate (Fig. 8.10 a).

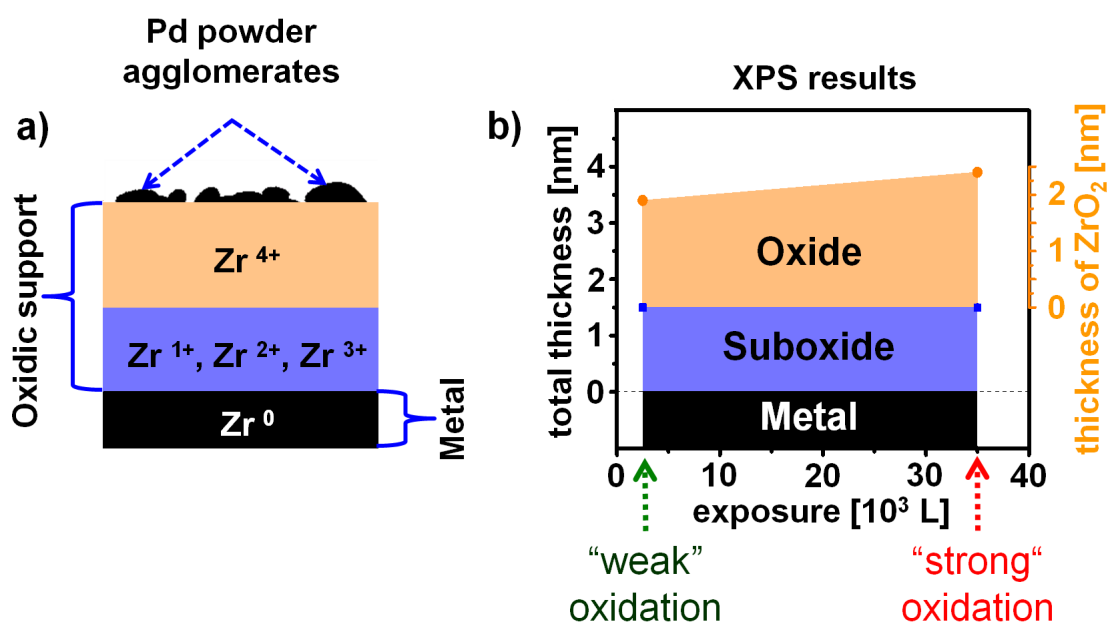


Figure 8.10: Estimation of supporting oxide layer thickness formed on the Pd/ZrO_x sample: a) two layer model of oxidic layer; b) thickness of the supporting oxide as a function of oxygen exposure.

A comparison revealed a significant difference in the thickness of the oxidic layer formed during exposure in 2.5×10^3 L and 35×10^3 L of oxygen (Fig. 8.10 b): the sample exposed in 2.5×10^3 L has thickness of stoichiometric oxide layer of 2.0 nm. The sample exposed in 35×10^3 L of oxygen has a thickness of stoichiometric oxide layer of 2.4 nm, which is 20% higher.

The possibility of formation of *Pd* oxide during the exposure in oxygen, which can also alter the catalytic behaviour of *Pd/ZrO_x*, was not considered: it is known that formation of *Pd* at low oxidation temperatures in 10^{-5} mbar is not observed.

Formation of subsurface oxygen in *Pd* can also be neglected in present study, because for the formation of subsurface oxygen species a higher temperature is necessary, that is the temperature used in the present study [165]. In addition, the regions of the sample in *PEEM* where subsurface species are formed appear to be significantly brighter than regions where no subsurface species is formed. In the present study such kind of phenomena, namely formation of regions of reduced work function during *CO* oxidation on *Pd* were not observed by *PEEM*.

Present data shows, that the thickness of the supporting oxidic layer, apparently modifies the catalytic behaviour of the *Pd/ZrO_x* model catalyst. Apparently, increase of oxide layer thickness on the support increases the effect of the metal/oxide interface on the adsorption properties of oxygen and *CO*, which results in a shift of the kinetic phase diagram.

Summary

Local reaction kinetics of the CO oxidation reaction on μm -sized Pd powder agglomerates supported by ZrO_x was investigated by $PEEM$ in 10^{-5} mbar pressure range. Based on the analysis of local $PEEM$ intensity extracted from the video-frames recorded during the ongoing CO oxidation reaction, the hysteresis curves were measured at cyclewise varying on CO pressure at constant oxygen pressure and constant temperature. From the measured data, a kinetic phase diagram for the Pd/ZrO_x model system was constructed for constant oxygen pressure of 1.3×10^{-5} mbar in the temperature range of 413 to 523 K. For comparison, the same diagram was constructed for similar Pd agglomerates supported by Pt foil, under identical conditions

The comparison of the local kinetic phase diagrams constructed for Pd/ZrO_x and for Pd/Pt revealed significant differences in the reaction behaviour of these two model systems: the Pd/ZrO_x sample exhibits significantly higher tolerance towards CO poisoning than the Pd/Pt sample. This effect could be explained by the influence of the metal/oxide interface on the adsorption properties of CO and oxygen: modified energetics of the CO and oxygen adsorption on the interface modifies the kinetics of the reaction.

To study the influence of the thickness of supporting oxidic layer on the catalytic properties of Pd , Pd agglomerates supported by Zr were exposed to 2.5×10^3 L and 35×10^3 L of oxygen at room temperature creating thus the ZrO_x model system with different thicknesses of the supporting oxide layer. Using XPS , the thickness of the supporting oxidic layer was determined and differences in the catalytic behaviour of Pd/ZrO_x with different oxide layer thickness was observed. Pd supported by thicker oxide layer showed higher tolerance towards the CO poisoning than that the thinner one.

9 | *Conclusions*

In the present thesis, *CO* oxidation on transition metal surfaces (stepped *Rh* surfaces and supported μm -sized *Pd* powder agglomerates) and initial oxidation of polycrystalline *Zr* surfaces was studied experimentally using *PEEM* and *XPS* techniques.

For the case of *CO* oxidation on stepped *Rh* surfaces, the reaction was studied on the μm -sized differently oriented grains of a polycrystalline *Rh* foil. Using *PEEM*, the *kinetics by imaging approach* was applied, where the kinetic information results from the analysis of the *in situ* recorded *PEEM* video-files. By analysis of the *PEEM* video data, the local kinetic phase diagrams for (111)-, (100)- and (110)-type vicinal *Rh* surfaces were constructed at constant oxygen pressure of 1×10^{-6} mbar and temperature in the range of 393 to 458 K. Analysis of experimental data revealed correlation between the density of steps and the catalytic performance for studied (111)-, (100)- and (110)- type vicinal *Rh* surfaces. For the case of (111)- and (100)- type vicinal *Rh* surfaces increase of steps density leads to an increase of the tolerance of these surfaces towards *CO* poisoning. For the case of (110)-type *Rh* surfaces the opposite correlation was established: an increase of density of steps on (110)-type stepped *Rh* surfaces leads to a decrease of the catalytic performance of these surfaces. It was proposed, that the reason of this "opposite" catalytic behaviour lies in the formation of subsurface oxygen on (110)-type *Rh* surfaces. This suggestion was supported by experiments with the propagation of hydrogen fronts in the H_2 oxidation: regions of subsurface oxygen formation were visualised in this way, whereas the regions of the (110)-type appeared to be more preferable for the subsurface oxygen formation.

For the study of *CO* oxidation on the *Pd* powder agglomerates supported by ZrO_x , the same approach as for stepped *Rh* surfaces, but at a constant oxygen pressure of 1.3×10^{-5} mbar and a different temperature in the range of 413 to 523 K was used.

In order to reveal the effect of the oxidic support (in present case, ZrO_x) on the reaction behaviour of CO oxidation on Pd powder agglomerates, catalytic performance of Pd powder agglomerates similar to those in the Pd/ZrO_x system but supported by Pt foil was studied. A comparison of the catalytic behaviour of Pd/ZrO_x and Pd/Pt systems revealed significant differences in the catalytic reactivity: Pd/ZrO_x model system exhibits significantly higher tolerance towards CO poisoning than the Pd/Pt model system, manifested by a corresponding shift of the kinetic phase diagram. The reason of effect of supporting oxide on the catalytic behaviour of Pd can be found in the modified binding energies of CO and oxygen on the metal/oxide interface.

To clarify the details of the support effect, the influence of the supporting layer thickness on local reaction kinetics of CO oxidation on Pd was investigated. The thickness of ZrO_x layer was varied by variation of exposure of the Pd/ZrO_x system to oxygen at room temperature. The comparison of the catalytic behaviour of the Pd/ZrO_x model system with supporting layer of different thicknesses revealed that an increase of the oxide layer thickness leads to a shift of the kinetic phase diagram towards higher CO partial pressure, which correspond to the increase of the tolerance of the studied system to the CO poisoning.

Apart from the CO oxidation reaction, the initial oxidation of Zr at oxygen pressures of 10^{-8} - 10^{-7} mbar was studied by XPS and $PEEM$. The study detected formation of three suboxidic species (Zr^{+1} , Zr^{+2} and Zr^{+3}) as an interlayer between the metal substrate and the stoichiometric (ZrO_2) overlayer. At the very beginning of oxygen exposure (≤ 4 L) a sole suboxidic layer was observed in XPS . A two stage oxidation process could be established on the basis of the XPS data: first (fast) stage with suboxide formation and second (slow) stage where ZrO_2 is formed. Additionally, *in situ* $PEEM$ observations of initial oxidation of Zr were performed at the same oxidation conditions as in the XPS . The $PEEM$ studies were in accord with the the XPS data and with the two stage model of Zr oxidation.

Present experimental data confirms the ability of the *kinetics by imaging approach* to provide the spatially-resolved information on μm -scale about the reaction kinetics for heterogeneous surfaces, such as Pd supported by ZrO_x or Pt . In the case of Pd/Pt model system also the component-resolved study of the reaction kinetics was possible.

A combination of *PEEM* and *XPS* allows an *in situ* control of the chemical composition of the model systems and provides important data, such as thickness of the supporting oxidic layer and spatial distribution of its components.

List of Figures

1.1	Schematic illustration of Three Way Catalytic Converter	3
1.2	Schematic presentation of the complexity axis in present studies of the <i>CO</i> oxidation reaction.	6
2.1	Energy diagram of the <i>CO</i> oxidation on <i>Pt</i> group metals	14
2.2	Schematical representation of different processes which occur during the thermal oxidation of metals.	15
2.3	Structure of different <i>Rh</i> surfaces.	17
2.4	The ball model of the stepped <i>Rh</i> (755) surface.	18
2.5	A <i>Rh</i> (755) stepped surface with marked orientation of a terrace and of a step.	18
2.6	Blyholder model of <i>CO</i> adsorption on <i>Pt</i> group metal surfaces.	19
2.7	The oxygen desorption spectrum for <i>Rh</i> (100) single crystalline surface.	21
2.8	The oxygen desorption spectrum for <i>Rh</i> (110) single crystalline surface.	21
2.9	Schematic representation of surface diffusion of the adsorbed molecule in one-dimensional case.	22
2.10	Schematic representation of the Langmuir-Hinshelwood mechanism for the <i>CO</i> oxidation on transition metal surfaces.	26
2.11	Schema of the global (spatially averaged) <i>CO</i> ₂ production rate hysteresis curve.	28
2.12	Schema of construction of a kinetic phase diagram.	29
2.13	Chemical shift (schematically) of <i>Zr</i> 3 <i>d</i> peak due to the oxidation or reduction of the <i>Zr</i>	33
3.1	<i>UHV</i> experimental setup.	37

3.2	The samples used in the experiments.	38
3.3	The view on the manipulator inside the <i>PEEM</i> chamber.	39
3.4	The view inside the <i>XPS</i> chamber.	40
3.5	The front view of the load lock.	41
3.6	The view to the sample fixed on the transfer rod inside the <i>XPS</i> chamber.	41
3.7	Schema of removing impurities from the sample surface by means of the Ar^+ ions sputtering.	42
3.8	Annealing of the sample in <i>UHV</i>	43
3.9	Heating of the sample in reactive gas atmosphere.	44
4.1	Schema of the photoelectric effect.	46
4.2	Schema of the photoemission spectrum.	46
4.3	Formation of the image contrast in a <i>PEEM</i>	48
4.4	Schema of the <i>UV-PEEM</i>	49
4.5	Twin anode X-ray source.	51
4.6	Schema of a hemispherical analyser.	52
4.7	Schematic representation of the measurement of the photoelectron kinetic energy in <i>XPS</i>	53
4.8	The X-ray photoelectron spectra of a <i>Zr</i> polycrystalline foil obtained using $AlK\alpha$ radiation.	54
4.9	Universal IMFP curve.	57
4.10	Illustration of collection of the photoelectrons under the different collection angle Θ	58
4.11	Schema of the multilayer system, consisting of two overlayers and a substrate.	58
4.12	Mass spectrum recorded during ongoing <i>CO</i> oxidation on transition metal surfaces.	60
4.13	Schema of a quadrupole mass spectrometer.	61
4.14	Schema of the <i>EBSD</i> experiment.	62
4.15	An example of <i>EBSD</i> image of polycrystalline <i>Pd</i> sample.	63
5.1	Illustration of the basic idea of the <i>reaction kinetics by imaging</i>	64
5.2	Experimental realization of the reaction kinetics by imaging.	66

6.1	<i>PEEM</i> field of view showing the polycrystalline <i>Rh</i> surface.	68
6.2	Contrast in <i>PEEM</i>	68
6.3	<i>PEEM</i> versus <i>EBSD</i>	69
6.4	<i>XPS</i> survey spectrum of the clean polycrystalline <i>Rh</i> foil.	70
6.5	Global reaction kinetics of <i>CO</i> oxidation on a stepped polycrystalline <i>Rh</i> surface.	71
6.6	<i>Rh</i> ($\bar{1}\bar{4}2$) surface.	73
6.7	Local reaction kinetics of <i>CO</i> oxidation on an individual <i>Rh</i> ($\bar{1}\bar{4}2$) domain.	74
6.8	<i>Rh</i> ($4\bar{4}2\bar{1}7$) surface.	75
6.9	Local reaction kinetics of <i>CO</i> oxidation on an individual <i>Rh</i> ($4\bar{4}2\bar{1}7$) domain.	76
6.10	<i>Rh</i> ($7\bar{1}\bar{8}$) surface.	77
6.11	Local reaction kinetics of <i>CO</i> oxidation on an individual <i>Rh</i> ($7\bar{1}\bar{8}$) domain.	78
6.12	<i>Rh</i> ($\bar{1}\bar{4}2$) and <i>Rh</i> (342) surfaces, both vicinal to <i>Rh</i> (111)	79
6.13	Comparison of the local kinetic phase diagrams for <i>Rh</i> ($\bar{1}\bar{4}2$) and <i>Rh</i> (342) surfaces constructed at constant oxygen pressure of 1×10^{-6} mbar and in the temperature range of 393 to 458 K.	80
6.14	<i>Rh</i> ($4\bar{4}2\bar{1}7$) and <i>Rh</i> ($\bar{3}\bar{1}24$) surfaces, vicinal to <i>Rh</i> (100)	81
6.15	Comparison of the local kinetic phase diagrams for <i>Rh</i> ($4\bar{4}2\bar{1}7$) and for <i>Rh</i> ($\bar{3}\bar{1}24$) surfaces constructed at a constant oxygen pressure of 1×10^{-6} mbar and in the temperature range of 393 to 458 K	82
6.16	<i>Rh</i> ($7\bar{1}\bar{8}$) and <i>Rh</i> ($\bar{1}\bar{1}\bar{1}\bar{3}\bar{2}$) surfaces, vicinal to <i>Rh</i> (110).	83
6.17	Local reaction kinetics of the <i>CO</i> oxidation reaction on (110)-type vicinal <i>Rh</i> surfaces: local kinetic phase diagram for <i>Rh</i> ($7\bar{1}\bar{8}$) and <i>Rh</i> ($\bar{1}\bar{1}\bar{1}\bar{3}\bar{2}$) vicinal surfaces constructed at constant oxygen pressure of 1×10^{-6} mbar and in the temperature range of 393 to 458 K.	84
6.18	Formation of a net of bright stripes during the H_2 oxidation on the polycrystalline <i>Rh</i> surface.	85
6.19	Comparison of the lifetime of regions of reduced work function for <i>Rh</i> (111)- and <i>Rh</i> (110)-type surfaces.	86
7.1	<i>XPS</i> survey spectrum of the clean polycrystalline <i>Zr</i> foil.	89

7.2	Formation of well-defined $Zr(hkil)$ domains on the polycrystalline Zr foil surface.	91
7.3	Phase transition in Zr	92
7.4	Changes of the polycrystalline Zr sample surface due to the "hcp-to-bcc" phase transition as imaged by <i>PEEM</i>	92
7.5	<i>In situ</i> XPS of the initial stages of Zr oxidation.	94
7.6	Zr 3d peaks recorded after the exposure of the polycrystalline Zr sample at $T=398$ K of 51 L of oxygen at an oxygen pressure of 8×10^{-7} mbar.	95
7.7	Comparison of the initial Zr oxidation for the samples annealed at two different temperatures.	97
7.8	Thickness of the ZrO_x interlayer, ZrO_2 overlayer and total Zr oxide layer thickness as obtained from XPS measurements at different temperatures for samples with different morphology.	98
7.9	<i>In situ</i> <i>PEEM</i> observation of the oxidation of the polycrystalline Zr foil.	99
8.1	XPS survey spectrum of clean Pd/ZrO_x sample.	102
8.2	Detailed XPS spectrum measured from Pd 3d region of the Pd/Pt sample.	103
8.3	Model system Pd/ZrO_x imaged in <i>PEEM</i>	104
8.4	<i>PEEM</i> image of the Pd/ZrO_x sample surface.	105
8.5	Pd/ZrO_x in the CO oxidation reaction.	106
8.6	Pd/ZrO_x versus Pd/Pt	108
8.7	Pd/ZrO_x and Pd/Pt samples in CO oxidation.	109
8.8	Comparison of the catalytic behaviour of the supported and "quasi-unsupported" Pd in the CO oxidation.	110
8.9	"Thin" versus "thick" supporting oxide in the CO oxidation on Pd/ZrO_x	112
8.10	Estimation of supporting oxide layer thickness formed on the Pd/ZrO_x sample.	113

List of Tables

6.1	Values of work function for the clean, oxygen and <i>CO</i> covered <i>Rh</i> (110), <i>Rh</i> (100), <i>Rh</i> (111) surfaces.	68
7.1	Values of binding energies for suboxidic species contributing to the <i>Zr</i> 3d region.	96
8.1	Values of binding energies for metallic and oxidic contributions of the <i>Zr</i> 3d region of the clean <i>Pd/ZrO_x</i> sample.	102
8.2	Values of work function for the clean, oxygen and CO covered <i>Pd</i> (110), <i>Pd</i> (100), <i>Pd</i> (111) surfaces.	104

References

- [1] P. E. MCGOVERN, J. ZHANG, J. TANG, Z. ZHANG, G. R. HALL, R. A. MOREAU, A. NUÑEZ, E. D. BUTRYM, M. P. RICHARDS, C.-S. WANG, G. CHENG, Z. ZHAO, C. WANG, *Proc. Natl. Acad. Sci. U S A*, **101**, 17593 (2004).
- [2] T. HUSEMANN, "*Cordus, Valerius*", *Allgemeine Deutsche Biographie (ADB)* (in German), Leipzig: Duncker and Humblot (1876).
- [3] H. DAVY, *Philos. Trans. A Math. Phys. Eng. Sci.* **106**, 1 (1816).
- [4] D. KNIGHT, *Humphry Davy: Science and Power*, Cambridge, Cambridge University Press (1992).
- [5] J. K. LAYLIN, *Nobel Laureates in Chemistry 1901-1992 (History of Modern Chemical Sciences)*, Amer. Chem. Soc., Wash. (1993).
- [6] G. ERTL, *Angew. Chem. Int. Ed.* **47**, 3524 (2008).
- [7] V. SMIL *Enriching the earth: Fritz Haber, Carl Bosch, and the transformation of world food production*, Cambridge, Mass.: MIT (2004).
- [8] F. HABER, *Z. Elektrochem.* **16**, 244 (1910).
- [9] F. HABER, R. LE ROSSIGNOL, *Z. Elektrochem.* **19**, 53 (1913).
- [10] J. W. ERISMAN, M. A. SUTTON, J. GALLOWAY, Z. KLIMONT, W. WINWARTER, *Nat. Geosci.* **1**, 636 (2008).
- [11] W. APPL, *Ammonia*, Wiley-VCH, Weinheim (1999).

- [12] Z. MA, F. ZAERA, *Heterogeneous Catalysis by Metals. Encyclopedia of Inorganic Chemistry* (2006).
- [13] <http://www.grandviewresearch.com/press-release/catalyst-market-analysis>, 15.04.2016.
- [14] H. J. GARY, G. E. HANDWERK, *Petroleum Refining: Technology and Economics* (4th ed.), CRC Press (2001).
- [15] J. G. SPEIGHT, *The Chemistry and Technology of Petroleum* (4th ed.), CRC Press (2006).
- [16] E.J. HOUDRY, US Patent 2674521 *Catalytic converter for exhaust gases* (1954).
- [17] H.S. GANDHI, G.W. GRAHAM, R. W. MCCABE, *J. Catal.* **216**, 433 (2003).
- [18] <http://www.autocatalyst-recycling.unicore.com/catalyticConverter>, 15.04.2016.
- [19] G. RUPPRECHTER, C. WEILACH, *J. Phys.: Condens. Matter* **20**, 184019 (2008).
- [20] R. SCHLÖGL, *Angew. Chem. Int. Ed.* **54**, 2 (2015).
- [21] <http://www.visioneng.com/resources/history-of-the-microscope>, 15.04.2016.
- [22] S. GÜNTHER, B. KAULICH, L. GREGORATTI, M. KISKINOVA, *Prog. Surf. Sci.* **70**, 187 (2002).
- [23] H. H. ROTERMUND, *Surf. Sci.* **603**, 1662 (2009).
- [24] R. IMBIHL, G. ERTL, *Chem. Rev.* **95**, 697 (1995).
- [25] C. SPIEL, D. VOGEL, Y. SUCHORSKI, W. DRACHSEL, R. SCHLÖGL, G. RUPPRECHTER, *Catal. Lett.* **141**, 625 (2011).
- [26] H. H. ROTERMUND, M. POLLMANN, I. G. KEVREKIDIS, *Chaos* **12**, 157 (2002).

- [27] E. BAUER, M. MUNDSCHAU, W. SWIECH, W. TELIEPS, *Ultramicroscopy* **31**, 49 (1989).
- [28] K. OURA, V. G. LIFSHITS, A. SARANIN, A. V. ZOTOV, M. KATAYAMA, *Surface Science. An Introduction*, Springer (2003).
- [29] M. EHSASI, M. BERDAU, T. REBITZKI, K.-P. CHARLÉ, K. CHRISTMANN, J. H. BLOCK, *J. Chem. Phys.* **98**, 9177 (1993).
- [30] M. BERDAU, G. G. YELENIN, A. KARPOWICZ, M. EHSASI, K. CHRISTMANN, J. H. BLOCK, *J. Chem. Phys.* **110**, 11551 (1999).
- [31] H. MURAKI, G. ZHANG, *Catal. Today* **63**, 337 (2000).
- [32] M. V. TWIGG, *Cat. Today* **117**, 407 (2006).
- [33] M. V. TWIGG, *Cat. Today* **163**, 33 (2011).
- [34] M. V. TWIGG, *Philos. Trans. A Math. Phys. Eng. Sci.* **363**, 1013 (2005).
- [35] <http://www.catalysts.basf.com>, 15.04.2016.
- [36] O. SALVAT, P. MAREZ, G. BELOT, *SAE Tech. Paper* **01**, 0473 (2000).
- [37] V. P. ZHDANOV, B. KASEMO, *Surf. Sci. Rep.* **29**, 31 (1997).
- [38] C. H. F. PEDEN, D. W. GOODMAN, D. S. BLAIR, P. J. BERLOWITZ, G. B. FISCHER, S. H. OH, *J. Phys. Chem.* **92**, 1563, (1988).
- [39] M. BOWKER, Q. GUO, Y. LI, R. W. JOYNER, *Catal. Lett.* **18**, 119 (1993).
- [40] M. J. P. HOPSTAKEN, J. W. NIEMANTSVERDRIET, *J. Chem. Phys.* **113**, 5457 (2000).
- [41] S. H. OH, G. B. FISHER, J. E. CARPENTER, D. W. GOODMAN, *J. Catal.* **100**, 360 (1986).
- [42] M. BOWKER, Q. GUO, R. W. JOYNER, *Surf. Sci.* **280**, 50 (1993).
- [43] L.-W. H. LEUNG, D. W. GOODMAN, *Catal. Lett.* **5**, 353 (1990).

- [44] V. P. ZHDANOV, B. KASEMO, *Appl. Surf. Sci.*, **74**, 147 (1994).
- [45] Y. SUCHORSKI, C. SPIEL, D. VOGEL, W. DRACHSEL, R. SCHLÖGL, G. RUPPRECHTER, *ChemPhysChem*, **11**, 3231 (2010).
- [46] D. VOGEL, C. SPIEL, Y. SUCHORSKI, A. URICH, R. SCHLÖGL, G. RUPPRECHTER, *Surf. Sci.* **605**, 1999 (2011).
- [47] Y. SUCHORSKI, G. RUPPRECHTER, *Surf. Sci.* **643**, 52 (2016).
- [48] D. VOGEL, Z. BUDINSKA, C. SPIEL, R. SCHLÖGL Y. SUCHORSKI G. RUPPRECHTER, *Catal. Lett.* **143**, 235 (2013).
- [49] N. KRUSE, A. FRENNET, J.M. BASTIN, *Catalysis and Automotive Pollution Control IV*, Elsevier, Amsterdam (1998).
- [50] J. P. CHANG, Y.-S. LIN, K. CHU, *J. Vac. Sci. Technol. B* **19**, 1782 (2001).
- [51] E. RYSHKEWITCH, D. W. RICHERSON, *Oxide Ceramics. Physical Chemistry and Technology*, Academic, Orlando (1985).
- [52] Q. PAN, X. WENG, M.S. CHEN, L.GIORDANO, G. PACCHIONI, C. NOGUERA, J. GONIAKOWSKI, S. SHAIKHUTDINOV, H.-J. FREUND, *ChemCatChem* **7**, 2620 (2015).
- [53] I. BESPALOV, M. DATLER, S. BUHR, W. DRACHSEL, G. RUPPRECHTER, Y. SUCHORSKI, *Ultramicroscopy* **159**, 147 (2015).
- [54] H.-J. FREUND, G. MEIJER, M. SCHEFFLER, R. SCHLÖGL, M. WOLF, *Angew. Chem. Int. Ed.* , **50**, 10064 (2011).
- [55] G. RUPPRECHTER, *Adv. Catal.* **51**, 133 (2007).
- [56] G. ERTL, *Reactions at Solid Surfaces*, John Wiley and Sons Inc. (2009).
- [57] F. GAO, Y. WANG, Y. CAI, D. W. GOODMAN, *J. Phys. Chem. C* **113**, 174 (2009).
- [58] F. GAO, Y. CAI, K. K. GATH, Y. WANG, M. S. CHEN, Q. L. GUO, D. W. GOODMAN, *J. Phys. Chem. C* **113**, 182 (2009).

- [59] H.-J. FREUND, *Chem. Eur. J.* **16**, 9384 (2010).
- [60] S. KUNZ, K. HARTL, M. NESSELBERGER, F. F. SCHWEINBERGER, G. H. KWON, M. HANZLIK, K. J. J. MAYRHOFER, U. HEIZ M. ARENZ, *Phys. Chem. Chem. Phys.* **12**, 10288 (2010).
- [61] B. ROLDAN CUENYA, F. BEHAFARID, *Surf. Sci. Rep.* **70**, 135 (2015).
- [62] R. IMBIHL, *Catal. Today* **105**, 206 (2005).
- [63] I. CHORKENDORF, J. NIEMANTSVERDRIET, *Concepts of Modern Catalysis and Kinetics*, Wiley-VCH (2003).
- [64] T. ENGEL, G. ERTL, *Adv. Catal.* **28**, 1 (1979).
- [65] T. ENGEL, G. ERTL, *J. Chem. Phys.* **69**, 1267 (1978).
- [66] N. CABRERA, N. MOTT, *Rep. Prog. Phys.* **12**, 163 (1949)
- [67] A. T. FROMHOLD, *Theory of Metal Oxidation*, North-Holland, Amsterdam (1976).
- [68] B. COX, *Advan. Corrosion Sci. Technol.* **5**, 173 (1976)
- [69] A. LYAPIN, L.P.H. JEURGENS, E.J. MITTEMEIJER *Acta Mater.* **53**, 2925 (2005).
- [70] E. G. MOORE, *Electronics Mag.*, **38**, 4, (1965).
- [71] E. STERN, J. F. KLEMIC, D. A. ROUTENBERG, P. N. WYREMBAK, D. B. TURNER-EVANS, A.D. HAMILTON, D. A. LAVAN, T. M. FAHMY, M. A. REED, *Nature* **445**, 519 (2007).
- [72] S. K. PARK, Y .K. HONG, Y. B. LEE, S. W. BAE, J. JOO, *Curr. Appl. Phys.* **9**, 847 (2009).
- [73] A. T. FROMHOLD, E. L. COOK, *Phys. Rev.* **163**, 650 (1967).
- [74] S. A. CAMPBELL, *The Science and Engineering of Microelectronic Fabrication*, Oxford University Press, (1996).

- [75] P. KOFSTAD, *High-Temperature Oxidation of Metals*, John Wiley and Sons, New York, London, Sydney (1966).
- [76] C. MORANT, J. M. SANZ, L. GALAN, L. SORIANO AND F. RUEDA, *Surf. Sci.* **218**, 331 (1989).
- [77] P. E. WEST, P. M. GEORGE, *J. Vac. Sci. Techn.* **A5**, 1124 (1987).
- [78] L. KUMAR, D. D. SARMA, S. KRUMMACHER, *Appl. Surf. Sci.* **32**, 309 (1988).
- [79] J.-M. ZHANGA, F. MAA, K.-W. XUB, *Appl. Surf. Sci.* **229**, 34 (2004).
- [80] Y.-N. WENA, J.-M. ZHANG *Solid State Commun.* **144**, 163. (2007).
- [81] C. DRI, C. AFRICH, F. ESCH, G. COMELLI, O. DUBAY, L. KÖHLER, F. MITTENDORFER, G. KRESSE, P. DUDIN, M. KISKINOVA, *J. Chem. Phys.* **125**,094701 (2006).
- [82] V. R. DHANAK, G. COMELLI, G. CAUTERO, G. PAOLUCCI, K. C. PRINCE, M. KISKINOVA, R. ROSEI *Chem. Phys. Lett.* **188 (3-4)**, 237 (1992).
- [83] C. VOSS, A. GAUSSMANN, N. KRUSE *Appl. Surf. Sci.* **67**, 42 (1993).
- [84] B. LANG, R. W. JOYNER, G. A. SOMORJAI, *Surf. Sci.* **30**, 440 (1972).
- [85] G. BLYHOLDER, *J. Phys. Chem.* **68**, 2772 (1964).
- [86] S. ROYER, D. DUPREZ, *ChemCatChem* **3**, 24 (2011).
- [87] I. TOYOSHIMA, G. A. SOMORJAI, *Catal. Rev. Sci. Eng.* **19**, 105 (1979).
- [88] M. C. J. BRADFORD, M. A. VANNICE, *Ind. Eng. Chem. Res.* **35**, 3171 (1996).
- [89] B. E. NIEUWENHUYS, *Surf. Sci.* **105**, 505 (1981).
- [90] B. E. NIEUWENHUYS, *Surf. Sci.* **126**, 307 (1983).
- [91] M. BOWKER, Q. GUO, R. JOYNER, *Surf. Sci.* **253**, 33 (1991).
- [92] R. J. BEHM, K. CHRISTMANN, G. ERTK, M. A. VAN HOVE, *J. Chem. Phys.* **73**, 2984 (1980).

- [93] Y. Y. YEO, L. VATTUONE, D. A. KING, *J. Chem. Phys.* **106**, 1990 (1997).
- [94] J. GOSCHNICK, M. GRUNZE, J. LOBODA-CACKOVIC, J. H. BLOCK, *Surf. Sci.* **189-190**, 137 (1987).
- [95] G. ERTL, P. RAU, *Surf. Sci.* **15**, 443 (1969).
- [96] J. GOSCHNICK, M. WOLF, M. GRUNZE, W. N. UNERTL, J. H. BLOCK, AND J. LOBODA-CACKOVIC, *Surf.Sci.* **178**, 831 (1986).
- [97] X. GUO, J. T. YATES, *J. Chem. Phys.* **90**, 6761 (1989).
- [98] H. CONRAD, G. ERTL, AND J. KÜPPERS, *Surf. Sci.* **76**, 323 (1978).
- [99] E. M. STUVE, R. J. MADIX, C. R. BRUNDLE, *Surf. Sci.* **146**, 155 (1984).
- [100] G. COMELLI, V. R. DHANAK, M. KISKINOVA, K. C. PRINCE, R. ROSEI, *Surf. Sci. Rep* **32**, 165 (1998).
- [101] K. A. PETERLINZ, S. J. SIBENER, *J. Phys. Chem.* **99**, 2817 (1995).
- [102] P. A. THIEL, J. T. YATES, W. H. WEINBERG, *Surf. Sci.* **82**, 22 (1979).
- [103] G. B. FISHER, S. J. SCHMIEG, *J. Vac. Sci. Technol.* **A 1**, 1064 (1983).
- [104] E. SCHWARZ, J. LENZ, H. WOHLGEMUTH, K. CHRISTMANN, *Vacuum* **41**, 167 (1990).
- [105] C. NYBERG, C. G. TENGSTAL, *Surf. Sci.* **126**, 163 (1983).
- [106] J.-W. HE, U. MEMMERT, P. R. NORTON, *J. Chem. Phys.* **90**, 5088 (1989).
- [107] J.-W. HE, U. MEMMERT, K. GRIFFITHS, P. R. NORTON, *J. Chem. Phys.* **90**, 5082 (1989).
- [108] A. GERBI, L. SAVIO, L. VATTUONE, F. PIRANI, D. CAPPELLETTI, M. ROCCA, *Angew. Chem. Int. Ed.* **45**, 6655 (2006).
- [109] R. IMBIHL, J. E. DEMUTH, *Surf. Sci.* **173**, 395 (1986).
- [110] P. SJÖVALL, P. UVDAL, *Chem. Phys. Lett.* **282**, 355 (1998).

- [111] H.H. ROTERMUND, S. NETTESHEIM, A. VON OERTZEN, G. ERTL, *Surf. Sci. Lett.* **275**, L645 (1992).
- [112] A. VON OERTZEN, H. H. ROTERMUND, S. NETTESHEIM, *Surf. Sci.* **311**, 322 (1994).
- [113] D. G. CASTNER, G. A. SOMORJAI, *Appl. Surf. Sci.* **6**, 29 (1980).
- [114] N. M. H. JANSSEN, M. F. H. VAN TOL, B. E. NIEUWENHUYS, *Appl. Surf. Sci.* **74**, 1 (1994).
- [115] M. F. H. VAN TOL, A. GIELBERT , B. E. NIEUWENHUYS, *Appl. of Surf. Sci.* **67**, 166 (1993).
- [116] J. GUSTAFSON, R. WESTERSTRÖM, A. RESTA, A. MIKKELSEN , J.N. ANDERSEN , O. BALMES, X. TORRELLES , M. SCHMID , P. VARGA, B. HAMMER, G. KRESSE, C.J. BADDELEY, E. LUNDGREN , *Catal. Today* **145**, 227 (2009).
- [117] J. GUSTAFSON, A. MIKKELSEN, M. BORG, E. LUNDGREN, L. KOHLER, G. KRESSE, M. SCHMID, P. VARGA, J. YUHARA, X. TORRELLES, C. QUIRÓS, J. N. ANDERSEN, *Phys. Rev .Lett.* **92**, 126102 (2004).
- [118] J. GUSTAFSON, A. MIKKELSEN, M. BORG, J. N. ANDERSEN, E. LUNDGREN, C. KLEIN, W. HOFER, M. SCHMID, P. VARGA, L. KÖHLER, G. KRESSE, N. KASPER, A. STIERLE, H. DOSCH, *Phys. Rev. B* **71**, 115442 (2005).
- [119] C. DRI, C. AFRICH, F. ESCH, G. COMELLI, O. DUBAY, L. KÖHLER, F. MITTENDORFER, G. KRESSE, P. DUDIN, M. KISKINOVA, *J. Chem.Phys.* **125**, 094701 (2006).
- [120] E. LUNDGREN, J. GUSTAFSON, A. MIKKELSEN, J. N. ANDERSEN, A. STIERLE, H. DOSCH, M. TODOROVA, J. ROGAL, K. REUTER, M. SCHEFFLER, *Phys. Rev. Lett.* **92**, 046101 (2004).
- [121] R. WESTERSTRÖM, C. J. WESTSTRATE, J. GUSTAFSON, A MIKKELSEN, J. SCHNADT, J. N. ANDERSEN, E. LUNDGREN, N. SERIANI, F. MITTENDORFER, G. KRESSE, A. STIERLE, *Phys. Rev. B* **80**, 125431 (2009).

- [122] I. LANGMIUR, *Trans. Faraday Soc.* **17**, 607 (1922).
- [123] I. LANGMIUR, *Trans. Faraday Soc.* **17**, 621 (1922).
- [124] G. ERTL, *Surf. Sci.* **299/300**, 742 (1994)
- [125] Y. SUCHORSKI, R. WROBEL, S. BECKER, H. WIESS, *J. Phys. Chem. C* **112**, 20012 (2008).
- [126] D. VOGEL, C. SPIEL, Y. SUCHORSKI, A. TRINCHERO, R. SCHLÄUGL, H. GRÄUNBECK, G. RUPPRECHTER, *Angew. Chem. Int. Ed.* **51**, 10041 (2012).
- [127] D. VOGEL, C. SPIEL, M. SCHMID, M. STÖGER-POLLACH, R. SCHLÖGL, Y. SUCHORSKI, G. RUPPRECHTER, *J. Phys. Chem. C.* **117**, 12054 (2013).
- [128] M. DATLER, I. BESPALOV, G. RUPPRECHTER, Y. SUCHORSKI, *Catal, Lett.* **145**, 1120 (2015),
- [129] J. S. FOORD, P. J. GODDARD, R. M. LAMBERT, *Surf. Sci.* **94**, 339 (1980).
- [130] C.-S ZHANG, B. J. FLINN, I. V MITCHELL, P. R. NORTON, *Surf. Sci.* **245**, 373 (1991).
- [131] F.-H. WANG, S.-Y. LIU, J.-X. SHANG, Y.-S. ZHOU, Z. LI, J. YANG *Surf. Sci.* **602**, 2212 (2008).
- [132] E. FROMM, O. MAYER, *Surf. Sci.* **74**, 259 (1978).
- [133] G. BAKRADZE, L. P. H. JEURGENS, E. J. MITTEMEIJER, *Surf. Sci.* **606**, 846 (2012).
- [134] S. K. R. S. SANKARANARAYANAN, S, RAMANATHAN, *J. Phys. Chem. C* **112**, 17877 (2008).
- [135] J. F. WATTS, J. WOLSTENHOLME, *An Introduction to Surface Analysis by XPS and AES*, John Wiley and Sons Ltd (2005).
- [136] D. P. WOODRUFF, T. A. DELCHAR *Modern Techniques Of Surface Science. Second edition*, Cambridge University Press (1994).

- [137] <http://www.thecatalyst.org/electabl.html>, 15.04.2016
- [138] Y. NISHINO, A. R. KRAUSS, Y. LIN, D. M. GRUEN, *J. Nucl. Mat.* **228**, 346 (1996).
- [139] A. LYAPIN, P. C. J. GRAAT, *Surf. Sci.* **552**, 160 (2004).
- [140] M. KURTH, P. C. J. GRAAT, *Surf. Interface Anal.* **34**, 220 (2002).
- [141] C. O. DE GONZALEZ, E. A. GARCIA, *Surf. Sci.* **193**, 305 (1988).
- [142] Y. SUCHORSKI, W. DRACHSEL, *Field Ion Microscopy (FIM) and Atom Probe (AP)* in: "Surface and Thin Film Analysis", G. Friedbacher, H. Bubert, Wiley-VCH (2011).
- [143] B. WADMAN, H.-O. ANDRÉN, in: C.M. Euchen, A.M. Garde (Eds.), *Zirconium in the Nuclear Industry, Ninth Symposium*, ASTM, STP 1132, ASTM, USA, (1991).
- [144] Y. DONG, A. T. MOTTA, E. A. MARQUIS *J. Nucl. Mat.* **442**, 270 (2013).
- [145] N. NI, S. LOZANO-PEREZ, J. SYKES, C. GROVENOR, *Ultramicroscopy* 111, 123 (2011).
- [146] T. TANABE, M. TOMITA, *Surf. Sci.* **222**, 84 (1989).
- [147] H. H. ROTERMUND, *J. Electron. Spectrosc. Relat. Phenom.* **98-99**, 41 (1999).
- [148] E. BRÜCHE, *Z. Phys.* **86**, 448 (1933).
- [149] M. C. ZEMAN, C. C. FULTON, G. LUCOVSKY, R. J. NEMANICH, W.-C. YANG, *J. Appl. Phys.* **99**, 023519 (2006).
- [150] H. HERTZ, *Ann. Phys.* **267**, 983 (1887).
- [151] W. HALLWACHS, *Ann. Phys.* **269**, 301 (1888).
- [152] A. EINSTEIN, *Ann. Phys.* **322**, 132 (1905).
- [153] H. SIMON, R. SUHRMANN, *Der lichtelektrische Effekt und seine Anwendungen*, Springer-Verlag, Berlin (1958).

- [154] http://www.nobelprize.org/nobel_prizes/physics/laureates/1981/,
15.04.2016
- [155] D. BRIGGS, M. P. SEAH, *Practical Surface Analysis*. Second edition Wiley (1990).
- [156] J. F. MOULDER, W. F. STICKLE, P. E. SOBOL, K. D. BOMBEN, *Handbook of X-ray Photoelectron Spectroscopy*, Physical Electronics Inc (1992).
- [157] T. MAITLAND, S. SITZMAN, *Electron Backscatter Diffraction (EBSD) Technique and Materials Characterization Examples* in: Zhou, Weilie, Wang, Zhong Lin Scanning Microscopy for Nanotechnology, Springer (2007).
- [158] S. NISHIKAWA, S. KIKUCHI, *Nature* **121**, 1019 (1928).
- [159] M. METHFESSEL, D. HENNIG, M. SCHEFFLER, *Phys. Rev. B* **46**, 4816 (1992).
- [160] K. JACOBI, *4.2 Electron work function of metals and semiconductors*, volume III/42A2, Springer Materials - The Landoldt-Börnstein Database (2002)
- [161] Y. ZHANG, J. ROGAL, K. REUTER, *Phys. Rev. B* **74**, 125414 (2006).
- [162] R. WESTERSTRÖM, J. GUSTAFSON, A. RESTA, A. MIKKELSEN, J. N. ANDERSEN, E. LUNDGREN, N. SERIANI, F. MITTENDORFER, M. SCHMID, J. KLIKOVITS, *Phys. Rev. B* **76**, 155410 (2007).
- [163] I. V. YUDANOV, R. SAHNOUN, K. M. NEYMAN, N. RÖSCH, J. HOFFMANN, S. SCHAUERMANN, V. JOHANEK, H. UNTERHALT, G. RUPPRECHTER, J. LIBUDA, H.-J. FREUND, *J. Phys. Chem. B* **107**, 255 (2003).
- [164] R. D. RAMSIER, K.-W. LEE, J. T. YATES, *Surf. Sci.* **322**, 243 (1995).
- [165] R. J. WROBEL, S. BECKER, H. WEISS *Phys. Chem. C* **119**, 5386 (2015))
- [166] J. WIDER, T. GREBER, E. WETLI, T.J. KREUTZ, P. SCHWALLER, J. OSTERWALDER, *Surf. Sci.* **417**, 301 (1998).
- [167] A. SCHAACK, R. IMBIHL, *J. Chem. Phys.* **113**, 9822 (2000).

- [168] E. L. SMART, E. A. MOORE, *Solid State Chemistry: An Introduction*. Fourth Edition CRC Press (2012).
- [169] Q. GUO, R.W. JOYNER, *Appl. Surf. Sci.* **144-145**, 375 (1999).
- [170] D. YAMASHITA, A. ISHIZAKI *Appl. Surf. Sci.* **363**, 240 (2016).
- [171] K. WANDELT, J. E. HULSE, *J. Chem. Phys.* **80**, 1340 (1984).

Publications list

I. Bepalov, M. Datler, S. Buhr, W. Drachsel, G. Rupprechter, Y. Suchorski:

*"Initial stages of oxide formation on the Zr surface at low oxygen pressure:
an in situ FIM and XPS study",*

Ultramicroscopy 159 (2015), 147;

M. Datler, I. Bepalov, G. Rupprechter, Y. Suchorski:

*"Analyzing the reaction kinetics for individual catalytically active components:
CO oxidation on a Pd powder supported by Pt foil",*

Catal. Lett., 145 (2015), 1120;

M. Datler, I. Bepalov, S. Buhr, J. Zeininger, M. Stöger-Pollach, J. Bernardi, G.
Rupprechter, Y. Suchorski:

"H₂ oxidation on stepped Rh surfaces: μ m-scale versus nanoscale"

submitted to Catal. Lett.;

Y. Suchorski, I. Bepalov, M. Datler, D. Vogel, S. Budinska, S. Kozlov, K. Neyman, G.
Rupprechter :

*"Metal-support boundary effect reloaded: CO oxidation on the supported Pd model cat-
alysts"*

in preparation;

Conference contributions

Oral presentations

I. Bepalov, M. Datler, J. Zeininger, M. Stöger-Pollach, J. Bernardi, G. Rupprechter, Y. Suchorski:

"Catalytic CO oxidation on high index Rh surfaces";

SFB-F45 "FOXSI" Annual PhD Workshop 2016, Haus im Ennstal; 30.03.2016 - 02.04.2016.

S. Buhr, J. Zeininger, I. Bepalov, M. Datler, G. Rupprechter, Y. Suchorski: *"Catalytic CO oxidation on Rh on the nanoscale";* SFB-F45 "FOXSI" Annual PhD Workshop 2016, Haus im Ennstal; 30.03.2016 - 02.04.2016.

Y. Suchorski, M. Datler, I. Bepalov, J. Zeininger, G. Rupprechter:

"Local surface reaction kinetics "just by imaging";

ECOSS-31 31st European Conference on Surface Science, Barcelona; 31.08.2015 - 04.09.2015; in: "Book of Abstracts", (2015); p. 64;

J. Zeininger, I. Bepalov, M. Datler:

"Initial oxidation of zirconium: XPS And PEEM studies";

Vienna Young Scientists Symposium, Wien; 25.06.2015 - 26.06.2015; in:

"VSS VIENNA young SCIENTISTS SYMPOSIUM",

Book-of-Abstracts.com, Gumpoldskirchen, (2015), ISBN: 978-3-9504017-0-7; p. 156 ;

M. Datler, I. Bespalov, J. Zeininger, G. Rupprechter, Y. Suchorski: "*Visualizing Reaction Kinetics: Hydrogen Oxidation on Rh and Rh/ZrO₂ model catalysts*"; International SFB FOXSI Symposium 2015, TUtheSky Lounge, TU Vienna; 11.05.2015 - 13.05.2015.

M. Datler, I. Bespalov, J. Zeininger, G. Rupprechter, Y. Suchorski: "*Visualizing Local Reaction Kinetics: Hydrogen Oxidation on Rhodium*"; 7th International Workshop on Surface Physics, Trzebnica, Poland; 21.06.2015 - 25.06.2015; in: "7th International Workshop on Surface Physics, Program and Abstracts", (2015); p. 41;

I. Bespalov:

"*Catalytic CO oxidation on supported model catalysts: a PEEM and XPS study*"
Seminar of the Institute of Materials Chemistry,
Vienna University of Technology, Vienna, Austria; 2015;

I. Bespalov:

"*CO oxidation on the ZrO₂ supported Pd model catalysts: the role of the support*";
SFB-F45 "FOXSI" Annual PhD Seminar 2014, Hochkar, Göstling; 2014;

D. Vogel, I. Bespalov, G. Rupprechter, Y. Suchorski:

"*Cartography of the reaction fronts in the CO oxidation on individual grains of polycrystalline Pd foil*"; 6th International Workshop on Surface Physics, Niemcza, Poland; 01.09.2013 - 06.09.2013; in: "Functional Materials", (2013); p. 44;

I. Bespalov:

"*CO oxidation on supported Pd model systems: PEEM studies*";
2nd Workshop of the TU Vienna Graduate school "CatMat",
Vienna University of Technology; 2013;

Posters

M. Datler, I. Bepalov, S. Buhr, J. Zeininger, M. Stöger-Pollach, J. Bernardi, G. Rupprechter, Y. Suchorski: "*Spatio-temporal oscillations in hydrogen oxidation on Rh: mesoscopic versus nanoscale*"; SFB-F45 "FOXSI" Annual PhD Workshop 2016, Haus im Ennstal; 30.03.2016 - 02.04.2016.

I. Bepalov, M. Datler, G. Rupprechter, J. Zeininger, Y. Suchorski:
"*CO oxidation on Rh: role of defects in the local reaction kinetics*";
SFB-F45 "FOXSI" Annual Meeting 2015, Stadtschlaining; 14.09.2015 - 16.09.2015;

M. Datler, I. Bepalov, S. Buhr, J. Zeininger, G. Rupprechter, Y. Suchorski:
"*Hydrogen oxidation on Rh: nm- versus μm -scale*";
SFB-F45 "FOXSI" Annual Meeting 2015, Stadtschlaining; 14.09.2015 - 16.09.2015;

I. Bepalov, M. Datler, S. Buhr, J. Zeininger, P. Blaha, G. Rupprechter, Y. Suchorski:
"*Initial surface oxidation of Zr: XPS, PEEM, FIM, FEM and DFT studies*";
ECOSS-31, 31st European Conference on Surface Science, Barcelona; 31.08.2015 -
04.09.2015; in: "Book of Abstracts", (2015); p. 412;

M. Datler, I. Bepalov, G. Rupprechter, Y. Suchorski:
"*Spatially- and component-resolved reaction kinetics on a μm -scale:
CO oxidation on Pd model catalysts*"; ECOSS-31, 31st European Conference on Sur-
face Science, Barcelona; 31.08.2015 - 04.09.2015;
in: "Book of Abstracts", (2015); p. 577;

M. Datler, I. Bepalov, J. Zeininger, G. Rupprechter, Y. Suchorski:
"*Mapping the Reaction Front Nucleation and Propagation in H_2 Oxidation on Rh*"; 7th
International Workshop on Surface Physics, Trzebnica, Poland; 21.06.2015 - 25.06.2015;
in: "7th International Workshop on Surface Physics, Program and Abstracts", (2015);
p. 52;

I. Bepalov, M. Datler, S. Buhr, J. Zeininger, P. Blaha, G. Rupprechter, Y. Suchorski: "*Bridging Scales in the Surface Oxidation of Zr: XPS, PEEM, FIM, FEM and DFT Studies*"; 7th International Workshop on Surface Physics, Trzebnica, Poland; 21.06.2015 - 25.06.2015; in: "7th International Workshop on Surface Physics, Program and Abstracts", (2015); p. 49;

I. Bepalov, M. Datler, S. Buhr, J. Zeininger, P. Blaha, G. Rupprechter, Y. Suchorski: "*Initial stages of Zr surface oxidation: XPS, PEEM, FIM, FEM and DFT studies*"; International SFB FOXSI Symposium 2015, TUtheSky Lounge, TU Vienna; 11.05.2015 - 13.05.2015;

M. Datler, I. Bepalov, J. Zeininger, G. Rupprechter, Y. Suchorski: "*Topography of the reaction front nucleation and propagation in H₂ oxidation on Rh*"; International SFB FOXSI Symposium 2015, TUtheSky Lounge, TU Vienna; 11.05.2015 - 13.05.2015;

M. Datler, I. Bepalov, G. Rupprechter, Y. Suchorski: "*Reaction front nucleation and propagation in H₂ oxidation on Rh*"; 4th Annual FOXSI PhD Workshop, Haus im Ennstal; 29.03.2015 - 01.04.2015;

I. Bepalov, M. Datler, S. Buhr, J. Zeininger, P. Blaha, G. Rupprechter, Y. Suchorski: "*Surface Oxidation of Zr: PEEM, FIM, XPS and DFT Study*"; 4th Annual FOXSI PhD Workshop, Haus im Ennstal; 29.03.2015 - 01.04.2015;

I. Bepalov, M. Datler, G. Rupprechter, Y. Suchorski: "*Compatibility of the nm-scale and μ m-scale studies of the catalytic CO oxidation on Pd: FIM/FEM versus PEEM*"; International Conference on Atom Probe Tomography and Microscopy, Stuttgart; 31.08.2014 - 05.09.2014; in: "APT and M", (2014); p. 216;

S. Buhr, I. Bepalov, M. Datler, G. Rupprechter, Y. Suchorski:

"Initial oxide formation on the Zr surface at low oxygen pressure: an in situ FIM, PEEM and XPS study"; International Conference on Atom Probe Tomography and Microscopy, Stuttgart; 31.08.2014 - 05.09.2014; in: "APT and M", (2014); p. 215;

Y. Suchorski, M. Datler, I. Bepalov, R. Schlögl, G. Rupprechter:

"Laterally-resolved reaction kinetics in CO oxidation on Pd: powder versus plane Pd(hkl) surfaces"; 3S'14 Symposium on Surface Science 2014, St. Christoph/Arlberg, St. Christoph/Arlberg; 09.03.2014 - 15.03.2014; in: "3S'14 Symposium on Surface Science 2014, St. Christoph/Arlberg", (2014); p. 129 - 130;

M. Datler, I. Bepalov, R. Schlögl, G. Rupprechter, Y. Suchorski:

"The role of the surface morphology in the CO oxidation reaction: Pd powder versus plane Pd(hkl) surfaces"; SFB-F45 "FOXSI" Annual PhD Seminar 2014, Hochkar, Göstling; 07.04.2014 - 10.04.2014;

I. Bepalov, M. Datler, D. Vogel, Z. Budinska, R. Schlögl, G. Rupprechter, Y. Suchorski: *"Surface oxides on Zr and Pd surfaces: an XPS and PEEM studies"*; 2nd Annual SFB FOXSI Symposium, Conference Center Burg Schlaining; 18.09.2013 - 20.09.2013;

D. Vogel, I. Bepalov, G. Rupprechter, Y. Suchorski:

"Catalytic CO oxidation on individual grains of polycrystalline Pd:"; 2nd Annual SFB FOXSI Symposium, Schlaining; 18.09.2013 - 20.09.2013;

D. Vogel, Z. Budinska, I. Bepalov, M. Datler, R. Schlögl, G. Rupprechter, Y. Suchorski:

"Kinetics of oxides formation on Zr and Pd surfaces: an XPS and PEEM study"; 6th International Workshop on Surface Physics, Niemcza, Poland; 01.09.2013 - 06.09.2013; in: "Functional Materials", (2013), p. 44;

I. Bespalov, M. Datler, D. Vogel, Z. Budinska, G. Rupprechter, Y. Suchorski:
"Reaction front propagation in the CO oxidation on Pd-powder catalysts";
SFB FOXSI PhD Workshop 2013 "FOXSKI", Hochkar; 18.03.2013 - 21.03.2013.

Curriculum vitae

Personal details

Full name: Ivan Bespalov

Data and place of birth: 17.06.1987, Krasnoyarsk-45, USSR

Citizenship: Russian

Address: Dr. Bruno Buchwieser gasse 1/1113, 2340 Mödling, Austria

e-mail: ivan.bespalov@tuwien.ac.at

Education

Sep.2012-May.2016 Ph.D. studies at the Institute of Materials Chemistry,
Vienna University of Technology, Austria;

Supervisors: Prof. Y. Suchorski and Prof. G. Rupprechter

Sep.2008-Jun.2010 M.Sc., Tomsk State University, Tomsk, Russian Federation

Thesis title: *Research of influence of the nature of metal fuel
and catalytic additives on burning of high-energy materials*

Sep.2004-Jun.2008 B.Sc., Tomsk State University, Tomsk, Russian Federation

Thesis title: *Influence of structure of metal fuel on burning of
nitrate fuel systems*